Synthesis of Aluminosilicate Nanomaterials using Surfactant Self-assembly as a Template and Their Catalytic Applications

José Andrés Hernández Gaitán

September 2024

Synthesis of Aluminosilicate Nanomaterials using Surfactant Self-assembly as a Template and Their Catalytic Applications

A dissertation submitted to
THE GRADUATE SCHOOL OF ENGINEERING SCIENCE
OSAKA UNIVERSITY
in partial fulfillment of the requirements for the degree of
DOCTOR OF PHILOSOPHY IN ENGINEERING

BY

José Andrés Hernández Gaitán

September 2024

Abstract

Synthesis of Aluminosilicate Nanomaterials using Surfactant Self-assembly as a Template and Their Catalytic Applications

José Andrés Hernández Gaitán

Graduate School of Engineering Science, Osaka University

We are currently in the 6th technological wave, commonly called the nanotechnology wave. Nanotechnology is a relatively new field (establish in 1959 by Richard Feynman) with the possibility of creating fine-tuned and enhanced materials.

Over the last 30 years, the research and use of nanotechnology has increased considerably, being the United States of America the biggest consumer of this technology followed by southern east and eastern Asia. In Japan alone both the research and spent budget on this technology has been steadily increasing over the last 15 years and the field of applications has been steadily increasing, venturing into many fields such as environment/energy, electronics, infrastructure, healthcare and life science.

The main aspects for the need to change from bulk to nano materials is because nano materials have increased surface area, selectivity and performance and can be tailored to specific applications and most of them are heterogeneous materials. On the contrary nowadays common materials main detractors are; many of the current applications still use rare metals, which are scarce and expensive. From an environmental point of view, most of these materials generate homogeneous mixtures, difficult to separate.

When synthesizing nanomaterials, there are two main synthetic approaches, top-down and bottom-up. The top-down approach means reduce the size of the structure toward the nanoscale. While the bottom-up approach is the formation of large nanostructure from smaller atoms and molecules. Due to the nature of the top-down approach of using an external force to break the material into smaller pieces, the overall quality of the material is compromised and its properties are compromised. On the other hand, bottom-up approach yields better quality materials with controlled properties, but their operational costs are high. Hence, more research on this topic is required and soft-templating methods for the synthesis of novel nanomaterials with catalytic applications are the main topics of this thesis.

Chapter 1 is the general introduction section. Here, I have introduced the background and the overview of this study in this chapter as well as the main objectives which are described at the end. The basic concepts of lyotropic mixtures are described in this Chapter, which are required to understand the synthetic method and its potential. Finally, we describe the main characteristic of aluminosilicate materials and their potential and versatility as catalytic materials.

In Chapter 2, I established a bottom-up nanosheet synthesis method, named the "two-dimensional reactor in amphiphilic phases (TRAP) method." In this method, sparsely suspended amphiphilic bilayers work as the reactors in hyperswollen lamellar (HL) phases. This method has the potential to synthesize a wide range of nanosheets of various materials: polymers, metal-organic frameworks, MO, and metals for different applications. I focused on the controlled synthesis of amorphous aluminosilicate nanosheets (a-ASns) and further used them as universal precursors for various zeolite-NSs. Secondly, I discuss the Emulsion Method, which allow us to synthesize crystalline aluminosilicate nanomaterials using a lyotropic mixture of Water/Surfactant/Organic solvent, with decreased diffusion resistance, increasing their performance in catalytic applications. Finally, I described the characteristics of these aluminosilicate nanomaterials and the characterization methods.

Abstract

In Chapters 3, I evaluated the catalytic application of amorphous aluminosilicate nanosheet (a-ASns) as support for nickel metal catalyst in the Catalytic Decomposition of Methane (CDM). In this chapter I compared a-ASns with bulky and mesoporous amorphous aluminosilicates as supports. I further evaluate the promotion of known metal promoters such as Chromium and Lanthanum using different incorporation methods such as wet impregnation and alkaline precipitation of metal nitrates in combination with hydrolysis of Si and Al species. Lastly, I even evaluated the morphology of the active species, by synthesizing nickel nanoparticles and further studying their effect as active species and as supports itself.

Lastly, in Chapters 4, I focus on one of the primary challenges of the 21st century; to insert conventional waste products into circular processes. Plant-based waste has been gaining interest in the research community, as new biorefineries breakthroughs take place. One of the main components of plants is lignin, and it has great potential, due to is composition of phenolic compounds, to be used in the production of high value chemicals, such as phenol. (Worldwide production of lignin is around 150 billion tons, out of which 415 million tons come from five major crops). Hence, I study one of the intermediary reactions for the chemical breakdown of lignin "transalkylation", by using a similar phenolic compound found in lignin, 4-propylphenol (ppp), and reacted it with supercritical benzene over nanometer sized MFI-type zeolites using a fix bed reactor.

In summary, I have successfully adapted lyotropic mixtures to different nanomaterials and morphologies by modifying the composition of the mixture, and further control the nanomaterial particle size by controlling the reagents amount during the nanomaterial synthesis. These materials showed great promise in different catalytic applications due to their great surface area, tailored active sites and shape selectivity.

Table of contents

Contents

Table of Contents

Chapter 1

General Introduction

We are currently in the 6th technological wave, "nanotechnology" and whether it will have the potential to be a general-purpose technology (GPT) is still under debate. However, is of general agreement that nanotechnology has revolutionized industries around the world, improving almost every industrial domain such as agriculture, food, medicine, clothing, materials, automobiles, civil engineering, environmental management, both energy storage and generation, life science among others. [1,2]

This emerging technology offers great potential for manufacturing substantially improved performance products. Just in the United States alone, more than 42 billion dollars have been generated in revenue by American companies in 2017[3] with very current applications such as the COVID-19 vaccines where lipid nanoparticles were used in more than 676 million doses [4].

In order to achieve further improvements, a great effort is being made in the research and development of nanomaterials, which are the core of nanotechnology.

1.1 Nanomaterials

As we decrease the size of the materials, we can reach the size of nanomaterials as seen in **Figure 1.1**. These materials, with at least one dimension in the range of 1 to 100 nm are considered nanomaterials. They exhibit superior catalytic properties compared to their bulk counterparts such as improved surface area, tailored morphology and increased active sites, which influence selectivity, performance and efficiency, as well as, improved magnetic, electric, optical and mechanical properties. [5] Currently, these materials have become a predominant research field for industrial and engineering applications such as energy generation and storage, [6–15] catalysis, [16–21] separation processes,[22–25] food industry,[26–30] and medical devices (diagnostic biosensors, drug delivery systems and imaging probes),[31–36] among other more specialized applications. Simply put, we are currently in the 6th technological wave of nanotechnology, and nanomaterials play a key role in the development of future technology.

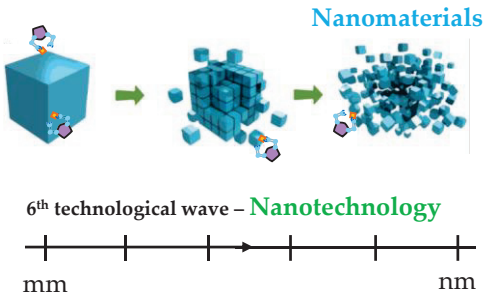

Figure 1.1 Nanomaterials

1.1.1 Synthesis Approaches

There are two main approaches to the synthesis of nanomaterials "Top-down" and "Bottom-up", as seen as **Figure 1.2**.

Top-down approach starts from bulky materials and breaks them down to a nanosized scale. Usually, an external force or source of energy is required to breakdown the particles such as mechanical milling, laser ablation, etching, sputtering and electro-deposition. This approach usually has high yields and low costs, but the quality of the material is low and difficult to control.

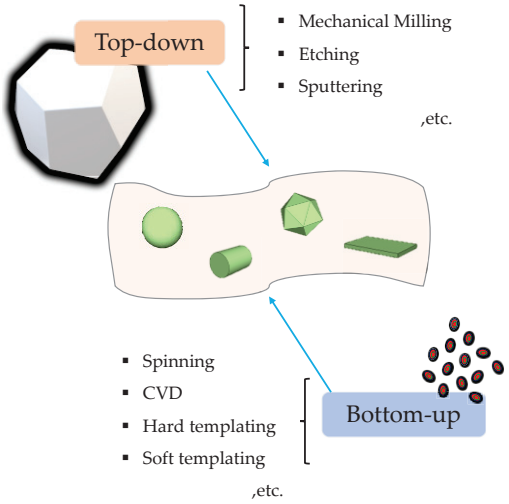

Figure 1.2 Nanomaterials synthetic approaches

Conversely, bottom-up approaches start from atomic or molecular level and build up to nanostructures. This approach allows precise control of the properties and the quality of the nanomaterials, but more research is required to improve the efficiency of the process and decrease operational cost for scale-up. In this study I focus mainly on bottom-up approaches, specifically soft-template method

1.1.2 Soft Templating

This approach allows the synthesis of nanostructured materials molded by the intermolecular interaction of flexible organic molecules, high polymers and surfactants (anionic, cationic and non-ionic) creating with a wide range of morphologies depending on their concentration and the mixture composition, at mild conditions and straightforward implementation. I focus mainly on the surfactant-assisted soft-templating. [37–40]

Typically, soft template methods encompass macro and microemulsions, micelles or vesicles, and molecular super-structure self-arrangements, which give opens the door to new methods such as polymer networks, hydrogels, emulsion droplets, bicontinuous emulsions, etc.

The research of this thesis focuses on emulsion and supramolecular assemblies soft-templating methods.

1.1.2.1 Surfactants

Surfactants are amphiphilic molecules which means that are composed of a hydrophilic "head" group and a hydrophobic "tail" region, with the capability to modify the properties of surfaces and interfaces between different media, as solid-liquid or liquid-gas interfaces, hence their common name surfactants (from surface active agent). These molecules have the capability to self-assemble into super-structures of several shape anisotropies and sizes, acting as flexible templates where a wide range of material morphologies can be synthesized.

Depending on their capability to interact with other molecules, and based on the surfactant charge, they can be classified in anionic, nonionic, cationic or amphoteric surfactants. This allows for different interactions in the templating method with the precursor's molecules affecting the overall synthetic process. [40]

1.1.2.2 Lyotropic Mixture

Mixtures of amphiphilic molecules and solvents can create lyotropic mesophases, with unique characteristics. As previously stated, the amphiphilic molecules can arrange themselves into different super-structures, creating different templating systems of different sizes and shapes.

A first classification approach based on the dimensions of these templates propose three big super-structure families, as seen in **Figure 1.3**:

a. Micellar systems

   These aggregates have small shape anisotropy with typical dimensions of about 10nm and shape anisotropy order of 1:2 in linear dimensions.

b. Aggregates of large shape anisotropy

   These aggregates are sometimes referred to as infinite, with typical orders of 1:100 in terms of linear dimensions.

c. Bi-continuous systems

   In these structures, amphiphilic molecules self-assemble as three-dimensional continuous structures at scales larger than 1000 nm.

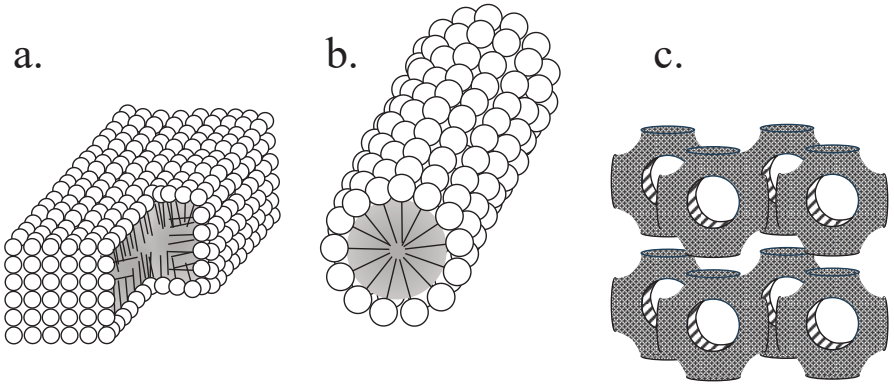

Figure 1.3 Amphiphile molecule super-structures in lyotropic phases. a) orthorhombic micelle, b) cylindrical aggregate, c) bicontinuous molecular aggregate with a cubic symmetry

1.1.2.3 Self-assembled Systems

When discussing lyotropic mixtures, an important concept to understand is the *critical micellar concentration*, CMC, [41–43] defined as the concentration at which amphiphilic molecules self-assemble into micelles. This term is the main the main chemical-physical parameter of surfactants that determines their surface activity and self-assemble aggregation. CMC value has become a key design target because it is correlated with many physicochemical properties such as detergency, equivalent conductivity, high frequency, conductivity, surface tension, osmotic pressure and interfacial tension.

Let c be the concentration of amphiphilic molecules in the solution of amphiphiles and a solvent. For c < CMC, the amphiphile molecules remain isolated. For c > CMC, the fraction of isolated amphiphile molecules remains almost constant and the concentration of micelles increases with c.

At a good temperature, CMC can be estimated based on the length of the surfactant, [44] given by the following equation:

$$\log_{10} \mathrm{CMC} = 1.6 - 0.3\, n_c \qquad \text{Eq.1}$$

where n_c is the number of carbon atoms in the chain.

Besides CMC, the critical micellar temperature, C MT, is another concept that plays a similar role in the self-assembly of amphiphilic molecules. Which is the lower temperature limit between the hydrated solid phase and the micellar phase and depends on the amphiphilic molecule being used and on the ionic strength of the mixture. [45]

Due to the dual hydrophobicity properties of amphiphile molecules, aggregates of these molecules can be of two-natures: direct and inverted, which refers to the relative concentration of polar and non-polar solvents with respect to the concentration of the principal amphiphile. In direct structures, the polar solvents have the largest concentration and in inverted, non-polar solvents, as seen in **Figure 1.4**.

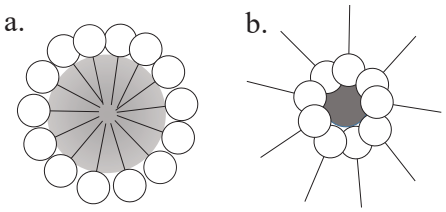

Figure 1.4 Examples of direct and inverted structures. a) direct micelle, b) inverted micelle

If the concentration of *c* increases to values much larger than CMC, we will reach anisotropic liquid crystalline phases. These crystalline phases display long-range orientational order and, in some cases, long or medium-range positional order in one or two dimensions.

Lyotropic liquid crystals are intermediate states of matter or mesophases, halfway between an isotropic liquid and a solid crystal. They display orientational order and even positional order along some directions. These materials flow like an isotropic fluid and have characteristic optical properties of solid crystals.

In summary, the polymorphism of a lyotropic mixture depends on the different parameters of the amphiphile itself; such as the ionic character of the polar head, the size and volume occupied by the head with respect to the parameters of the chain, the presence or absence of another surfactant (usually called co-surfactant) or of a salt in the mixture, pH, and ionic strength of the solution, the purity of the compounds, and the temperature, among other factors.

1.1.2.4 Phase Diagrams of Lyotropic Mixtures

Phase diagrams of lyotropic mixtures are useful tools to locate a wide range of stable structures and regions depending on which surfactant is used and its physical properties such as temperature, pressure and the relative concentration of the components. For constant temperature and pressure, triangular phase diagrams are a useful tool to locate these regions for each specific case, as seen in **Figure 1.5**.

An interesting feature of lyotropics is the possibility of mixing a large number of components and the positioning of the different regions will vary depending on the components of the mixture, their concentration and the operational conditions of the system (temperature and pressure).

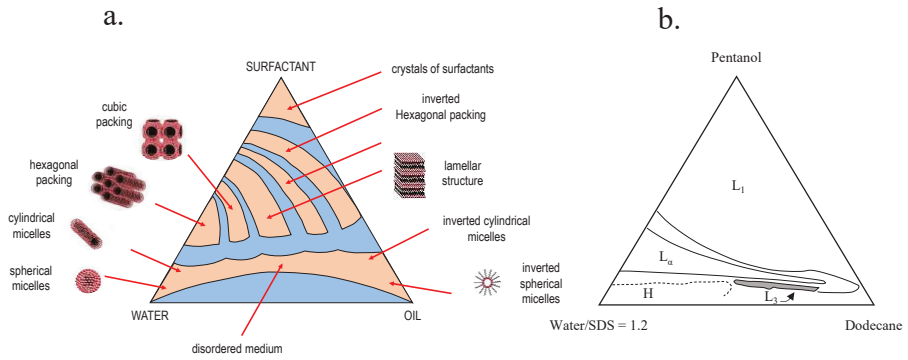

Figure 1.5 a) Different lyotropic mixture regions of stable amphiphile structures, b) Partial isotherm sketch of a quaternary mixture of SDS, dodecane, pentanol and water. (L_1 = direct micelle, L_2 = indirect micelle, L_3 = sponge, H = Hexagonal)

For this research I normally used complex mixtures, however here I classify them as ternary or quaternary lyotropic mixtures with the material precursors in the desired polar or non-polar phase. Ternary mixtures include water/non-polar/surfactant system, however, in quaternary mixtures; a co-surfactant is added to the system. Normally the surfactant or the co-surfactant is represented as a constant value correlated to one of the three previous components, as seen in Figure 5. In general, similar features are observed in most of the partial isotherms of ternary mixtures composed by a surfactant, an alcohol and water.

1.1.2.5 Structures and Terminology

Lyotropic liquid crystals provide perhaps the richest examples of polymorphism among complex dfluid mixtures.

1.1.2.5.1 Micellar Isotropic Phase

Direct and inverted micelle structures can be found in different regions of the lyotropic phase diagram, with the ability to change their shape anisotropy depending on temperature and relative concentration of the compounds of the mixture. At low amphiphilic molecular concentrations ($c \geq CMC$), micelles are mostly spherical in shape. At larger concentrations of amphiphiles ($c \approx 10^2 \times CMC$), micelles may have non-spherical shapes. In some lyotropic mixtures, isolated micelles can have orthorhombic symmetry[46].

Micellar arrangements can lead to lyotropic nematic phases. Two of them with axial character N_C (calamitic nematic) and N_D (discotic nematic), [47–49] as seen in **Figure 1.6**, and a third phase of biaxial character N_B. These mesophases are composed of micelles with short-range positional and long-range orientational order.

Cholesteric phase can be formed if a nematic phase is doped with a chiral molecule or if a mixture contains a chiral amphiphilic molecule. [50]

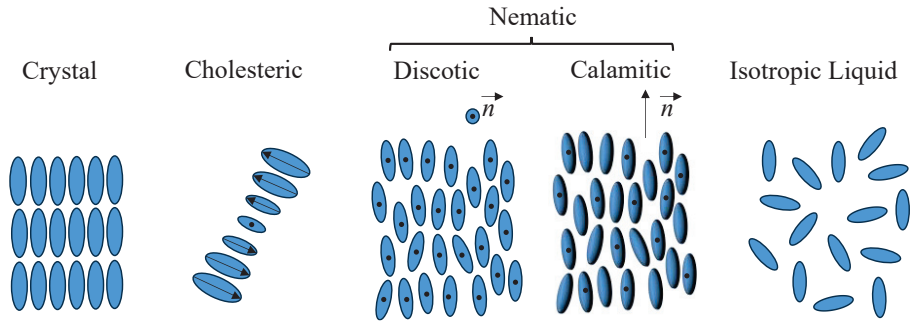

Figure 1.6 Sketch of different micellar orders in lyotropic mixtures in the context of the intrinsically biaxial cylinder-like micelle model. *a) The dots represent a particular surface of the micelle , b) cylinder-like micelles in cholesteric phase rotates around an axis perpendicular to the infinite-fold symmetry axes of the micelles (represented by the black arrows inside)

1.1.2.5.2 Lamellar Phase

In this phase, the amphiphile molecules arrange as supermolecular aggregates, forming layers with a large shape anisotropy. The thickness of these layers is mainly dependent on the length of the amphiphile molecule (usually of the order of two) and temperature. The layers of amphiphiles can show some orientational order or show an undulated topology (ripple), as seen in **Figure 1.7**.

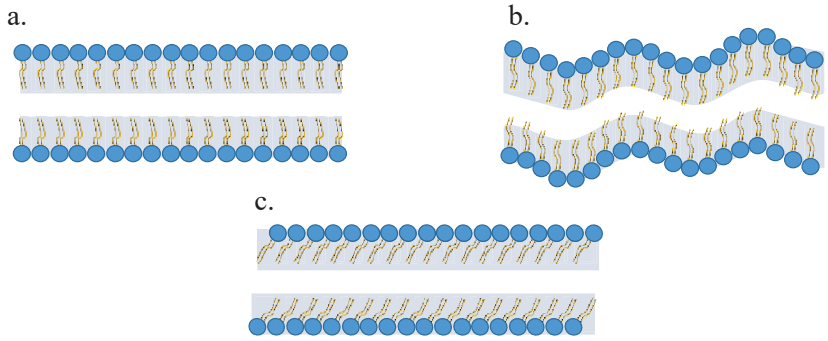

Figure 1.7 Sketch of a) lamellar structure, b) ripple phase, c) hexatic type ordering

1.1.2.5.3 Hexagonal Phase

In this phase, amphiphile molecules self-arrange as long cylinder-like aggregates, with large shape anisotropy, as seen in **Figure 1.8**. The diameter of the cylinders is of the order of twice the length of the main amphiphilic molecule and the lengths usually are on the range of 50 times larger than the diameter. These cylinders can further order into hexagonal, rectangular and square packaging as seen in Figure 8. Another example of polymorphism in these molecular aggregates systems are long unfolded ribbons.

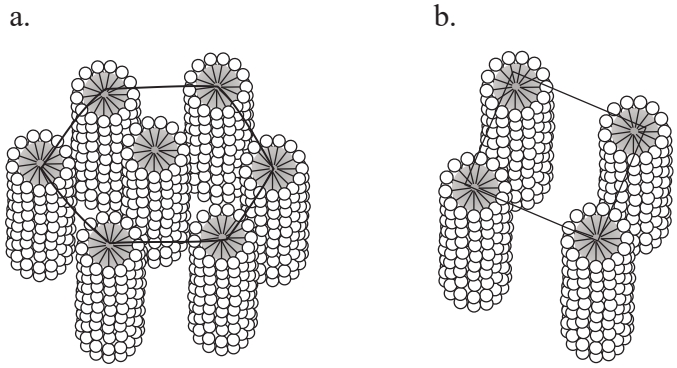

Figure 1.8 Sketch of hexagonal phase, long cylinder-like aggregates with large shape anisotropy, a) hexagonal packing, b) square packing.

1.1.2.5.4 Bicontinuous Phase

For these phases, amphiphilic molecules self-assemble in a three-dimensional structure, as seen in **Figure 1.9**. This means that molecules, with their head in the aggregated surface, can diffuse continuously through all the structure without the need of going to the bulk in which the solvent is present. This characteristic is not found in phases with aggregates as micelles, cylinders or lamellae, where the molecule indeed requires going through the solvent to diffuse from one aggregate to another.

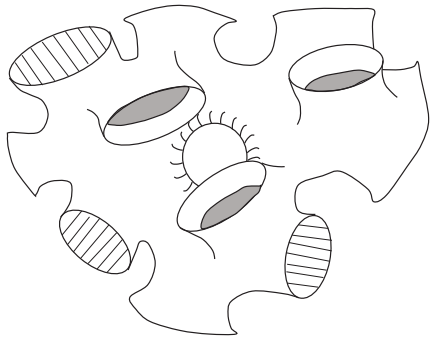

Figure. 1.9 Sketch of the sponge phase

1.1.2.6 Emulsion Method

This method takes advantage of the templating capabilities of surfactant molecules. The desired precursors are dissolved in water, hydrolyzed with an organic directing agent (OSDA) at room temperature. Further mixed with a Surfactant/Organic Solvent solution, creating an emulsion, which encapsulates the reactants inside the formed micelles. The micelles formed in the Water/Surfactant/Organic solvent system quench the hydrothermal treatment on nucleation and the increased nucleation rate controlled by the concentration of reactants facilitates a narrow size distribution of zeolite nanospheres. [51–53] Two important parameters of this method are the concentration of the surfactant in the organic solvent and the molar ratio of water to surfactant due to their strong correlation with the morphology and crystal size of the synthesized zeolite. [54]

Compared to other soft-template methods, the emulsion method can withstand high temperatures without compromising the templates (micelles) integrity.

1.1.2.7 TRAP Method

Figure 1.10 shows the TRAP method process which uses the hyperswollen lamellar (HL) phases of lyotropic liquid crystals, in which sparsely suspended amphiphilic molecules superstructures, consisting of many bilayers with several nm thicknesses, work as independent "two-dimensional reactors in amphiphilic phases" TRAPs,[55] for the synthesis of a wide range of nanosheet materials. They are useful for the nanosheet synthesis of various materials: polymers, [56] metal-organic frameworks [57] and metals.[58] This bottom-up TRAP method has allowed us to obtain thin nanosheets materials with high S_{ext}. The nanosheets with widths of several hundred nm are composed of aggregated nanoplates with widths of several tens of nm. The patchy nanosheets can work as precursors of further complex nanomaterials. [59]

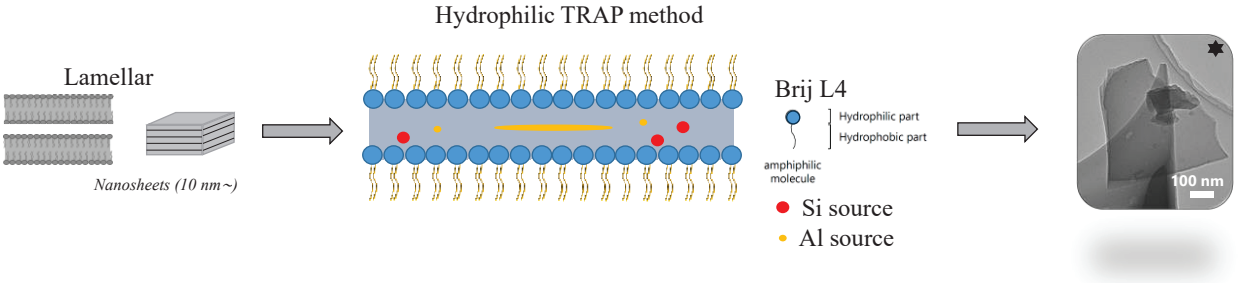

Figure 1.10 TRAP method for the synthesis of amorphous aluminosilicates nanosheets
(*MFI-type sample synthesized by two-step synthesis 1) a-ASns using TRAP + emulsion method hydrothermal synthesi)

1.2 Aluminosilicates

Aluminosilicates (AS) are materials that share a basic chemical composition of both silicon (Si) and aluminum (Al) oxides, as seen in **Figure 1.11**. AS materials belong to one of the more abundant elements of Earth crust and can be found in a wide range of chains, rings, layers and three-dimensional arrays. They can either be natural or synthetic, crystalline or amorphous, or have different arrangements of atoms and molecules leading to crystalline or amorphous structures with different physicochemical properties. Among the most researched aluminosilicate materials, we can find clays, zeolites and mesoporous aluminosilicates. These materials have excellent mechanical strength, thermal/hydrothermal stability, high surface area, shape-selectivity, and ion-exchange capabilities.[60] Among the many current applications of AS materials we have filtration, [61,62] energy storage,[63–65] catalysis,[16,66,67] mechanical and thermal reinforcement, among many others.

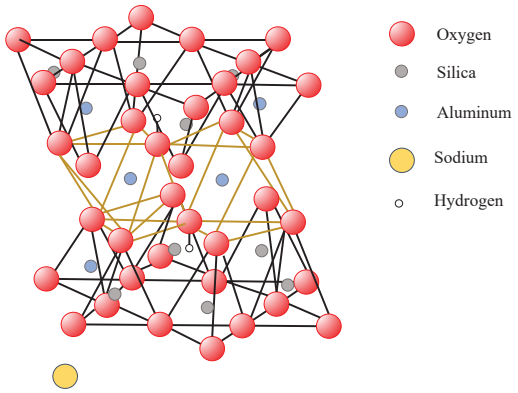

Figure 1.11 Basic chemical aluminosilicate structure

1.2.1 Mesoporous Silica and Aluminosilicates

Supramolecular templating has revolutionized the nanoscopic organization of silica resulting in new microporous materials. Cationic, anionic or nonionic amphiphile molecules act as templates to create these mesostructured materials. [68–70]

The polymorphism of lyotropic mixtures allows for a wide range of morphologies for any material depending on the certain constraints related to their synthetic requirements. Silica and aluminosilicate materials are not the exception. The polar precursors of these materials are capable of dissolving in the water phase of lyotropic mixtures, and several morphologies are possible. Mesoporous silica with hexagonally close-pack arrays and other morphologies are possible by controlling the synthesis conditions (pH, temperature, concentration) and the nature of templates. [71–74]

As discussed before, the surfactant nature and chain length, the nature of the reagents and precursors of the desired material and their interaction with the surfactant molecules are key factors in the control of the evolution of these silica/aluminosilicate materials, however, the significance of each factor may vary depending on the particular system and actual conditions. It is possible to modify the active sites by the introduction of AlO_4 units into the framework or by isomorphously substituting Si^{4+} with other metal cations. [75]

Mesoporous aluminosilicates are promising acid catalysts, however, more research is required since synthesizing well-ordered structures is more complicated than pure silica materials.

1.2.2 Amorphous Aluminosilicates

Amorphous aluminosilicate (a-AS) is an acidic solid consisting of silica and alumina. The conflict between tetrahedral and octahedral coordination, preferable for silicon and aluminum atoms, respectively, makes aluminosilicate amorphous; various shapes are allowed. Therefore, a-AS is a promising constituent for various materials: zeolite precursors, [59, 76, 77] geopolymer precursors, [78–80] supports of solid catalysts [81–84] and heterogeneous solid catalysts.[85–88] These products lead to many industrial applications: aluminosilicate glasses, high-strength fibers, [89] hermetic seals, [90] photonic glass [91] and adsorbents. [92–95]

Substantial research on a-AS synthesis and properties: structure, morphology, and composition, [95–102] shows that their catalytic properties depend mostly on the acidity (Brønsted and Lewis acidity) and morphology. High external surface area (S_{ext}) favors catalytic reactions of bulk molecules, such as cracking and isomerization reactions, [103,104] while acidity control will allow tailor-made catalysts for each application. Combining these two main variables paves the way for new precursors or supports for catalytic materials such as zeolite crystallization precursors and metal catalyst support.

1.2.3 Zeolites

One of the most important members of the aluminosilicate family compounds in the industry and several manufacturing processes are zeolites. These materials are considered as molecular sieves (microporous solids) which are widely used as filtering membranes, ion exchangers and as solid, shape selective Lewis-acid or redox catalysts. They form three-dimensional frameworks of tetrahedral SiO_4 and AlO_4 building units.

Up to now, more than 200 types of zeolites are known and around 100 types of aluminosilicates are available. However, only a few types can be industrially manufactured, due to feasibility and quality issues. The main types of zeolites used in the industry are called the big five of high silica zeolites; FAU (faujasite, USY), *BEA (beta), MOR (high-silica mordenite), MFI (ZSM-5), and FER (high-silica ferrierite) as seen in **Figure 1.14.c**. [105]

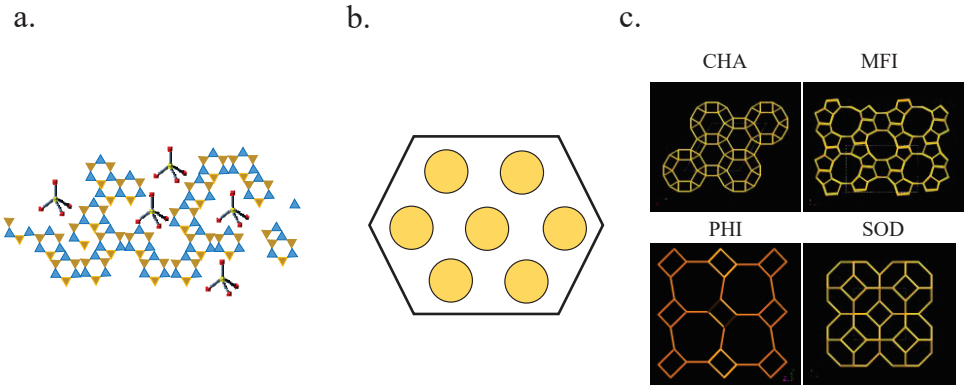

Figure 1.14 Aluminosilicate materials, a) amorphous tetrahedral Si and Al framework without long-rang order, b) mesoporous, c) some Zeolite Framework Types (obtained from the Database of Zeolite Structures, https://www.iza-structure.org/databases/)

1.3 Nanomaterials Catalytic applications

With the advancement of nanotechnology, a wide range of new nanomaterials have been developed and constantly new applications are being research for each of them, especially with the tailoring capacity that nanotechnology allows in the synthesis of said nanomaterials. In this section, we will briefly discuss some of the current applications of the nanomaterials that will be discuss throughout this study.

Aluminosilicate materials have gained great importance in the practical industrial catalysis due to their large specific surface areas, controlled micro and meso pores, adjustable acidity/basicity and depending on morphology, shape-selectivity. And in the case of metals, they can dissociatively adsorb molecules, let the fragments react at their surfaces and allow product molecules to desorb, when becoming nanosized, their specific surface area is considerably increased and their catalytic potential as well. **Table 1.1 and Table 1.2** show some relevant, related and additional catalytic applications for the nanomaterials discussed in this study.

Table 1.1 Catalytic applications for aluminosilicate nanomaterials.

Material	Catalytic Process	Function		Ref. #
Amorphous Aluminosilicate	Catalytic Decomposition	Support for Ni-species in the catalytic decomposition of methane	a-AS nanosheets 2.8 nm thick and mesoporous (45 nm pore size)	Hernandez G. et.al. [106]
	Methane decomposition to CO_x	Catalyst support for Ni-species	a-AS hollow-sphere with 8 – 13 particle size range	Awadallah et. al. [107]
	Upgrading of LTFT waxes	Catalyst support for metal species (Co, Mo, Ni, Pt)	Potential of a-AS as supports for metals in the upgrading of LTFT waxes	Collins et.al, Leckel. [108,109]
	Zeolite synthesis	Dry gel conversion of a-AS.ns precursors into several zeolite frameworks	a-AS.ns of 2 nm thick and 395 nm	Sasaki et.al. [59]
	Hydrocarbon cracking catalysts	Catalyst	Evaluation of the acidity of a-AS for catalytic applications	Holm et.al., Schwarz et.al. [110,111]
Zeolites	Transalkylation	Catalyst	H-MFI	Hernandez G. et.al [112]
	LDPE cracking	Catalyst	MFI	Tsubota et.al., Kokuryo et.al. [113,114]
	Lignin fractionation	Catalyst	Beta-zeolite	Kramarenko et.al, Subbotina et.al. [115,116]
	UOP/Hydro MTO	Catalyst for making light olefins	SAPO-34 (CHA)	Yilmaz et.al. [117]
	Methane-to-benzene	Catalytic upgrading of methane into benzene and H_2 generation over Mo/HZSM-5	HZSM-5 interframework structure of nanosheets 10 – 30 nm	Mishra et.al. [118]

Table 1.2 Catalytic applications for nickel nanoparticles.

Material	Catalytic Process	Function		Ref. #
Ni nanoparticles	Hydrogen generation	Ni-nanoparticles used as a catalyst or as support for CDM	Ni nanosheets comprised of Ni nanoplates with a diameter of 23.2 nm and height of 8.9 nm	Hernandez G. et.al [106]
	Benzene Hydrogenation	Ni hexagonal close-packed and face-centered cubic nanoparticles for hydrogen storage	Ni nanoparticles of 5 – 10 nm	Wegner et.al. [119]
	Water splitting	Ni and NiO nanoparticles loaded in graphen oxide sheets for photocatalytic applications	Ni nanoparticles of 2 – 3 nm	Agegnehu et.al. [120]
	Absorbent in sewage treatment	Ni nanoparticles obtained from the reduction of Ni^{2+} aby $NaBH_4$ for the adsorption of azo dyes.	Ni nanoparticles of 10 – 30 nm	Zhang et.al. [121]
	Chronoamperometric detection of glucose	Ni-based electrode for the detection of glucose	Ni nanoparticles of 2.2 nm – 3.4 nm	Neiva et.al. [122]

1.4 Overview of This Study

As previously stated, nanotechnology has revolutionized most of the known current technologies and has opened the door for the improvement of current processes and the achievement of critical goals that will have an impact on the survival and success of humanity and the achievement of balancing human activities and nature.

In this study, I focus on a specific branch of the synthesis of nanomaterials, soft-templating methodologies, and I further study the potential of surfactants self-assembly as templates for the synthesis of aluminosilicate and other nanomaterials and their catalytic applications. I developed several lyotropic mixtures for the synthesis of a wide range of materials in TRAP's, as seen in **Figure 1.15.**

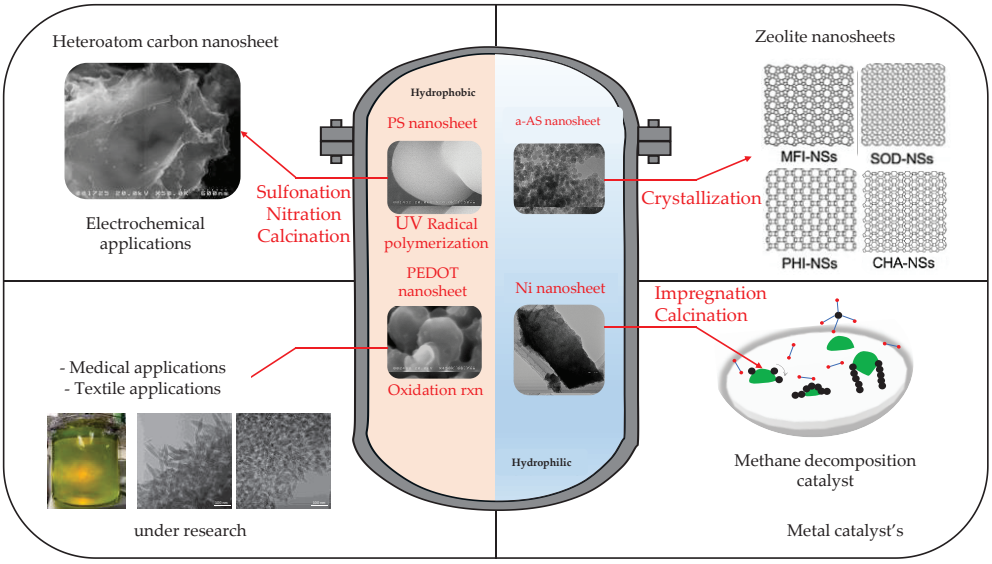

Figure 1.15 Different nanomaterials synthesized in two-dimensional reactor in amphiphilic molecules

In this study, I discuss the synthesis of both amorphous and crystalline aluminosilicate nanomaterials using different lyotropic mixtures and synthetic processes, and I further study their catalytic applications.

There are currently many synthetic methodologies for nanomaterials as well as an innumerable variation of nanomaterials for a wide range of catalytic applications. However, one of the main challenges for soft-templating remains the same, scaling up.

One of the main novelties of this study is that we have selected a rather affordable surfactant Brij L4, as seen in **Table 1.2**, with the hope of developing a soft-templating methodology that could easily be scaled up.

Table 1.2 Price comparison of some surfactants that can achieve lamellar phases.

Surfactant	**Price/100g**
SOBS	¥ 410,000.00
HDPB	¥ 23,000.00
CTAC	¥ 10,100.00
Brij L4	¥ 4,042.00

*Prices obtained from Waken G Online-Shop

To achieve this goal, not only does the surfactant have to be affordable, but the overall synthesis process must be cost-effective. This also includes high quality and homogeneity of the synthesized nanomaterials and the versatility of the system to adapt to several materials.

The controlled synthesis of nanomaterials is still a challenging job. For example, a crucial challenge associated with carbon nanotube synthesis is to achieve chiral selectivity, conductivity, and precisely controlled diameters.[123,124]

In this study I not only focused on the controlled synthesis of aluminosilicate materials, but also was able to synthesize other types of materials using the same TRAP methodology.

By controlling the synthesis conditions, I was also able to decrease the degree of vertical agglomeration which is a common challenge in soft-templating due to physical entanglement electrostatic interactions, or high surface energy. [125]

Figure 1.16 shows a general graphical description of the overview of this study. In Chapter 2, I discussed the control synthesis of amorphous aluminosilicate nanosheets in TRAP's and two main critical variables were identified for the control of the size of amorphous aluminosilicate nanoplates and the aggregated nanosheet and the synthesis of crystalline MFI-type zeolite using the emulsion method (lyotropic mixture of O-15 non-ionic surfactant/water/cyclohexane). Both methods, TRAP and emulsion method can maintain the main characteristics of the synthesized nanomaterials.

In Chapter 3, I focused on the application of amorphous aluminosilicate nanomaterials as supports for nickel oxide particles in the Catalytic Decomposition of Methane (CDM). I further evaluate the effect of the morphology of amorphous aluminosilicates and nickel particles. I devised a new strategy for the synthesis of metallic nanosheet supports for Ni particles with promising catalytic activity in CDM.

Finally, in Chapter 4, I calculated the kinetics of the transalkylation of 4-propylphenol and supercritical benzene over MFI-type zeolite nanomaterials, with improved the overall catalytic performance of this catalyst. Improved desired product yield was obtained due to the natural intrinsic shape-selectivity of two-dimensional sinusoidal channels (5.1 x 5.5 Å) and one-dimensional straight channels (5.3 x 5.6 Å), including two-membered rings (10-Mr) micropore structures, of MFI-type zeolites, which favors the cleavage of C_{aro}-C_{α} carbons and allows to produce phenol and propyl alkyls.

I improved the overall yield of the reaction by transferring the reaction conditions into the reaction controlling conditions region of the reaction by decreasing the diffusion limitations by reduction of the particle size and the improved stability of the reaction was obtained due to reduced coke formation by supercritical conditions.

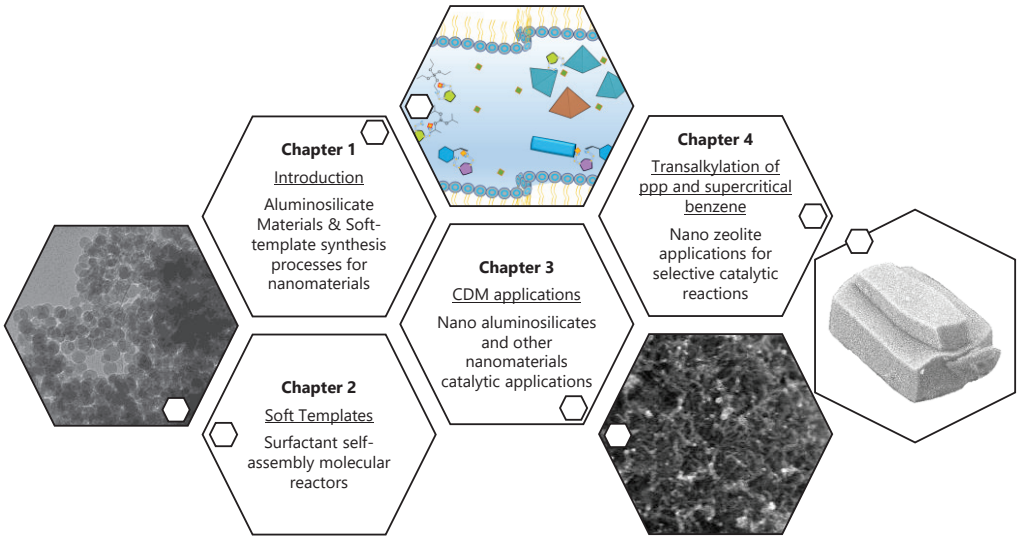

Figure 1.16 This study overview.

Reference

[1] Shapira P, Youtie J. The Economic Contributions of Nanotechnology to Green and Sustainable Growth. Green Processes for Nanotechnology, Cham: Springer International Publishing; 2015, p. 409–34. https://doi.org/10.1007/978-3-319-15461-9_15.

[2] Malik S, Muhammad K, Waheed Y. Nanotechnology: A Revolution in Modern Industry. Molecules 2023;28:661. https://doi.org/10.3390/molecules28020661.

[3] U.S. Census Bureau. NAICS 541713. United States of America: 2017.

[4] Centers for Disease Control and Prevention. CDC COVID Data Tracker 2023. COVID-19 Vaccinations in the United States 2023.

[5] Baig N, Kammakakam I, Falath W, Kammakakam I. Nanomaterials: A review of synthesis methods, properties, recent progress, and challenges. Mater Adv 2021;2:1821–71. https://doi.org/10.1039/d0ma00807a.

[6] Manidurai P, Sekar R. Nanomaterials in Energy Generation. Handbook of Composites from Renewable Materials, Wiley; 2017, p. 207–28. https://doi.org/10.1002/9781119441632.ch155.

[7] Nie R, Li A, Deng X. Environmentally friendly biomaterials as an interfacial layer for highly efficient and air-stable inverted organic solar cells. J Mater Chem A 2014;2:6734–9. https://doi.org/10.1039/C4TA00152D.

[8] Bai P, Zhu G, Lin Z-H, Jing Q, Chen J, Zhang G, et al. Integrated Multilayered Triboelectric Nanogenerator for Harvesting Biomechanical Energy from Human Motions. ACS Nano 2013;7:3713–9. https://doi.org/10.1021/nn4007708.

[9] Casals E, Barrena R, García A, González E, Delgado L, Busquets-Fité M, et al. Programmed Iron Oxide Nanoparticles Disintegration in Anaerobic Digesters Boosts Biogas Production. Small 2014;10:2801–8. https://doi.org/10.1002/smll.201303703.

[10] Chen X, Xu S, Yao N, Shi Y. 1.6 V Nanogenerator for Mechanical Energy Harvesting Using PZT Nanofibers. Nano Lett 2010;10:2133–7. https://doi.org/10.1021/nl100812k.

[11] Grätzel M. Solar Energy Conversion by Dye-Sensitized Photovoltaic Cells. Inorg Chem 2005;44:6841–51. https://doi.org/10.1021/ic0508371.

[12] Keis K, Magnusson E, Lindström H, Lindquist S-E, Hagfeldt A. A 5% efficient photoelectrochemical solar cell based on nanostructured ZnO electrodes. Solar Energy Materials and Solar Cells 2002;73:51–8. https://doi.org/10.1016/S0927-0248(01)00110-6.

[13] Li Y, Park SY, Zhu J. Solid-state anaerobic digestion for methane production from organic waste. Renewable and Sustainable Energy Reviews 2011;15:821–6. https://doi.org/10.1016/j.rser.2010.07.042.

[14] Siddiqui S, Kim D-I, Duy LT, Nguyen MT, Muhammad S, Yoon W-S, et al. High-performance flexible lead-free nanocomposite piezoelectric nanogenerator for biomechanical energy harvesting and storage. Nano Energy 2015;15:177–85. https://doi.org/10.1016/j.nanoen.2015.04.030.

[15] Konuklu Y, Paksoy HO, Unal M. Nanoencapsulation of n-alkanes with poly(styrene-co-ethylacrylate) shells for thermal energy storage. Appl Energy 2015;150:335–40. https://doi.org/10.1016/j.apenergy.2014.11.066.

[16] Gaitan JAH, Nakasaka Y, Yoshikawa T, Nishiyama N, Masuda T. Catalytic transalkylation of alkylphenol to phenol in supercritical benzene fluid over MFI type zeolite in a fixed-bed reactor: Diffusion and reaction limitations. Chemical Engineering Journal 2023;464:142618. https://doi.org/10.1016/j.cej.2023.142618.

[17] Lu Q, Wei X-Z, Zhang Q, Zhang X, Chen L, Liu J, et al. Efficient selective hydrogenation of terminal alkynes over Pd–Ni nanoclusters encapsulated inside S-1 zeolite. Microporous and Mesoporous Materials 2024;365:112883. https://doi.org/10.1016/j.micromeso.2023.112883.

[18] Rafiani A, Aulia D, Kadja GTM. Zeolite-encapsulated catalyst for the biomass conversion: Recent and upcoming advancements. Case Studies in Chemical and Environmental Engineering 2024;9:100717. https://doi.org/10.1016/j.cscee.2024.100717.

[19] Vassilina G, Umbetkaliyeva K, Abdrassilova A, Vassilina T, Zakirov Z. The mesoporous aluminosilicate application as support for bifunctional catalysts for *n* -hexadecane hydroconversion. Open Chem 2022;20:225–36. https://doi.org/10.1515/chem-2022-0134.
[20] Xu L, Liu Z, Li Z, Liu J, Ma Y, Guan J, et al. Non-crystalline mesoporous aluminosilicates catalysts: Synthesis, characterization and catalytic applications. J Non Cryst Solids 2011;357:1335–41. https://doi.org/10.1016/j.jnoncrysol.2010.12.028.
[21] Xu D, Lv H, Liu B. Encapsulation of Metal Nanoparticle Catalysts Within Mesoporous Zeolites and Their Enhanced Catalytic Performances: A Review. Front Chem 2018;6. https://doi.org/10.3389/fchem.2018.00550.
[22] Wang Z, Du C, Zhu L, Wang Z. Retention Performance of Al2o3 Plot Column Coated with Γ–Alumina Nanoparticles in the Highly Volatile Hydrocarbons Separation. SSRN Electronic Journal 2022. https://doi.org/10.2139/ssrn.4208773.
[23] Khan WA, Arain MB, Soylak M. Nanomaterials-based solid phase extraction and solid phase microextraction for heavy metals food toxicity. Food and Chemical Toxicology 2020;145:111704. https://doi.org/10.1016/j.fct.2020.111704.
[24] Jia Z, Du C, Zhu L, Wang Z. Retention performance of alumina porous layer open-tubular column coated with γ–alumina nanoparticles in the highly volatile hydrocarbons separation. J Chromatogr A 2023;1687:463657. https://doi.org/10.1016/j.chroma.2022.463657.
[25] Minakshi P, Ghosh M, Brar B, Ranjan K, Patki HS, Kumar R. Separation techniques with nanomaterials. Handbook of Nanomaterials in Analytical Chemistry, Elsevier; 2020, p. 99–158. https://doi.org/10.1016/B978-0-12-816699-4.00006-2.
[26] Ozcakir G. Applications of Nanomaterials in Food Industry: A Review. IOCN 2023, Basel Switzerland: MDPI; 2023, p. 22. https://doi.org/10.3390/IOCN2023-14470.
[27] Kodithuwakku P, Jayasundara DR, Munaweera I, Jayasinghe R, Thoradeniya T, Weerasekera M, et al. A review on recent developments in structural modification of TiO2 for food packaging applications. Progress in Solid State Chemistry 2022;67:100369. https://doi.org/10.1016/j.progsolidstchem.2022.100369.
[28] Lu N, Chen Z, Song J, Weng Y, Yang G, Liu Q, et al. Size Effect of TiO2 Nanoparticles as Food Additive and Potential Toxicity. Food Biophys 2022;17:75–83. https://doi.org/10.1007/s11483-021-09695-7.
[29] Raul PK, Thakuria A, Das B, Devi RR, Tiwari G, Yellappa C, et al. Carbon Nanostructures As Antibacterials and Active Food-Packaging Materials: A Review. ACS Omega 2022;7:11555–9. https://doi.org/10.1021/acsomega.2c00848.
[30] Goh K, Heising JK, Yuan Y, Karahan HE, Wei L, Zhai S, et al. Sandwich-Architectured Poly(lactic acid)–Graphene Composite Food Packaging Films. ACS Appl Mater Interfaces 2016;8:9994–10004. https://doi.org/10.1021/acsami.6b02498.
[31] Liu L, Li Y, Zhan L, Liu Y, Huang C. One-step synthesis of fluorescent hydroxyls-coated carbon dots with hydrothermal reaction and its application to optical sensing of metal ions. Sci China Chem 2011;54:1342–7. https://doi.org/10.1007/s11426-011-4351-6.
[32] Zhou L, Lin Y, Huang Z, Ren J, Qu X. Carbon nanodots as fluorescence probes for rapid, sensitive, and label-free detection of Hg^{2+} and biothiols in complex matrices. Chem Commun 2012;48:1147–9. https://doi.org/10.1039/C2CC16791C.
[33] Bayda S, Hadla M, Palazzolo S, Kumar V, Caligiuri I, Ambrosi E, et al. Bottom-up synthesis of carbon nanoparticles with higher doxorubicin efficacy. Journal of Controlled Release 2017;248:144–52. https://doi.org/10.1016/j.jconrel.2017.01.022.
[34] Cao L, Wang X, Meziani MJ, Lu F, Wang H, Luo PG, et al. Carbon Dots for Multiphoton Bioimaging. J Am Chem Soc 2007;129:11318–9. https://doi.org/10.1021/ja073527l.
[35] Knoll AW, Pires D, Coulembier O, Dubois P, Hedrick JL, Frommer J, et al. Probe-Based 3-D Nanolithography Using Self-Amplified Depolymerization Polymers. Advanced Materials 2010;22:3361–5. https://doi.org/10.1002/adma.200904386.
[36] Li Q, Ohulchanskyy TY, Liu R, Koynov K, Wu D, Best A, et al. Photoluminescent Carbon Dots as Biocompatible Nanoprobes for Targeting Cancer Cells *in Vitro*. The Journal of Physical Chemistry C 2010;114:12062–8. https://doi.org/10.1021/jp911539r.

[37] Xie Y, Kocaefe D, Chen C, Kocaefe Y. Review of Research on Template Methods in Preparation of Nanomaterials. J Nanomater 2016;2016:1–10. https://doi.org/10.1155/2016/2302595.
[38] Poolakkandy RR, Menamparambath MM. Soft-template-assisted synthesis: a promising approach for the fabrication of transition metal oxides. Nanoscale Adv 2020;2:5015–45. https://doi.org/10.1039/D0NA00599A.
[39] Poolakkandy RR, Menamparambath MM. Soft-template-assisted synthesis: a promising approach for the fabrication of transition metal oxides. Nanoscale Adv 2020;2:5015–45. https://doi.org/10.1039/D0NA00599A.
[40] Liu Y, Goebl J, Yin Y. Templated synthesis of nanostructured materials. Chem Soc Rev 2013;42:2610–53. https://doi.org/10.1039/C2CS35369E.
[41] Perinelli DR, Cespi M, Lorusso N, Palmieri GF, Bonacucina G, Blasi P. Surfactant Self-Assembling and Critical Micelle Concentration: One Approach Fits All? Langmuir 2020;36:5745–53. https://doi.org/10.1021/acs.langmuir.0c00420.
[42] Del Regno A, Warren PB, Bray DJ, Anderson RL. Critical Micelle Concentrations in Surfactant Mixtures and Blends by Simulation. J Phys Chem B 2021;125:5983–90. https://doi.org/10.1021/acs.jpcb.1c00893.
[43] Li H, Hu D, Liang F, Huang X, Zhu Q. Influence factors on the critical micelle concentration determination using pyrene as a probe and a simple method of preparing samples. R Soc Open Sci 2020;7:192092. https://doi.org/10.1098/rsos.192092.
[44] Shinoda K, Nakagawa T. Colloidal Surfactants. vol. 12. Elsevier; 1963. https://doi.org/10.1016/C2013-0-12170-8.
[45] Mazer NA, Benedek GB, Carey MC. An investigation of the micellar phase of sodium dodecyl sulfate in aqueous sodium chloride solutions using quasielastic light scattering spectroscopy. J Phys Chem 1976;80:1075–85. https://doi.org/10.1021/j100551a011.
[46] Tolédano P, Neto AMF. Phase Transitions in Complex Fluids. WORLD SCIENTIFIC; 1998. https://doi.org/10.1142/3591.
[47] Tschierske C, Photinos DJ. Biaxial nematic phases. J Mater Chem 2010;20:4263. https://doi.org/10.1039/b924810b.
[48] Bruce DW, Wali MA, Wang QM. Calamitic nematic liquid crystal phases from Zn II complexes of 5, 15-disubstituted porphyrins. J Chem Soc Chem Commun 1994:2089. https://doi.org/10.1039/c39940002089.
[49] Bisoyi HK, Kumar S. Discotic nematic liquid crystals: science and technology. Chem Soc Rev 2010;39:264–85. https://doi.org/10.1039/B901792P.
[50] Zhou H, Wang H, He W, Yang Z, Cao H, Wang D, et al. Research Progress of Cholesteric Liquid Crystals with Broadband Reflection. Molecules 2022;27:4427. https://doi.org/10.3390/molecules27144427.
[51] Tago T, Nishi M, Kouno Y, Masuda T. New Method for Preparing Monodispersed Nanocrystalline Silicalite via Hydrothermal Synthesis in Water/Surfactant/Oil Solution. Chem Lett 2004;33:1040–1. https://doi.org/10.1246/cl.2004.1040.
[52] Tago T. Template-free Synthesis for Nano-crystalline Zeolite. Hosokawa Powder Technology Foundation ANNUAL REPORT 2010;18:67–73. https://doi.org/10.14356/hptf.08108.
[53] Tago T, Iwakai K, Nishi M, Masuda T. Synthesis of Mono-Dispersed Silicalite-1 Nanocrystals in Water-Surfactant-Organic Solvent. J Nanosci Nanotechnol 2009;9:612–7. https://doi.org/10.1166/jnn.2009.J068.
[54] Tago T, Nakasaka Y, Masuda T. Synthesis of Nano-crystalline Zeolites and Applications to Zeolite Membranes. Journal of the Japan Petroleum Institute 2012;55:149–59. https://doi.org/10.1627/jpi.55.149.
[55] Sasaki K, Okue T, Shu Y, Miyake K, Uchida Y, Nishiyama N. Thin ZIF-8 nanosheets synthesized in hydrophilic TRAPs. Dalton Transactions 2021;50:10394–9. https://doi.org/10.1039/d1dt01507a.
[56] Uchida Y, Nishizawa T, Omiya T, Hirota Y, Nishiyama N. Nanosheet Formation in Hyperswollen Lyotropic Lamellar Phases. J Am Chem Soc 2016;138:1103–5. https://doi.org/10.1021/jacs.5b11256.

[57] Zhao JH, Tan RQ, Yang Y, Xu W, Li J, Shen WF, et al. Synthesis mechanism of nanoporous Sn3O4 nanosheets by hydrothermal process without any additives. Chinese Physics B 2015;24. https://doi.org/10.1088/1674-1056/24/6/066202.
[58] Sasaki K, Okue T, Nakai T, Uchida Y, Nishiyama N. Lateral Growth of Uniformly Thin Gold Nanosheets Facilitated by Two-Dimensional Precursor Supply. Langmuir 2021;37:5872–7. https://doi.org/10.1021/acs.langmuir.1c00344.
[59] Sasaki K, Gaitan JAH, Okue T, Matoba S, Tokuda Y, Miyake K, et al. 1. Amorphous Aluminosilicate Nanosheets as Universal Precursors for the Synthesis of Diverse Zeolite Nanosheets for Polymer-Cracking Reactions. Angewandte Chemie - International Edition 2022;61. https://doi.org/10.1002/anie.202213773.
[60] Lopes AC, Martins P, Lanceros-Mendez S. Aluminosilicate and aluminosilicate based polymer composites: Present status, applications and future trends. Prog Surf Sci 2014;89:239–77. https://doi.org/10.1016/j.progsurf.2014.08.002.
[61] Saffaj N, Persin M, Younsi SA, Albizane A, Cretin M, Larbot A. Elaboration and characterization of microfiltration and ultrafiltration membranes deposited on raw support prepared from natural Moroccan clay: Application to filtration of solution containing dyes and salts. Appl Clay Sci 2006;31:110–9. https://doi.org/10.1016/j.clay.2005.07.002.
[62] Ulbricht M. Advanced functional polymer membranes. Polymer (Guildf) 2006;47:2217–62. https://doi.org/10.1016/j.polymer.2006.01.084.
[63] Arora P, Zhang Z (John). Battery Separators. Chem Rev 2004;104:4419–62. https://doi.org/10.1021/cr020738u.
[64] Wang WS, Chen HS, Wu YW, Tsai TY, Chen-Yang YW. Properties of novel epoxy/clay nanocomposites prepared with a reactive phosphorus-containing organoclay. Polymer (Guildf) 2008;49:4826–36. https://doi.org/10.1016/j.polymer.2008.08.019.
[65] Son D-H, Sharma RK, Shul Y-G, Kim H. Preparation of Pt/zeolite–Nafion composite membranes for self-humidifying polymer electrolyte fuel cells. J Power Sources 2007;165:733–8. https://doi.org/10.1016/j.jpowsour.2006.11.090.
[66] Parton RF, Vankelecom IFJ, Casselman MJA, Bezoukhanova CP, Uytterhoeven JB, Jacobs PA. An efficient mimic of cytochrome P-450 from a zeolite-encaged iron complex in a polymer membrane. Nature 1994;370:541–4. https://doi.org/10.1038/370541a0.
[67] Teng H, Wang J, Chen D, Liu P, Wang X. Silicalite-1 membrane on millimeter-sized HZSM-5 zeolite extrudates: Controllable synthesis and catalytic behavior in toluene disproportionation. J Memb Sci 2011;381:197–203. https://doi.org/10.1016/j.memsci.2011.07.025.
[68] Lin H-P, Mou C-Y. Structural and Morphological Control of Cationic Surfactant-Templated Mesoporous Silica. Acc Chem Res 2002;35:927–35. https://doi.org/10.1021/ar000074f.
[69] Ying JY, Mehnert CP, Wong MS. Synthesis and Applications of Supramolecular-Templated Mesoporous Materials. Angewandte Chemie International Edition 1999;38:56–77. https://doi.org/10.1002/(SICI)1521-3773(19990115)38:1/2<56::AID-ANIE56>3.0.CO;2-E.
[70] Hunks WJ, Ozin GA. Periodic Mesoporous Organosilicas with Phenylene Bridging Groups, 1,4-$(CH_2)_n C_6 H_4$ (n = 0–2). Chemistry of Materials 2004;16:5465–72. https://doi.org/10.1021/cm048986p.
[71] Corma A. From Microporous to Mesoporous Molecular Sieve Materials and Their Use in Catalysis. Chem Rev 1997;97:2373–420. https://doi.org/10.1021/cr960406n.
[72] Ciesla U, Schüth F. Ordered mesoporous materials. Microporous and Mesoporous Materials 1999;27:131–49. https://doi.org/10.1016/S1387-1811(98)00249-2.
[73] Stein A, Melde BJ, Schroden RC. Hybrid Inorganic-Organic Mesoporous Silicates—Nanoscopic Reactors Coming of Age. Advanced Materials 2000;12:1403–19. https://doi.org/10.1002/1521-4095(200010)12:19<1403::AID-ADMA1403>3.0.CO;2-X.
[74] Zhao XS, Lu GQ (Max), Millar GJ. Advances in Mesoporous Molecular Sieve MCM-41. Ind Eng Chem Res 1996;35:2075–90. https://doi.org/10.1021/ie950702a.
[75] Abdelhamid Sayari. Catalysis by Crystalline Mesoporous Molecular Sieves. Chemistry of Materials 1996;8:1840–52.

[76] Guo H, Zhao L, Martineau-Corcos C, Fayon F, Viger-Gravel J, Awala H, et al. 2. Transformation of Discrete Amorphous Aluminosilicate Nanoparticles into Nanosized Zeolites. Adv Mater Interfaces 2021;8. https://doi.org/10.1002/admi.202000634.
[77] Grand J, Awala H, Mintova S. 3. Mechanism of zeolites crystal growth: New findings and open questions. CrystEngComm 2016;18:650–64. https://doi.org/10.1039/c5ce02286j.
[78] Castillo H, Collado H, Droguett T, Vesely M, Garrido P, Palma S. 4. State of the art of geopolymers: A review. E-Polymers 2022;22:108–24. https://doi.org/10.1515/epoly-2022-0015.
[79] Mackenzie KJD, Welter M. 5. Geopolymer (aluminosilicate) composites: synthesis, properties and applications. Advances in Ceramic Matrix Composites, Elsevier; 2014, p. 445–70. https://doi.org/10.1533/9780857098825.3.445.
[80] Zain-ul-abdein M, Ahmed F, Channa IA, Makhdoom MA, Ali R, Ehsan M, et al. 6. Synthesis of Geopolymer from a Novel Aluminosilicate-Based Natural Soil Precursor Using Electric Oven Curing for Improved Mechanical Strength. Materials 2022;15. https://doi.org/10.3390/ma15217757.
[81] Shee Ween O, Cheng-Yong H, Mustafa Al Bakri Abdullah M, Ho LN, Wan En O. 7. Geopolymer via Pressing Method: Aluminosilicates/Alkaline Solution Ratio as the Determining Factor. IOP Conf Ser Mater Sci Eng, vol. 864, IOP Publishing Ltd; 2020. https://doi.org/10.1088/1757-899X/864/1/012164.
[82] Caillot M, Chaumonnot A, Digne M, Poleunis C, Debecker DP, Van Bokhoven JA. 8. Synthesis of amorphous aluminosilicates by grafting: Tuning the building and final structure of the deposit by selecting the appropriate synthesis conditions. Microporous and Mesoporous Materials 2014;185:179–89. https://doi.org/10.1016/j.micromeso.2013.10.032.
[83] Samad JE, Blanchard J, Sayag C, Louis C, Regalbuto JR. 9. The controlled synthesis of metal-acid bifunctional catalysts: Selective Pt deposition and nanoparticle synthesis on amorphous aluminosilicates. J Catal 2016;342:213–25. https://doi.org/10.1016/j.jcat.2016.08.002.
[84] Ogorzały K, Jajko G, Korzeniowska A, Mazur M, Li A, Roth WJ, et al. 10. The effect of amorphous silica support on the catalytic activity of liquid-exfoliated monolayered MCM-56 zeolite. Journal of Porous Materials 2023. https://doi.org/10.1007/s10934-023-01433-3.
[85] Caillot M, Chaumonnot A, Digne M, Van Bokhoven JA. 12. The variety of Brønsted acid sites in amorphous aluminosilicates and zeolites. J Catal 2014;316:47–56. https://doi.org/10.1016/j.jcat.2014.05.002.
[86] Maity A, Chaudhari S, Titman JJ, Polshettiwar V. 14. Catalytic nanosponges of acidic aluminosilicates for plastic degradation and CO2 to fuel conversion. Nat Commun 2020;11. https://doi.org/10.1038/s41467-020-17711-6.
[87] Styskalik A, Abbott JG, Orick MC, Debecker DP, Barnes CE. 13. Synthesis, characterization and catalytic activity of single site, Lewis acidic aluminosilicates. Catal Today 2019;334:131–9. https://doi.org/10.1016/j.cattod.2018.11.079.
[88] Locus R, Verboekend D, d'Halluin M, Dusselier M, Liao Y, Nuttens N, et al. 15. Synthetic and Catalytic Potential of Amorphous Mesoporous Aluminosilicates Prepared by Postsynthetic Aluminations of Silica in Aqueous Media. ChemCatChem 2018;10:1385–97. https://doi.org/10.1002/cctc.201701660.
[89] Chen C, Zhu Q, Wang H, Huang F, Yang Q, Xu S. 16. Excellent Mechanical Properties of the Silicate Glasses Modified by CeO 2 and TiO 2 : a New Choice for High-Strength and High-Modulus Glass Fibers n.d. https://doi.org/10.1007/s12633-021-01215-z/Published.
[90] Goel A, Reddy AA, Pascual MJ, Gremillard L, Malchere A, Ferreira JMF. Sintering behavior of lanthanide-containing glass-ceramic sealants for solid oxide fuel cells. J Mater Chem 2012;22:10042. https://doi.org/10.1039/c2jm16300d.
[91] Sen S, Rakhmatullin R, Gubaidullin R, Pöppl A. 20. Direct spectroscopic observation of the atomic-scale mechanisms of clustering and homogenization of rare-earth dopant ions in vitreous silica. Phys Rev B Condens Matter Mater Phys 2006;74. https://doi.org/10.1103/PhysRevB.74.100201.
[92] Yokoyama T, Ueda A, Kato K, Mogi K, Matsuo S. 21. A study of the alumina-silica gel

adsorbent for the removal of silicic acid from geothermal water: Increase in adsorption capacity of the adsorbent due to formation of amorphous aluminosilicate by adsorption of silicic acid. J Colloid Interface Sci 2002;252:1–5. https://doi.org/10.1006/jcis.2002.8382.

[93] Suzuki M, Nakanishi R, Inukai K, Maeda M, Hiradate S, Tsukimura K. 22. A New Amorphous Aluminum-Silicate : High Performance Adsorbent for Water Vapor and Carbon Dioxide. n.d.

[94] Wang S, Li L, Zhu ZH. 23. Solid-state conversion of fly ash to effective adsorbents for Cu removal from wastewater. J Hazard Mater 2007;139:254–9. https://doi.org/10.1016/j.jhazmat.2006.06.018.

[95] Li L, Wang S, Zhu Z. 24. Geopolymeric adsorbents from fly ash for dye removal from aqueous solution. J Colloid Interface Sci 2006;300:52–9. https://doi.org/10.1016/j.jcis.2006.03.062.

[96] Gammond L V.D., Youngman RE, Zeidler A, Aitken BG, Salmon PS. 25. Structural model for amorphous aluminosilicates. Journal of Chemical Physics 2022;156. https://doi.org/10.1063/5.0079607.

[97] Goldsmith BR, Peters B, Johnson JK, Gates BC, Scott SL. 26. Beyond Ordered Materials: Understanding Catalytic Sites on Amorphous Solids. ACS Catal 2017;7:7543–57. https://doi.org/10.1021/acscatal.7b01767.

[98] Trombetta M, Busca G, Rossini S, Piccoli V, Cornaro U, Guercio A, et al. 27. FT-IR Studies on Light Olefin Skeletal Isomerization Catalysis III. Surface Acidity and Activity of Amorphous and Crystalline Catalysts Belonging to the SiO 2-Al 2 O 3 System. vol. 179. 1998.

[99] Fernández-Jiménez A, Vallepu R, Terai T, Palomo A, Ikeda K. 28. Synthesis and thermal behavior of different aluminosilicate gels. J Non Cryst Solids 2006;352:2061–6. https://doi.org/10.1016/j.jnoncrysol.2006.03.037.

[100] Hartati H, Purwaningsih A, Tjahjandarie TS, Saputri NH, Puspitasari IS, Lamanele CN, et al. 29. Synthesis of amorphous aluminosilicate from impure Indonesian kaolin. Open Chem 2020;18:295–302. https://doi.org/10.1515/chem-2020-0033.

[101] Reif P, Gupta NK, Rose M. 30. Highly stable amorphous silica-alumina catalysts for continuous bio-derived mesitylene production under solvent-free conditions. Green Chemistry 2023;25:1588–96. https://doi.org/10.1039/d2gc04116b.

[102] Kosanović C, Bosnar S, Subotić B, Svetličić V, Mišić T, Dražić G, et al. 31. Study of the microstructure of amorphous aluminosilicate gel before and after its hydrothermal treatment. Microporous and Mesoporous Materials 2008;110:177–85. https://doi.org/10.1016/j.micromeso.2007.06.007.

[103] Msheik M, Rodat S, Abanades S. 32. Methane Cracking for Hydrogen Production: A Review of Catalytic and Molten Media Pyrolysis energies Methane Cracking for Hydrogen Production: A Review of Catalytic and Molten Media Pyrolysis 2021. https://doi.org/10.3390/en14113107ï.

[104] Gallo P Del, Meunier R, Pham-Huu C, Crouzet C, Ledoux MJ. 33. Selective n-Butane Isomerization over High Specific Surface Area MoO 3-Carbon-Modified Catalyst. 1997.

[105] Bingre R, Louis B, Nguyen P. An Overview on Zeolite Shaping Technology and Solutions to Overcome Diffusion Limitations. Catalysts 2018;8:163. https://doi.org/10.3390/catal8040163.

[106] Gaitan, J. A. H., Li, X., Tamura, K., Miyake, K., Uchida, Y., & Nishiyama, N. (2024). Ni Particle Morphology and Support Effect in the Catalytic Decomposition of Methane: Into the Design of Novel, High Yield Catalyst for Catalytic Decomposition of Methane. Advanced Energy and Sustainability Research. https://doi.org/10.1002/aesr.202400096

[107] A.E. Awadallah, W. Ahmed, M.R.N. El-Din, A.A. Aboul-Enein, Novel aluminosilicate hollow sphere as a catalyst support for methane decomposition to COx-free hydrogen production, Appl Surf Sci 287 (2013) 415–422. https://doi.org/10.1016/j.apsusc.2013.09.173.

[108] Collins, J. P., Font Freide, J. J. H. M., & Nay, B. (2006). A History of Fischer-Tropsch Wax Upgrading at BP—from Catalyst Screening Studies to Full Scale Demonstration in Alaska. Journal of Natural Gas Chemistry, 15(1), 1–10. https://doi.org/10.1016/S1003-9953(06)60001-7

[109] Leckel, D. (2007). Noble Metal Wax Hydrocracking Catalysts Supported on High-Siliceous

Alumina. Industrial & Engineering Chemistry Research, 46(11), 3505–3512. https://doi.org/10.1021/ie0700922

[110] Holm, V. C. F., Bailey, G. C., & Clark, A. (1959). Acidity Studies of Silica-Alumina Catalysts. The Journal of Physical Chemistry, 63(2), 129–133. https://doi.org/10.1021/j150572a001

[111] Schwarz, J. (1978). A study of pyridine adsorbed on silica-alumina catalysts by combined infrared spectroscopy and temperature-programmed desorption. Journal of Catalysis, 54(3), 303–317. https://doi.org/10.1016/0021-9517(78)90079-9

[112] Gaitan, J. A. H., Nakasaka, Y., Yoshikawa, T., Nishiyama, N., & Masuda, T. (2023). Catalytic transalkylation of alkylphenol to phenol in supercritical benzene fluid over MFI type zeolite in a fixed-bed reactor: Diffusion and reaction limitations. Chemical Engineering Journal, 464, 142618. https://doi.org/10.1016/j.cej.2023.142618

[113] Tsubota, S., Kokuryo, S., Tamura, K., Miyake, K., Uchida, Y., Mizusawa, A., Kubo, T., & Nishiyama, N. (2024). Exploring the effect of Brønsted acidity of MFI-type zeolites on catalytic cracking temperature of low density polyethylene. Catalysis Science & Technology, 14(5), 1369–1374. https://doi.org/10.1039/D3CY01622F

[114] Kokuryo, S., Miyake, K., Uchida, Y., Tanaka, S., Miyamoto, M., Oumi, Y., Mizusawa, A., Kubo, T., & Nishiyama, N. (2022). Design of Zr- and Al-Doped *BEA-Type Zeolite to Boost LDPE Cracking. ACS Omega, 7(15), 12971–12977. https://doi.org/10.1021/acsomega.2c00283

[115] Kramarenko, A., Etit, D., Laudadio, G., & D'Angelo, F. N. (2021). β - Zeolite - Assisted Lignin - First Fractionation in a Flow - Through Reactor**. ChemSusChem, 14(18), 3838–3849. https://doi.org/10.1002/cssc.202101157

[116] Subbotina, E., Velty, A., Samec, J. S. M., & Corma, A. (2020). Zeolite - Assisted Lignin - First Fractionation of Lignocellulose: Overcoming Lignin Recondensation through Shape - Selective Catalysis. ChemSusChem, 13(17), 4528 – 4536. https://doi.org/10.1002/cssc.202000330

[117] Yilmaz, B., & Müller, U. (2009). Catalytic Applications of Zeolites in Chemical Industry. Topics in Catalysis, 52(6–7), 888–895. https://doi.org/10.1007/s11244-009-9226-0

[118] Mishra, D., Modak, A., Pant, K. K., & Zhao, X. S. (2022). Improved benzene selectivity for methane dehydroaromatization via modifying the zeolitic pores by dual-templating approach. Microporous and Mesoporous Materials, 344, 112172. https://doi.org/10.1016/j.micromeso.2022.112172

[119] Wegner, S., Rutz, C., Schütte, K., Barthel, J., Bushmelev, A., Schmidt, A., Dilchert, K., Fischer, R. A., & Janiak, C. (2017). Soft, Wet - Chemical Synthesis of Metastable Superparamagnetic Hexagonal Close - Packed Nickel Nanoparticles in Different Ionic Liquids. Chemistry – A European Journal, 23(26), 6330–6340. https://doi.org/10.1002/chem.201605251

[120] Agegnehu, A. K., Pan, C.-J., Rick, J., Lee, J.-F., Su, W.-N., & Hwang, B.-J. (2012). Enhanced hydrogen generation by cocatalytic Ni and NiO nanoparticles loaded on graphene oxide sheets. Journal of Materials Chemistry, 22(27), 13849. https://doi.org/10.1039/c2jm30474k

[121] Zhang, G., Li, J., Zhang, G., & Zhao, L. (2015). Room-Temperature Synthesis of Ni Nanoparticles as the Absorbent Used for Sewage Treatment. Advances in Materials Science and Engineering, 2015, 1–4. https://doi.org/10.1155/2015/973648

[122] Neiva, E. G. C., Bergamini, M. F., Oliveira, M. M., Marcolino, L. H., & Zarbin, A. J. G. (2014). PVP-capped nickel nanoparticles: Synthesis, characterization and utilization as a glycerol electrosensor. Sensors and Actuators B: Chemical, 196, 574–581. https://doi.org/10.1016/j.snb.2014.02.041

[123] Li, Z., Xiao, M., Jin, C., & Zhang, Z. (2023). Toward the Commercialization of Carbon Nanotube Field Effect Transistor Biosensors. Biosensors, 13(3), 326. https://doi.org/10.3390/bios13030326

[124] Yang, F., Wang, X., Zhang, D., Yang, J., Luo, D., Xu, Z., Wei, J., Wang, J.-Q., Xu, Z., Peng, F., Li, X., Li, R., Li, Y., Li, M., Bai, X., Ding, F., & Li, Y. (2014). Chirality-specific growth of single-

walled carbon nanotubes on solid alloy catalysts. Nature, 510(7506), 522–524. https://doi.org/10.1038/nature13434

[125] Vandenabeele, C. R., & Lucas, S. (2020). Technological challenges and progress in nanomaterials plasma surface modification – A review. Materials Science and Engineering: R: Reports, 139, 100521. https://doi.org/10.1016/j.mser.2019.100521

Chapter 2

Synthesis of Aluminosilicate Nanoparticles

2.1 Introduction

As previously stated in Chapter I, aluminosilicates (AS) materials share a basic chemical composition of both silicon (Si) and aluminum (Al) oxides and have a wide range of applications. AS catalytic properties depend mostly on the acidity (Brønsted and Lewis acidity) and morphology. High external surface area (S_{ext}) favors catalytic reactions of bulk molecules, such as cracking and isomerization reactions,[1,2] while acidity control will allow tailor-made catalysts for each application. Combining these two main variables paves the way for new precursors or supports for catalytic materials such as zeolite crystallization precursors and metal catalyst support.[3–10]

2.1.1 MFI-type Nanospheres

Open-framework aluminosilicate materials with orderly distributed micropores (zeolites) have unique characteristics such as lower diffusion resistance, shape-selectivity, tailored active sites and high hydrothermal stability and low production costs, makes them materials in several industries. Most important heterogeneous catalysts in petrochemical industries and promising conversion of sustainable feedstock into high-value biofuels and platform chemicals.[11,12]

MFI-type zeolite catalyst shows great promise for several selective reactions such as cracking of alkanes[13–15] and transalkylation, [16–18] alkylation of aromatics,[19,20] and synthesis of olefins from alcohol and acetone.[20,21] However, a rate-limiting step of these type of reactions is the diffusion of the reactant/product molecules within the zeolite micropores. Hence, nano-size zeolites are a promising solution to achieve low diffusion resistance, because the diffusion length for the reactant/products decreases, together with the reduction of the zeolite crystal size.[20–22] In order to improve the efficiency of MFI-type zeolite catalyst, two main approaches have been studied; formation of meso-pores,[23–29] and the preparation of nano-crystalline zeolites.[30–38] In this study, I focus on the latter.

Nano-crystalline zeolites diffusion limitations decrease thanks to the decrease in the diffusion length, directly correlated to the crystal size, which also increases the outer surface area of these nanomaterials. Several methods for the synthesis of nano-crystalline zeolites have been reported. [39,40]

In this chapter, I focus on the synthetic approaches for aluminosilicate nanomaterials using soft-template methods. Both amorphous and crystalline aluminosilicate materials were synthesized using TRAP's and emulsion method, respectively. In the following chapters, I will discuss some catalytic applications for these materials from the many applications they can be used.

2.2 Experimental

2.2.1 Materials

Tetraethyl orthosilicate (TEOS, Wako Pure Chemicals Co.), aluminum isopropoxide (AIP, Nacalai Tesque Inc.), sodium hydroxide (NaOH, Wako Pure Chemicals Co.), polyethylene glycol dodecyl ether (Brij L4, Sigma-Aldrich Co.), methanol (Wako Pure Chemicals Co.), heptane (Wako Pure Chemicals Co.), tetra-n-propyl ammonium hydroxide solution (abt. 10.0%V) (TPA-OH, Sigma-Aldrich Co.), sodium chloride (NaCl, Sigma-Aldrich Co), Ammonium Nitrate (NH_4NO_3, Sigma-Aldrich Co.), and deionized water were used without further purification to prepare amorphous aluminosilicate nanosheets and nano-sized MFI-type zeolites.

2.2.2 Soft-templating methodology

I synthesized a-ASns in between the hyperswollen lamellar (HL) phases of the heptane solution of Brij L4 (6.91 wt%), methanol (1.00 wt%) and water (1.87 wt%). For the reactants, tetraethyl orthosilicate (TEOS) as the source of silicon (0.37 wt%), aluminum isopropoxide (AIP) as the source of aluminum (0.02 wt%) and sodium hydroxide (NaOH) as a catalyst at various concentrations (c, 0.7×10^{-2} - 2.1×10^{-2} wt%) according to the previously reported procedure, [41] as seen in **Figure. 2.1**.

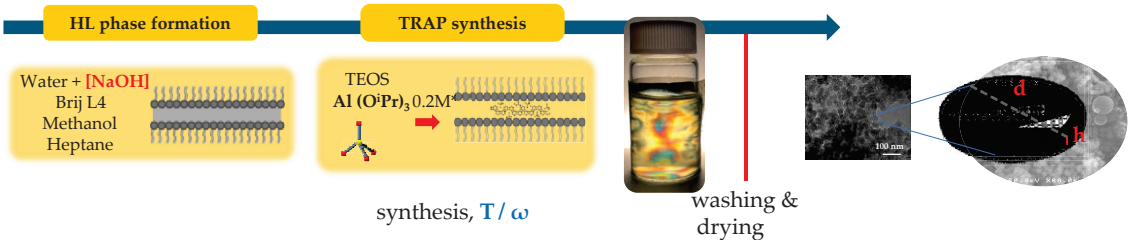

Figure 2.1 a-ASns synthesis using TRAP's.

For the emulsion method, two solutions were prepared: an aqueous solution containing the Si and Al sources and OSDA molecules, and an organic solvent containing the surfactant molecules. The aqueous solution was added to the surfactant/organic solution, and the mixture was stirred to obtain a homogeneous solution. The preparation procedure is described in detail in previous reports [42 – 44].
Micrometer-sized zeolite was synthesized by conventional methods. Three aqueous solutions (Si and Al source, OSDA source and alkaline source) were mixed; pH was adjusted to 10.0 for initial nucleation followed by a second adjustment to a pH of 9.50 for hydrothermal synthesis.

The synthesized zeolites were centrifuged and washed with 2-propanol three times and calcined to eliminate the organic directing agent from the zeolite structure as seen in **Figure 2.2.**

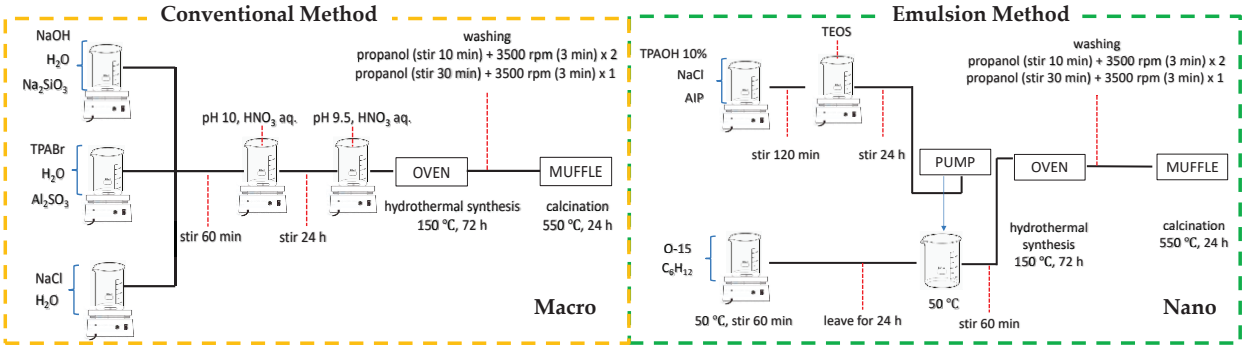

Figure 2.2 Macro and nano sized MFI-type zeolite synthesis methods.

All nanometer and micrometer sized batches were heated at 150 °C in a Teflon-sealed stainless bottles for 72.0 – 84.0 h to improve crystallinity of the sample and obtain smaller Si/Al ratios by increasing the substitution of Si atoms for Al atoms (nanometer samples N.1 – N.3 and micrometer sample M.1). They were calcined at 550 °C for 12.0 hours to remove OSDA molecules and absorb hydrocarbons. Further ion exchange with 10.0% NH_4NO_3 aqueous solution at 80 °C for 9.00 h, centrifuge, and calcination at 550 °C K for 12.0 h was performed to produce the H–form (H–MFI–type) to be used in the kinetic study.

Both micrometer and nanometer MFI- type zeolite were activated by ion exchange for with NH_4NO_3, to obtain the H form zeolite. Ion exchange was performed three times with incrementing amounts of NH_4NO_3 dissolved in Wako water at a temperature of 70 °C. After ion exchange, the zeolite was washed with 2-propanol, centrifuge and calcinated

for 24 hours.

Finally, samples were pelletized. Micrometer size samples were pressed with 1-ton force for 40 minutes while nanometer size samples were pressed with 2-ton force for 20 minutes. This palletization process allowed me to obtain samples with a bulk particle size of ca. 0.40 mm. Before using for catalytic applications, samples were calcinated at 550 °C under a constant flow of air.

2.2.3 Characterization

2.2.3.1 Amorphous Aluminosilicate Nanosheets

Amorphous aluminosilicate nanoparticles were observed by transmission electron microscopy (TEM), obtained using a Hitachi H-800 at 200 kV, as shown in **Figure 2.3a**. All samples were indeed amorphous, based on their X-ray patterns obtained using a PANalytical X'Pert PRO diffractometer with Cu Kα radiation (45 kV and 40 mA) to determine whether the a-ASns were amorphous or crystals. XRD pattern indicated that all the products have no crystallinity, as shown in **Figure 2.3b**. Therefore, synthesized nanoparticles are amorphous.

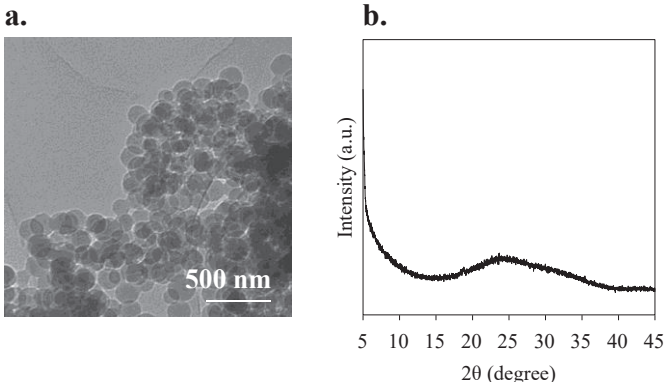

Figure 2.3 Characterization of entry 20 in Table 1 (C_{cat} = 0.0195, T = 30 °C, $\bar{v}$ = 200 rpm). a) TEM image, b) XRD pattern.

At the same time, TEM imaging allowed me to observe a complex morphology, where the overall nanosheet morphology showed that these nanosheets were the result of the lateral aggregation of smaller units, identified as disk-shaped nanoplates with diameters below 100 nm, supporting the evidence that TRAP's successfully avoid vertical aggregation and promotes lateral aggregation only (2D nanomaterials). This conclusion was further confirmed by the particle height of the samples, estimated by atomic force microscopy (AFM) using a Veeco Instruments MMAFM-2, as shown in **Figures 2.4**. AFM images indicate that the average synthesized particles are nanosheets with a thickness of about 3 nm.

Few factors could significantly affect the thickness of the bilayer where the synthesis takes place; 1) the type of surfactant and its interaction with the solvent, 2) the surfactant concentration and 3) presence of salts, [45 – 49]. However, for this study the surfactant used was always Brij L4, with the same concentration and without presence of salts, hence, the thickness of the lipid bilayers where almost constant as seen **in Figures 2.6.c and 2.7.c**, where *h* was almost constant for all points except at low temperatures and high catalyst concentration.

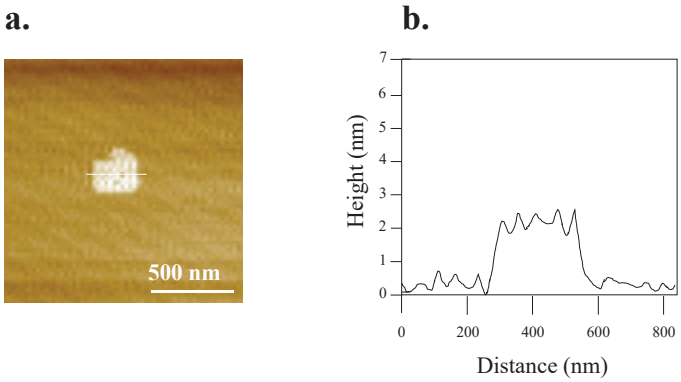

Figure 2.4 Characterization of entry 20 in Table 1 (C_{cat} = 0.0195, T = 30 °C, $\bar{v}$ = 200 rpm). a) AFM image, and b) particle height obtained from AFM analysis.

Fourier-transform infrared (FT-IR) spectroscopy, using a JASCO FT/IR – 4600 with ATR PRO ONE single reflection accessory, was used to estimate the molecular structures of the products, as shown in **Figure 2.5** The FT-IR spectra indicates that silicon and aluminum atoms are bonded to each other via oxygen atoms. This data is consistent with previously reported aluminosilicates.[50] Entry samples 17-25, showed the peak at 1045 cm^{-1} attributed to Si-O-Si bonds (additional FT-IR spectra can be seen in **Figure S.2.1**). The samples synthesized with low C_{cat} showed splitting of the peak at 1045 cm^{-1} into two peaks at 1120 cm^{-1} and 1170 cm^{-1}, corresponding to the Si-O vibrational modes.

The peak at 2350 cm^{-1} suggests that there is strong quasi-symmetrical hydrogen bonding.[6] The spectrum has a small peak attributed to OH stretching around 3700 cm^{-1}. Its intensity was lower than the framework vibration such as Si-O-Si. Consistent with very thin nanosheets. Finally, I identified Al species in all the samples. All Al species are mostly Al_2O_3 that corresponds to the peak at 445 cm^{-1}. However, peaks attributed to some tetrahedral and octahedral units could also be observed at 550 cm^{-1} and 790 cm^{-1}, respectively. The octahedral configuration was preferred as the configuration of the products.

To verify the states of Al species in the amorphous aluminosilicate, I performed the magic angle spinning nucleus magnetic resonance (MAS NMR) spectroscopy for samples 21 and 22. Both the spectra show two peaks as shown in **Figure 2.5.**

The first peak, in the range of 0-10 ppm, corresponds to AlO_6 sites, and the second one in the range of 55-60 ppm corresponds to the AlO_4Na^+ sites.[51] It is consistent with the IR spectrum.

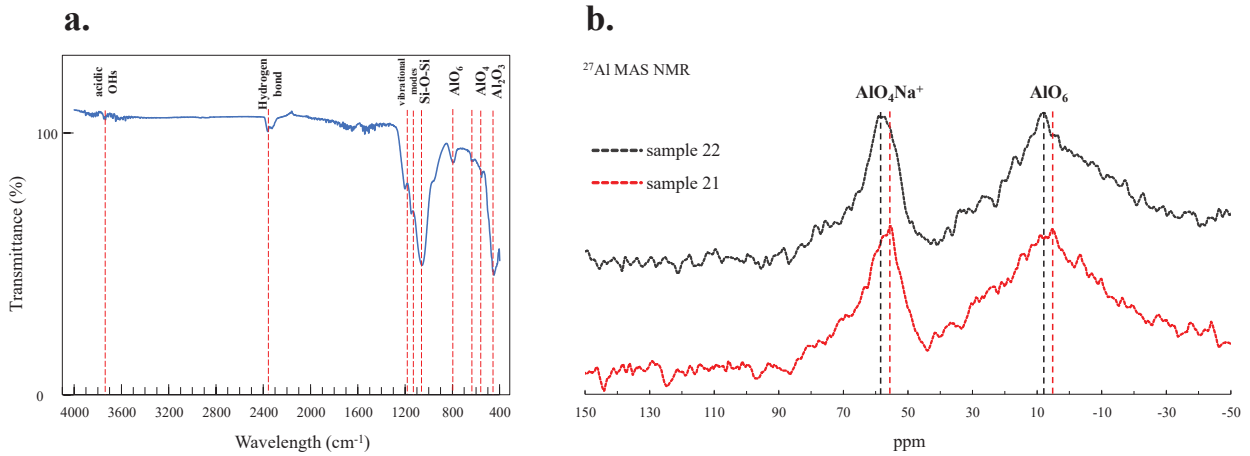

Figure 2.5 a) FT-IR spectra of entry 23 of **Table 2.1**, b) . ^{27}Al MAS NMR spectra of amorphous aluminosilicate nanosheets for entries 21 and 22 of **Table 2.1**.

* b) Scale was increased to show the chemical shift of the identified peaks. (original scale was from -600 to 600, no additional peaks were found)

Using adsorption isotherms, I estimated the external surface areas of the a-ASns by nitrogen (N_2) adsorption on the a-ASns using a BELSORPmax (MicrotracBEL). All adsorption isotherms show an adsorption-desorption curve, as shown in **Figure 2.6a**. They display a type IV isotherm with a flat region in P/P0 = 0 - 0.85, and show a steep increase of the adsorption capacity, attributed to the meso- to macroporous materials with high surface areas.[52,53–55] A hysteresis loop observed here indicates a bottle-neck pore structure.[56] They are consistent with a card-house-like[57] or multiple spheres arrangement generating meso- to macropores between the particles. Therefore, it can also be attributed to some pores between connected a-ASnp in a-ASns, as shown in **Figure 2.6b**. The synthesized a-ASns consisting of a-ASnp is expected to have higher S_{ext} than conventional monolithic AS, and S_{ext} is expected to depend on the size of a-ASnp.

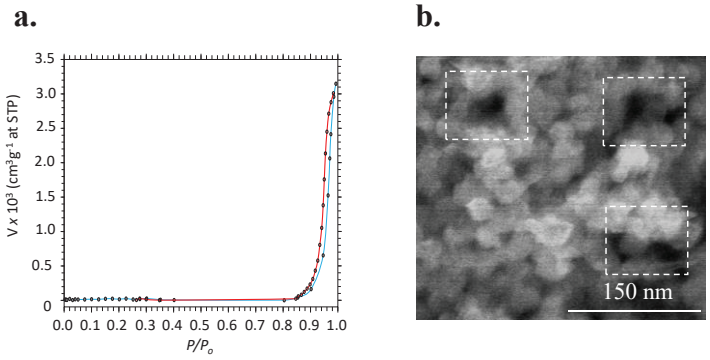

Figure 2.6 Characterization of entry 20 in Table 1 (C_{cat} = 0.0195, T = 30 °C, $\bar{\nu}$ = 200 rpm). N_2 adsorption isotherm. Blue and red lines denote curves upon the absorption and desorption processes, respectively. f) FE-SEM image showing mesoporous structure after lateral and limited vertical aggregation.

2.2.3.2 MFI-type zeolite particles

Zeolite particles morphology as well as crystal size were analyzed by field emission scanning electron microscopy (FE–SEM; JEOL JSM–6500F), scanning electron microscopy (VP–SEM; HITACHI SU1510), and X–ray diffraction (XRD; JEOL JDX–8020), which was also employed to evaluate the crystallinity of the synthesized zeolites. Nitrogen adsorption isotherm was measured using a Belsorp mini (MicrotractBEL Corp.) to determine the total and external surface areas of zeolites, calculated by BET and t–method, respectively. The acidity of the samples was evaluated by the NH_3–TPD method [53], using a BELCAT II (MicrotractBEL Corp.) with BELMASS (MicrotractBEL Corp.). TPD experiment specific conditions are described in detail in previous reports [54].

Acidity of the samples (Si/Al ratios [-]) was calculated using Inductively Coupled Plasma mass spectrometry ICP (ICPE–9000, Shimadzu, Co). Calibrations curves were made using Silicon Standard Solution, 1006 mg L^{-1} (Wako, Japan, product number 197 - 18671) and Aluminium Standard Solution, 1002 mg L^{-1} (Wako, Japan, product number 016 - 15471) for ICP analysis. Samples were prepared by dissolving 10 mg of the samples in 5mL of potassium hydroxide solution 5 M. All solutions were prepared using ultra-pure water.

2.3 Results and Discussion

2.3.1 Amorphous Aluminosilicate (a-AS)

Considering the balance between the high S_{ext} and the reusability of catalysts, nanosheets are promising.[52, 58 – 60] Hyperswollen lamellar (HL) phases, in which sparsely suspended amphiphilic bilayers work as the reactors, are useful for the nanosheet synthesis of various materials: polymers,[61] metal-organic frameworks[51] and metals.[62] The bilayer is called "two-dimensional reactor in amphiphilic phases (TRAP)."[63] This bottom-up TRAP method has allowed us to obtain thin nanosheets with high S_{ext}. The nanosheets with widths of several hundred nm are composed of small nanoplates with widths of several tens of nm. The patchy nanosheets work as the precursors of monolithic zeolite nanosheets.[41]

To create aluminosilicate precursors or supports with high S_{ext}, I focused on the acidity and morphology of amorphous aluminosilicate nanoplates (a-ASnp) constituting the patchy nanosheets (a-ASns) because they determine some of the catalytic properties of the final nanomaterial, as shown in **Figure 2.7**. Each catalytic reaction requires specific a-ASnp with the best combination of chemical composition, structure, morphology, and size, which can be tuned by controlling the conditions of TRAP solutions, such as temperature,[61] composition,[64] and shear rate.[65]

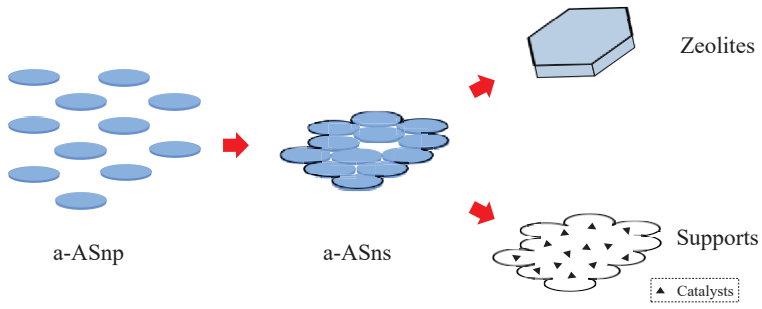

Figure 2.7 Schematic illustration of a-ASnp assembly into a-ASns and further conversion to monolith zeolite nanosheet or catalytic supports.

I was able to tune up the synthesis conditions to obtain 3 nm-thick a-ASns with controlled size. To do this, I look for operation variables using an all-factorials analysis of variance (ANOVA). I also discuss the dependence of the size of a-ASnp on S_{ext}.
I further investigated the application of these a-ASns as support for metal catalysts in the methane decomposition reaction, which I discussed in Chapter 3.

2.3.2 Two-Dimensional Reactor in Amphiphilic Phases (TRAP) for Controlled Synthesis of Amorphous Aluminosilicates nanosheets (a-ASns)

Considering the industrial production and scaling-up, more affordable surfactant Brij L4, which is a mixture of polyethylene glycol dodecyl ethers, was used.[63] I was able to confirm the stability of TRAP solutions to be highly sensitive to composition and temperature, by observing the sample between crossed polarizers;[62] HL phases exhibit colorful textures based on the birefringence. Twenty-four hours after starting the reaction, I washed the product with ethanol three times, centrifuged at 11,000 rpm for 30 min and dried at 90 °C for 12 hours.

To evaluate the significance of the explanatory variables and their effects on the response variables, I did two factorial analyses; one for screening of relevant factors (entries 1-16 in Table 1) and the second one for more detailed analysis of the significant factors on the response variables (entries 17-25 in Table 2.1). The composition of each product was determined by scanning electron microscope-energy dispersive X-ray spectroscopy (SEM-EDX) using a JEOL JCM-7000 microscope at 15 kV. The SEM-EDX spectra showed that all the products have silicon and aluminum and that synthesis conditions influenced the final composition, as shown in **Table 2.1**.

Table 2.1 Experimental results as explanatory and response variables.

Entry	T (°C)	$\bar{v}$ (rpm)	C_{cat}	Si/Al	Yield (%)	$\bar{d}$ (nm)	S_{ext} (m^2/g)
1	10	220	0.14	8.96	11.79	17.69	**94.94**
2	10	220	0.29	5.09	37.52	33.99	**17.21**
3	10	450	0.14	16.54	11.79	16.87	**81.23**
4	10	450	0.29	9.53	35.56	35.60	**75.98**
5	22	220	0.14	16.72	13.95	31.86	**74.52**
6	22	220	0.29	8.52	43.22	34.98	**32.68**
7	22	450	0.14	32.91	13.56	25.24	**81.62**
8	22	450	0.29	15.54	43.61	26.86	**52.30**
9	30	220	0.14	9.26	14.54	51.12	**70.34**
10	30	220	0.29	12.62	49.31	51.26	**53.59**
11	30	450	0.14	18.63	14.93	36.56	**71.40**
12	30	450	0.29	15.96	45.58	39.44	**50.92**
13	40	220	0.14	18.66	16.90	52.69	**63.25**
14	40	220	0.29	29.16	46.37	65.34	**37.59**
15	40	450	0.14	22.70	16.31	51.93	**45.42**
16	40	450	0.29	21.86	49.71	84.18	**38.27**

17	24	220	0.10	19.85	5.70	19.20	**66.13**
18	24	220	0.19	50.71	28.88	34.63	**45.07**
19	24	220	0.29	59.16	46.17	40.93	**31.22**
20	30	220	0.10	21.05	5.30	27.47	**63.07**
21	30	220	0.19	51.53	29.86	36.31	**39.77**
22	30	220	0.29	57.75	50.10	50.65	**23.23**
23	38	220	0.10	24.30	6.29	28.64	**53.11**
24	38	220	0.19	51.59	34.58	41.07	**43.65**
25	**38**	**220**	**0.29**	**57.39**	**52.06**	**60.79**	**24.97**

* Temperature (T), rotational frequency ($\bar{v}$), relative catalyst concentration (C_{cat} = [OH^-]/[Si]), silica to aluminum ratio (Si/Al), average particle diameter ($\bar{d}$) and specific external surface area (S_{ext})

2.3.2.1 Factorial Analysis of Variance

TRAP method enables a controlled synthesis of the desired material, allowing control of morphology and size. Using this method, S_{ext}, which is important factor in the synthesis of aluminosilicate, was used as the response variable.

Therefore, I performed a first exploratory factorial analysis of variance (ANOVA) for all three factors based on S_{ext}. The first ANOVA using entries 1-16 in **Table 2.1** showed the importance of the analyzed factors: temperature (T), agitation rate ($\bar{v}$), and relative catalyst concentration (C_{cat} = [OH-]/[Si]). The full model statistical p-value was 1.49×10^{-3}. The main factor was C_{cat}, with a p-value of 1.83×10^{-3}.

The other factors did not significantly affect the S_{ext} for a-ASnp: T and $\bar{v}$ p-values were 5.47×10^{-2} and 8.04×10^{-2}, respectively. These results indicate we should mainly control C_{cat} to control a-ASns size and composition.

To verify that C_{cat} was the main variable for the control synthesis of a-ASns, I performed a second factor analysis varying only C_{cat} at several T, the second stronger factor. The second ANOVA used entries 17-25 in **Table 2.1**. The full model statistical p-value was 6.87×10^{-5}. Naturally, C_{cat} showed a low p-value of 2.43×10^{-5} to control the desired response variables: S_{ext}, silica-to-aluminum ratio (Si/Al), particle diameter and height ($\bar{d}$ and $\bar{h}$, respectively). For detailed analytical purposes, I focused on this factorial only.

The correlation analysis showed a negative correlation between S_{ext} and $\bar{d}$ or Si/Al with correlation coefficient of –0.92 for both cases, as shown in **Table 2.2**. As $\bar{d}$ or Si/Al increases, S_{ext} decreases. Inversely, there is a positive correlation between Si/Al and factors $\bar{d}$ or $\bar{h}$ with a correlation coefficient of 0.82 and 0.57, respectively. In summary S_{ext} negatively correlates to the following variables in correlation strength; $\bar{d}$ > Si/Al > $\bar{h}$.

Table. 2.2 Correlation coefficients for different analyzed response variables in the second factorial (entries 17-25 in Table 2.1)

	S_{ext}	Si/Al	$\bar{d}$	$\bar{h}$
S_{ext}	1			
Si/Al	-0.92	1		
$\bar{d}$	-0.92	0.82	1	
$\bar{h}$	**-0.53**	**0.57**	**0.31**	1

Visually examination showed that the dependence of the physicochemical properties of a-ASnp on C_{cat} and T, as shown in **Figures 2.8**. The slopes of S_{ext} and Si/Al with respect to T are almost zero for $C_{cat,1}$ (0.10), $C_{cat,2}$ (0.19) and $C_{cat,3}$ (0.29), as shown in **Figures 2.8a and 2.8b**. Meanwhile, the slope of $\bar{h}$ with respect to T depends on C_{cat}, as shown in **Figure 2.8c.** As C_{cat} decreases, $\bar{h}$ is independent of T. The slope of $\bar{d}$ with respect to T slightly depends on C_{cat}, as shown in **Figure 2.8d**. Higher T tends to increase a-ASnp width. These results indicate that T had a small effect on the response variables.

Moreover, they suggest that C_{cat} affects physicochemical properties more strongly. It is consistent with ANOVA.

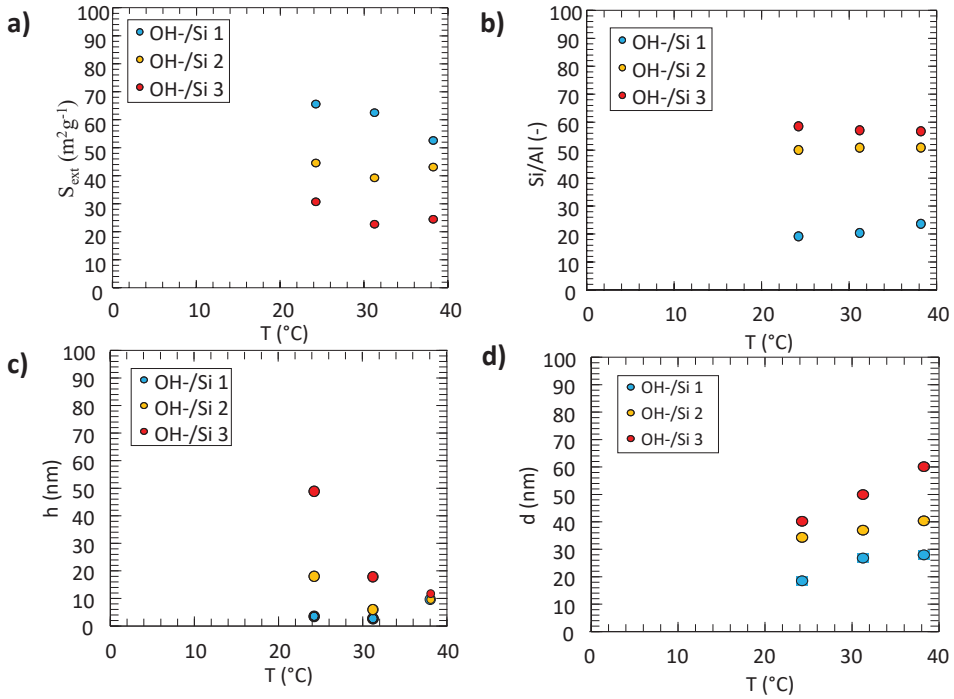

Figure 2.8 Temperature effect on the main physicochemical properties of the synthesized a-ASnp a) S_{ext} as a function of C_{cat}, b) Si/Al as a function of C_{cat}, c) $\bar{h}$ as a function of C_{cat}, d) $\bar{d}$ as a function of C_{cat}.

Finally, I validated C_{cat} as the operation variable for the physicochemical properties of a-ASnp, as shown in **Figure 2.9**. The slopes of S_{ext} and Si/Al with respect to C_{cat} are almost the same for T_1 (24°C), T_2 (30 °C) and T_3 (38°C), as shown in **Figures 2.9a and 2.9b**. As the response variable, S_{ext} negatively correlates with C_{cat}. As the reaction rate increases, S_{ext} decreases. Si/Al also showed a positive correlation with C_{cat}. Higher reaction rate is likely to stabilize the Al species in the framework better. Moreover, the S_{ext} and Si/Al are almost independent of T. It is consistent with **Figures 2.8a and 2.8b**. Meanwhile, the slope of $\bar{h}$ with respect to C_{cat} depends on T, as shown in **Figure 2.9c**. For higher T, $\bar{h}$ is larger and independent of C_{cat}. It suggests that reaction rate is too high so that TRAP cannot confine the particles. Furthermore, even when T is lower, $\bar{h}$ becomes larger in the TRAP solution with much higher C_{cat} that induces higher reaction rate. Destabilizing the TRAPs should cause the high $\bar{h}$. This means that stabilizing TRAP needs appropriate temperatures.[61]

As theoretically expected, $\bar{h}$ negatively correlates with S_{ext}. This means that slower particle growth increases the particle aspect ratio. The slope of $\bar{d}$ with respect to C_{cat} is positive and almost independent of T, as shown in **Figure 2.9d** and consistent with the discussion about the TRAP stability. From the results I was able to hypothesize that C_{cat} works as the operation variable for $\bar{d}$ and Si/Al. If we achieve higher stability TRAP's solutions by adding cosurfactant, S_{ext} becomes positive correlated with $\bar{d}$. [64]

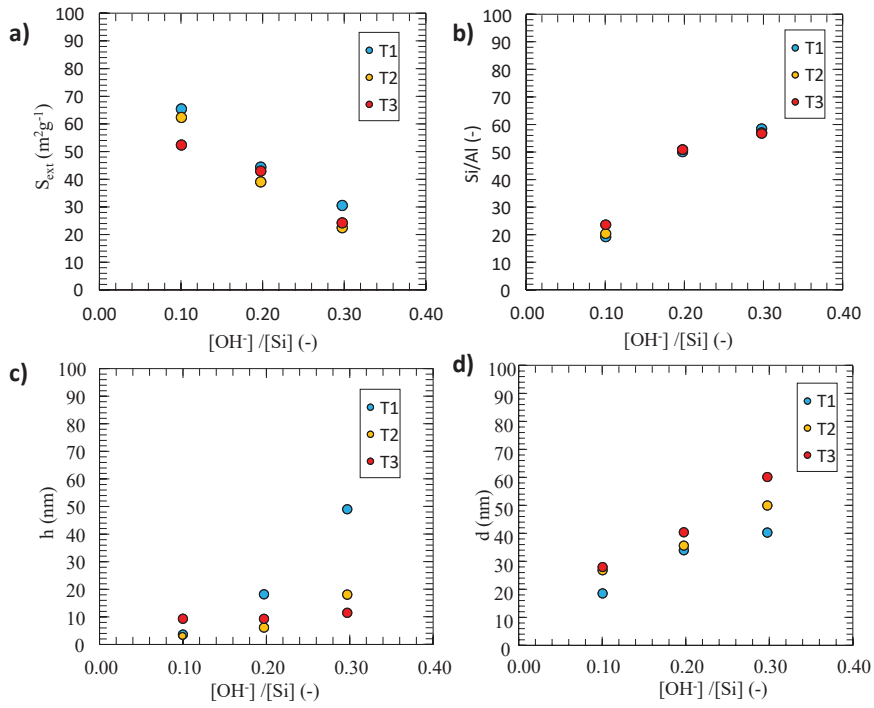

Figure. 2.9 Concentration effect on the main physicochemical properties of the synthesized a-ASnp a) S_{ext} as a function of T, b) Si/Al as a function of T, c) $\bar{h}$ as a function of T, d) $\bar{d}$ as a function of T.

The Si/Al ratio and S_{ext} of amorphous aluminosilicate nanoplates can be controlled as the response variables by tuning C_{cat} in TRAP's as the operation variable, was confirmed. I expect that $\bar{d}$ simultaneously becomes the response variable if TRAP solution can be more stable.

2.3.3 H-MFI-type Zeolites

Narrow size distribution H-MFI-type zeolites with different crystals size and Si/Al ratios [-] were prepared by conventional and emulsion method, via hydrothermal synthesis.

All zeolites were successfully synthesized; nonetheless, synthesized zeolites M.2 and N.3 had less crystallinity compared to the other batches (M.1, N.1 and N.2). The main reason was due to the hydrothermal synthesis time. M.1, N.1, and N.2 had 84 hours of hydrothermal synthesis, while M.2 and N.3 had 72.

Successful synthesis of MFI type zeolite was confirmed by XRD analysis (**Figure 2.10 a**)), when compared to the calculated powder diffraction pattern for MFI-type zeolite from the database of zeolite structure (International Zeolite Association), as well as good crystallinity of the samples. Approximate crystal size was determined by imaging of the samples using SEM and FE–SEM as seen in **Figure 2.10 b**), ranging from 100 – 2.00 x 10^3 nm.

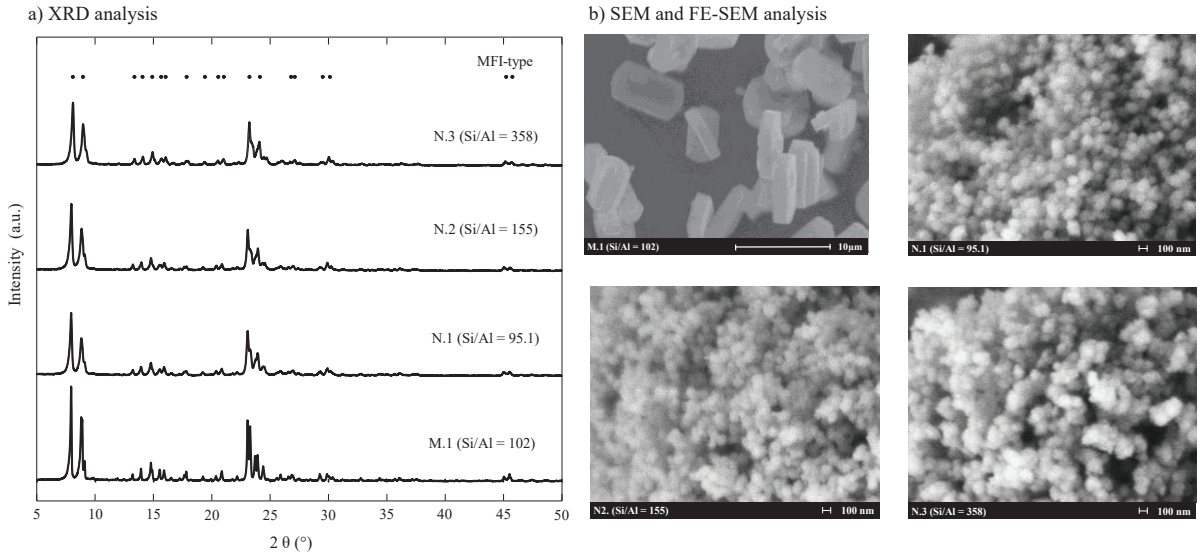

Figure. 2.10 a) X–ray powder diffraction patterns of synthesized samples, b) Morphologies of samples

BET surface areas (S_{BET}) and micropore volumes (V_m) of the nanometer- and micrometer-sized MFI type zeolites did not present any correlation with crystal size, ranging from 0.150 – 0.168 cm^3g^{-1} for V_m and 358 – 425 m^2g^{-1} for S_{BET}. As in previous reports [66], only external area (S_{ext}) showed a clear difference between the micrometer– and nanometer–sized MFI type zeolites, where nanometer-sized crystals showed much larger S_{ext}, ranging from 26.2 – 50.7 m^2g^{-1}.

For the micrometer (M.1) and nanometer (N.1) samples, used in the calculation of the kinetics of the transalkylation of ppp and benzene, the amount of NH_3 desorbed at high temperatures (strong acid site) was 0.162 and 0.174 $mmolg^{-1}$, respectively. Si/Al ratio [-] difference between the samples (6.80 %) was considered small enough to discuss effect of crystal size on the reaction rate. The Si/Al (associated to the strong acid site) ratios [-] used in the study range from 95 – 358 [–], evaluated by the NH_3–TPD method.

Table 2.3. MFI type zeolites properties used in this study

Sample	Si/Al [a] ratio (–)	V_m (cm^3g^{-1})	S_{BET} (m^2g^{-1})	S_{EXT} (m^2g^{-1})	Crystallite size [d] (nm)	Particle size [e] (nm)
M.1	102	0.168	384	10.4	345.3	2.00×10^3
N.1	95.1	0.165	425	50.7	26.7	160
N.2	155	0.150	397	49.1	24.4	113
N.3	358	0.151	358	26.2	22.4	100

[a] Si/Al ratio was calculated by the NH_3–TPD method.

[b] Micropore volume (V_m) and external surface area (S_{ext}) were obtained by t–method from nitrogen adsorption.

[c] Surface area (S_{BET}) was obtained by BET–method from nitrogen adsorption.

[d] Crystallite size was calculated from XRD pattern using Scherrer equation and Origin software (Multiple peak fit) for each sample diffraction. Main diffractions peaks were 011, 020, 421, 431, 250 and 053.

[e] Particle size was estimated from FE–SEM and SEM images

2.4 Conclusions

I successfully synthesized aluminosilicate nanomaterials with controlled size and morphology. By using lyotropic mixtures of Water/Surfactant/Organic Solvent, it was possible to obtained different morphologies, plates, sheets and spheres of aluminosilicate materials, both amorphous and crystalline. Furthermore, in our laboratory, I successfully used these amorphous aluminosilicate nanosheets (a-ASns) as precursors for several zeolite nanosheets; hence, the control of this a-ASns was significant. In both synthetic methodologies (TRAP and Emulsion), controlling the concentration of reactants had a great impact on the amount of aluminum in the aluminosilicate framework and S_{ext}.

I determined that the concentration of alkaline catalyst for the hydrolysis of silica and aluminum reagents was the most significant variable for the control of particle size and amount of Lewis acid sites. The nanometer size particles showed improved surface area compared to their bulk non-porous counterparts. Finally, the concentration of the components in the lyotropic mixture and the type of surfactant have a great influence on the several available mesophases for that specific mixture. In my study I focus mainly on sheets (lamellar region), and spheres (micelle region).

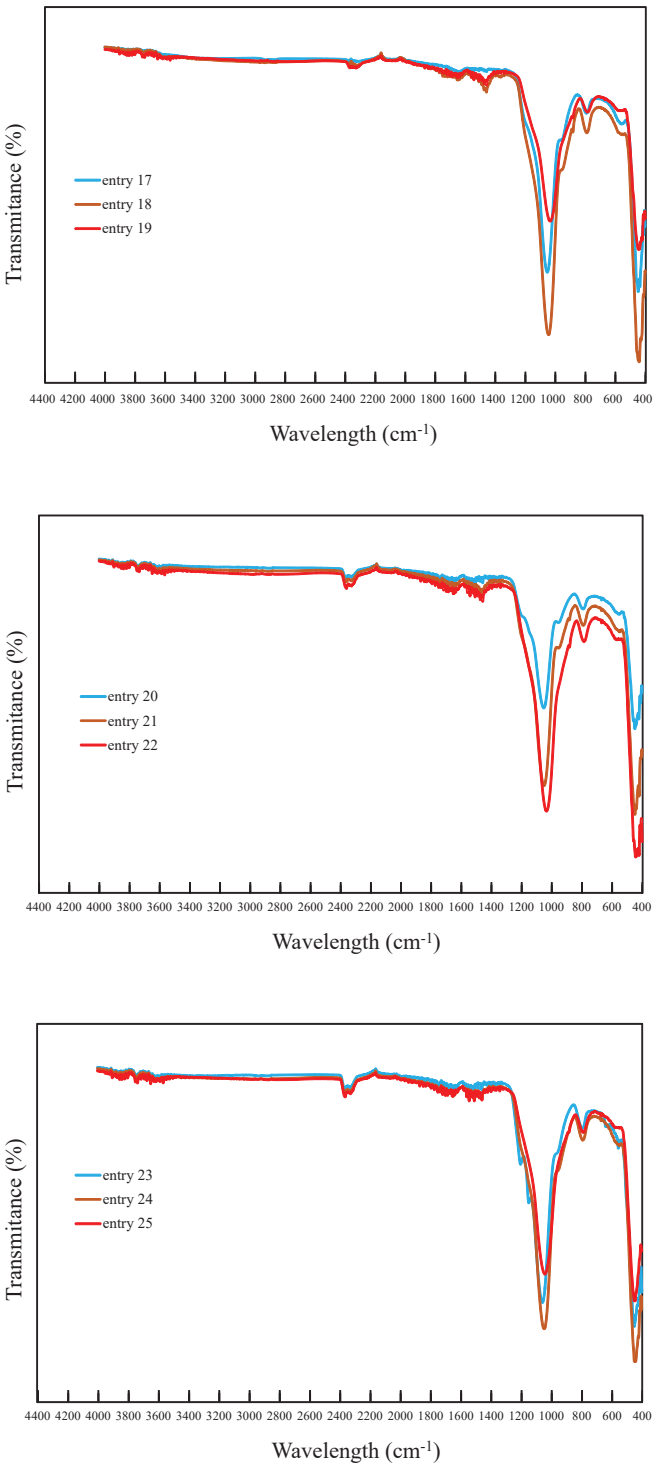

Figure S.2.1 a) FT-IR spectra of entries 17 - 25

Reference

[1] M. Msheik, S. Rodat, S. Abanades, 32. Methane Cracking for Hydrogen Production: A Review of Catalytic and Molten Media Pyrolysis energies Methane Cracking for Hydrogen Production: A Review of Catalytic and Molten Media Pyrolysis, (2021). https://doi.org/10.3390/en14113107ï.

[2] P. Del Gallo, R. Meunier, C. Pham-Huu, C. Crouzet, M.J. Ledoux, 33. Selective n-Butane Isomerization over High Specific Surface Area MoO 3-Carbon-Modified Catalyst, 1997. https://pubs.acs.org/sharingguidelines.

[3] L. Li, S. Wang, Z. Zhu, 24. Geopolymeric adsorbents from fly ash for dye removal from aqueous solution, J Colloid Interface Sci 300 (2006) 52–59. https://doi.org/10.1016/j.jcis.2006.03.062.

[4] L. V.D. Gammond, R.E. Youngman, A. Zeidler, B.G. Aitken, P.S. Salmon, 25. Structural model for amorphous aluminosilicates, Journal of Chemical Physics 156 (2022). https://doi.org/10.1063/5.0079607.

[5] B.R. Goldsmith, B. Peters, J.K. Johnson, B.C. Gates, S.L. Scott, 26. Beyond Ordered Materials: Understanding Catalytic Sites on Amorphous Solids, ACS Catal 7 (2017) 7543–7557. https://doi.org/10.1021/acscatal.7b01767.

[6] M. Trombetta, G. Busca, S. Rossini, V. Piccoli, U. Cornaro, A. Guercio, R. Catani, R.J. Willey, 27. FT-IR Studies on Light Olefin Skeletal Isomerization Catalysis III. Surface Acidity and Activity of Amorphous and Crystalline Catalysts Belonging to the SiO 2-Al 2 O 3 System, 1998.

[7] A. Fernández-Jiménez, R. Vallepu, T. Terai, A. Palomo, K. Ikeda, 28. Synthesis and thermal behavior of different aluminosilicate gels, J Non Cryst Solids 352 (2006) 2061–2066. https://doi.org/10.1016/j.jnoncrysol.2006.03.037.

[8] H. Hartati, A. Purwaningsih, T.S. Tjahjandarie, N.H. Saputri, I.S. Puspitasari, C.N. Lamanele, A.A. Sa'adah, A.S. Haque, D.Z. Mardho, 29. Synthesis of amorphous aluminosilicate from impure Indonesian kaolin, Open Chem 18 (2020) 295–302. https://doi.org/10.1515/chem-2020-0033.

[9] P. Reif, N.K. Gupta, M. Rose, 30. Highly stable amorphous silica-alumina catalysts for continuous bio-derived mesitylene production under solvent-free conditions, Green Chemistry 25 (2023) 1588–1596. https://doi.org/10.1039/d2gc04116b.

[10] C. Kosanović, S. Bosnar, B. Subotić, V. Svetličić, T. Mišić, G. Dražić, K. Havancsák, 31. Study of the microstructure of amorphous aluminosilicate gel before and after its hydrothermal treatment, Microporous and Mesoporous Materials 110 (2008) 177–185. https://doi.org/10.1016/j.micromeso.2007.06.007.

[11] T. Ennaert, J. Van Aelst, J. Dijkmans, R. De Clercq, W. Schutyser, M. Dusselier, D. Verboekend, B.F. Sels, Potential and challenges of zeolite chemistry in the catalytic conversion of biomass, Chem Soc Rev 45 (2016) 584–611. https://doi.org/10.1039/C5CS00859J.

[12] P.Y. Dapsens, C. Mondelli, J. Pérez-Ramírez, Design of Lewis-acid centres in zeolitic matrices for the conversion of renewables, Chem Soc Rev 44 (2015) 7025–7043. https://doi.org/10.1039/C5CS00028A.

[13] N. Katada, M. Niwa, Analysis of Acidic Properties of Zeolitic and Non-Zeolitic Solid Acid Catalysts Using Temperature-Programmed Desorption of Ammonia, Catalysis Surveys from Asia 8 (2004) 161–170. https://doi.org/10.1023/B:CATS.0000038534.37849.16.

[14] A. Corma, M. Davis, V. Fornés, V. González-Alfaro, R. Lobo, A.V. Orchillés, Cracking Behavior of Zeolites with Connected 12- and 10-Member Ring Channels: The Influence of Pore Structure on Product Distribution, J Catal 167 (1997) 438–446. https://doi.org/10.1006/jcat.1997.1584.

[15] P. MAGNOUX, Coking, aging, and regeneration of zeolites III. Comparison of the deactivation modes of H-mordenite, HZSM-5, and HY during n-Heptane cracking, J Catal

106 (1987) 242–250. https://doi.org/10.1016/0021-9517(87)90228-4.
[16] D. Verboekend, Y. Liao, W. Schutyser, B.F. Sels, Alkylphenols to phenol and olefins by zeolite catalysis: a pathway to valorize raw and fossilized lignocellulose, Green Chem. 18 (2016) 297–306. https://doi.org/10.1039/C5GC01868D.
[17] Y. Xie, Y. Liang, Q. Zhou, J. Wang, Q. Gong, W. Jia, J. Li, Z. Zhu, Transalkylation of C $_{10}$ Aromatics with 2-Methylnaphthalene for 2,6-Dimethylnaphthalene Synthesis over a Shape-Selective SiO $_{2}$ –Ni–H-Mordenite with Nanosheet Crystal, Ind Eng Chem Res 60 (2021) 17907–17916. https://doi.org/10.1021/acs.iecr.1c03652.
[18] J.A.H. Gaitan, Y. Nakasaka, T. Yoshikawa, N. Nishiyama, T. Masuda, Catalytic transalkylation of alkylphenol to phenol in supercritical benzene fluid over MFI type zeolite in a fixed-bed reactor: Diffusion and reaction limitations, Chemical Engineering Journal 464 (2023) 142618. https://doi.org/10.1016/j.cej.2023.142618.
[19] S. Inagaki, K. Kamino, E. Kikuchi, M. Matsukata, Shape selectivity of MWW-type aluminosilicate zeolites in the alkylation of toluene with methanol, Appl Catal A Gen 318 (2007) 22–27. https://doi.org/10.1016/j.apcata.2006.10.036.
[20] H. Konno, T. Okamura, Y. Nakasaka, T. Tago, T. Masuda, Effects of Crystal Size and Si/Al Ratio of MFI-type Zeolite Catalyst on <i>n</i>-Hexane Cracking for Light Olefin Synthesis, Journal of the Japan Petroleum Institute 55 (2012) 267–274. https://doi.org/10.1627/jpi.55.267.
[21] T. Tago, H. Konno, M. Sakamoto, Y. Nakasaka, T. Masuda, Selective synthesis for light olefins from acetone over ZSM-5 zeolites with nano- and macro-crystal sizes, Appl Catal A Gen 403 (2011) 183–191. https://doi.org/10.1016/j.apcata.2011.06.029.
[22] T. Masuda, Diffusion Mechanisms of Zeolite Catalysts, Catalysis Surveys from Asia 7 (2003) 133–144. https://doi.org/10.1023/A:1025333507890.
[23] F. Jin, Y. Cui, Z. Rui, Y. Li, Effect of sequential desilication and dealumination on catalytic performance of ZSM-5 catalyst for pyridine and 3-picoline synthesis, J Mater Res 25 (2010) 272–282. https://doi.org/10.1557/JMR.2010.0033.
[24] M. Ogura, S. Shinomiya, J. Tateno, Y. Nara, E. Kikuchi, M. Matsukata, Formation of Uniform Mesopores in ZSM-5 Zeolite through Treatment in Alkaline Solution, Chem Lett 29 (2000) 882–883. https://doi.org/10.1246/cl.2000.882.
[25] J.C. Groen, J.C. Jansen, J.A. Moulijn, J. Pérez-Ramírez, Optimal Aluminum-Assisted Mesoporosity Development in MFI Zeolites by Desilication, J Phys Chem B 108 (2004) 13062–13065. https://doi.org/10.1021/jp047194f.
[26] J. Groen, On the introduction of intracrystalline mesoporosity in zeolites upon desilication in alkaline medium, Microporous and Mesoporous Materials 69 (2004) 29–34. https://doi.org/10.1016/j.micromeso.2004.01.002.
[27] L. Xu, Z. Liu, Z. Li, J. Liu, Y. Ma, J. Guan, Q. Kan, Non-crystalline mesoporous aluminosilicates catalysts: Synthesis, characterization and catalytic applications, J Non Cryst Solids 357 (2011) 1335–1341. https://doi.org/10.1016/j.jnoncrysol.2010.12.028.
[28] T. Sumi, S. Kokuryo, Y. Fujimoto, X. Li, K. Miyake, Y. Uchida, N. Nishiyama, Mg and Zn co-doped mesoporous ZSM-5 as an ideal catalyst for ethane dehydroaromatization reaction, Catal Sci Technol 12 (2022) 7010–7017. https://doi.org/10.1039/D2CY01129H.
[29] X. Li, J.A. Hernandez Gaitan, S. Kokuryo, T. Sumi, H. Kitamura, K. Miyake, Y. Uchida, N. Nishiyama, Hierarchical zeolites with high hydrothermal stability prepared via desilication of OSDA-occluded zeolites, Microporous and Mesoporous Materials 344 (2022) 112096. https://doi.org/10.1016/j.micromeso.2022.112096.
[30] P. Morales-Pacheco, F. Alvarez-Ramirez, P. Del Angel, L. Bucio, J.M. Domínguez, Synthesis and Structural Properties of Zeolytic Nanocrystals I. MFI Type Zeolites, The Journal of Physical Chemistry C 111 (2007) 2368–2378. https://doi.org/10.1021/jp064780v.
[31] S. Mintova, V. Valtchev, T. Onfroy, C. Marichal, H. Knözinger, T. Bein, Variation of the Si/Al ratio in nanosized zeolite Beta crystals, Microporous and Mesoporous Materials 90 (2006) 237–245. https://doi.org/10.1016/j.micromeso.2005.11.026.
[32] R.C. Lima, C.W. Lopes, J. Villarroel-Rocha, L. Bieseki, K. Sapag, S.B.C. Pergher, Organic-

Free Synthesis of Finned Mordenite Zeolite, Nanomaterials 12 (2022) 2623. https://doi.org/10.3390/nano12152623.
[33] B.A. Holmberg, H. Wang, J.M. Norbeck, Y. Yan, Controlling size and yield of zeolite Y nanocrystals using tetramethylammonium bromide, Microporous and Mesoporous Materials 59 (2003) 13–28. https://doi.org/10.1016/S1387-1811(03)00271-3.
[34] J. Padilla, V. García, Preparation and Characterization of ZSM-5 Zeolites Modified with Titanium and Iron by Direct Synthesis, MRS Proceedings 1765 (2015) 145–151. https://doi.org/10.1557/opl.2015.821.
[35] S. Mintova, N.H. Olson, V. Valtchev, T. Bein, Mechanism of Zeolite A Nanocrystal Growth from Colloids at Room Temperature, Science (1979) 283 (1999) 958–960. https://doi.org/10.1126/science.283.5404.958.
[36] M.J. Mora-Fonz, C.R.A. Catlow, D.W. Lewis, The role of solvation and pH in the nucleation of pure silica zeolites, in: 2005: pp. 295–302. https://doi.org/10.1016/S0167-2991(05)80352-0.
[37] C.S. Tsay, A.S.T. Chiang, The synthesis of colloidal zeolite TPA–silicalite-1, Microporous and Mesoporous Materials 26 (1998) 89–99. https://doi.org/10.1016/S1387-1811(98)00219-4.
[38] S. Mintova, Crystal growth of nanosized zeolites in solutions and films: In situ grazing incidence diffraction (GID) study using synchrotron X-ray radiation, J Mater Sci Lett 22 (2003) 751–753. https://doi.org/10.1023/A:1023760111702.
[39] S.C. Larsen, Nanocrystalline Zeolites and Zeolite Structures: Synthesis, Characterization, and Applications, The Journal of Physical Chemistry C 111 (2007) 18464–18474. https://doi.org/10.1021/jp074980m.
[40] V. Valtchev, S. Mintova, Nano-Microporous Materials: Hydrothermal Synthesis of Zeolites, in: Encyclopedia of Inorganic and Bioinorganic Chemistry, Wiley, 2011. https://doi.org/10.1002/9781119951438.eibc0334.
[41] K. Sasaki, J.A.H. Gaitan, T. Okue, S. Matoba, Y. Tokuda, K. Miyake, Y. Uchida, N. Nishiyama, 1. Amorphous Aluminosilicate Nanosheets as Universal Precursors for the Synthesis of Diverse Zeolite Nanosheets for Polymer-Cracking Reactions, Angewandte Chemie - International Edition 61 (2022). https://doi.org/10.1002/anie.202213773.
[42] H. Kondoh, Y. Nakasaka, T. Kitaguchi, T. Yoshikawa, T. Tago, T. Masuda, Upgrading ofoil sand bitumen over an iron oxide catalyst using sub- and super-critical water, Fuel Processing Technology 145 (2016) 96–101. https://doi.org/10.1016/j.fuproc.2016.01.030.
[43] T. Tago, M. Nishi, Y. Kouno, T. Masuda, New method for preparing monodispersed nanocrystalline silicalite via hydrothermal synthesis in water/surfactant/oil solution, Chem Lett 33 (2004) 1040–1041. https://doi.org/10.1246/cl.2004.1040.
[44] T. Tago, D. Aoki, K. Iwakai, T. Masuda, Preparation for size-controlled MOR zeolite nanocrystal using water/surfactant/organic solvent, Top Catal 52 (2009) 865–871. https://doi.org/10.1007/s11244-009-9227-z.
[45] Kosior, D., Gvaramia, M., Scarratt, L. R. J., Maroni, P., Trefalt, G., & Borkovec, M. (2021). Thickness of the particle-free layer near charged interfaces in suspensions of like-charged nanoparticles. Soft Matter, 17(25), 6212–6224. https://doi.org/10.1039/D1SM00584G
[46] Kučerka, N., Heberle, F., Pan, J., & Katsaras, J. (2015). Structural Significance of Lipid Diversity as Studied by Small Angle Neutron and X-ray Scattering. Membranes, 5(3), 454–472. https://doi.org/10.3390/membranes5030454
[47] Nouhi, S., Koutsioubas, A., Kapaklis, V., & Rennie, A. R. (2020). Distortion of surfactant lamellar phases induced by surface roughness. The European Physical Journal Special Topics, 229(17–18), 2807–2823. https://doi.org/10.1140/epjst/e2020-900220-3
[48] Pabst, G., Hodzic, A., Štrancar, J., Danner, S., Rappolt, M., & Laggner, P. (2007). Rigidification of Neutral Lipid Bilayers in the Presence of Salts. Biophysical Journal, 93(8), 2688–2696. https://doi.org/10.1529/biophysj.107.112615
[49] Speer, D. J., Salvador-Castell, M., Huang, Y., Liu, G.-Y., Sinha, S. K., & Parikh, A. N. (2023). Surfactant-Mediated Structural Modulations to Planar, Amphiphilic Multilamellar Stacks. The Journal of Physical Chemistry B, 127(34), 7497–7508. https://doi.org/10.1021/acs.jpcb.3c01654

[50] P.P. Nampi, P. Moothetty, F.J. Berry, M. Mortimer, K.G. Warrier, Aluminosilicates with varying alumina-silica ratios: Synthesis via a hybrid sol-gel route and structural characterisation, Dalton Transactions 39 (2010) 5101–5107. https://doi.org/10.1039/c001219j.
[51] L. Mafra, J.A. Vidal-Moya, T. Blasco, Structural Characterization of Zeolites by Advanced Solid State NMR Spectroscopic Methods, in: 2012: pp. 259–351. https://doi.org/10.1016/B978-0-12-397020-6.00004-0.
[52] J.H. Zhao, R.Q. Tan, Y. Yang, W. Xu, J. Li, W.F. Shen, G.Q. Wu, Y.L. Zhu, X.F. Yang, W.J. Song, Synthesis mechanism of nanoporous Sn3O4 nanosheets by hydrothermal process without any additives, Chinese Physics B 24 (2015). https://doi.org/10.1088/1674-1056/24/6/066202.
[53] M. V. Santhosh, R. Geethu, K.S. Devaky, A novel, facile, and efficient two-step hydrothermal route for WS2 nanosheets and its optimistic exposure as competent industrial-level sonocatalyst, Journal of Materials Science: Materials in Electronics 32 (2021) 9357–9367. https://doi.org/10.1007/s10854-021-05599-x.
[54] X. Li, W. Ge, P. Wang, H. Zhao, Y. Tian, X. He, Z. Liu, SnO2 Nanosheets for NIR-Enhanced NO2 Sensing and Adsorption/Desorption, ACS Appl Nano Mater 6 (2023) 6415–6422. https://doi.org/10.1021/acsanm.3c01059.
[55] J. Li, Z. Jin, Y. Chao, A. Wang, D. Wang, S. Chen, Q. Qian, Synthesis of Graphene-Oxide-Decorated Porous ZnO Nanosheet Composites and Their Gas Sensing Properties, Chemosensors 11 (2023). https://doi.org/10.3390/chemosensors11010065.
[56] R. Wang, S. Sang, D. Zhu, S. Liu, K. Yu, Pore characteristics and controlling factors of the Lower Cambrian Hetang Formation shale in Northeast Jiangxi, China, Energy Exploration and Exploitation 36 (2018) 43–65. https://doi.org/10.1177/0144598717723814.
[57] S. Ida, A.K. Thapa, Y. Hidaka, Y. Okamoto, M. Matsuka, H. Hagiwara, T. Ishihara, Manganese oxide with a card-house-like structure reassembled from nanosheets for rechargeable Li-air battery, J Power Sources 203 (2012) 159–164. https://doi.org/10.1016/j.jpowsour.2011.11.042.
[58] H.N. Abdelhamid, An introductory review on advanced multifunctional materials, Heliyon 9 (2023) e18060. https://doi.org/10.1016/j.heliyon.2023.e18060.
[59] K. Nakagawa, Metal oxide nanosheets synthesized by bottom-up approach: Applications to catalyst and separation membranes, Journal of the Japan Petroleum Institute 62 (2019) 53–60. https://doi.org/10.1627/jpi.62.53.
[60] K. Na, M. Chol, W. Park, Y. Sakamoto, O. Terasakl, R. Ryoo, Pillared MFI zeolite nanosheets of a single-unit-cell thickness, J Am Chem Soc 132 (2010) 4169–4177. https://doi.org/10.1021/ja908382n.
[61] Y. Uchida, T. Nishizawa, T. Omiya, Y. Hirota, N. Nishiyama, Nanosheet Formation in Hyperswollen Lyotropic Lamellar Phases, J Am Chem Soc 138 (2016) 1103–1105. https://doi.org/10.1021/jacs.5b11256.
[62] K. Sasaki, T. Okue, T. Nakai, Y. Uchida, N. Nishiyama, Lateral Growth of Uniformly Thin Gold Nanosheets Facilitated by Two-Dimensional Precursor Supply, Langmuir 37 (2021) 5872–5877. https://doi.org/10.1021/acs.langmuir.1c00344.
[63] K. Sasaki, T. Okue, Y. Shu, K. Miyake, Y. Uchida, N. Nishiyama, Thin ZIF-8 nanosheets synthesized in hydrophilic TRAPs, Dalton Transactions 50 (2021) 10394–10399. https://doi.org/10.1039/d1dt01507a.
[64] K. Sasaki, J.A. Hernandez Gaitan, Y. Tokuda, K. Miyake, Y. Uchida, N. Nishiyama, A nanosheet molding method to estimate the size of bilayers suspended in liquids, J Mater Chem C Mater 10 (2022) 15816–15821. https://doi.org/10.1039/D2TC03765C.
[65] K. Sasaki, K. Miyake, Y. Uchida, N. Nishiyama, Mechanochemical Synthesis of Dispersible Platinum Nanosheets for Enhanced Catalysis in a Microreactor, ACS Appl Nano Mater 5 (2022) 4998–5005. https://doi.org/10.1021/acsanm.1c04583.
[66] T. Tago, Y. Okubo, S.R. Mukai, T. Tanaka, T. Masuda, Simultaneous characterization of acidic and basic properties of solid catalysts by a new TPD method and their correlation to reaction rates, Appl Catal A Gen 290 (2005) 54–64. https://doi.org/10.1016/j.apcata.2005.05.010.

Chapter 3

Nanosized particle's Role in the Design of Novel Catalysts for the Catalytic Decomposition of Methane (CDM)

3.1 Introduction

In this chapter, I focus on the catalytic applications of amorphous aluminosilicate materials as support for metal species.

Fossil fuels are one of the main sources of greenhouse gas emissions and, currently, a primary source of energy in developing countries.[1] Alternative solutions, such as hydrogen energy systems, could become viable through intense research in production, storage and usage. Energy production using hydrogen technologies is starting to become viable, and the technological gaps are starting to close,[2–4] rapidly becoming a foreseeable alternative.

From the different actual methods to produce hydrogen: steam methane reforming (SMR),[5] dry methane reforming (DMR),[6–8] coal and biomass gasification,[9] electrolysis,[10,11] water splitting,[12,13] and autothermal processes,[14] SMR is frequently used due to its simplicity and efficiency, however, large quantities of CO_2 are generated in this process.[5] A viable alternative to this process is the catalytic decomposition of methane (CDM), which does not require a water-gas shift step and is a CO_x–free hydrogen process.

CDM shows great methane conversion and hydrogen yield potential. By using different supports for the metal catalyst, CDM could be improved to reach a scalable turning point. Currently, many challenges regarding the surface area and stability of the supported catalyst, the interaction between the metal catalyst and the support and the fine dispersion of the metal catalyst in the support, are yet to be improved.[15]

Studies regarding the effectiveness of different metal-based catalysts for methane decomposition have shown noble metals outstanding catalytic activity, however, their use is restricted because of their low availability and higher cost. Other than noble metals,

Ni-based catalysts have been proved to show the best catalytic performance for CDM reaction,[16–19] decreasing the thermal decomposition temperature from 1200 °C to temperatures between 500 – 600 °C. In addition, formation of carbon nanofibers and/or nanotubes at intermediate temperatures are attractive by-products for electrochemical applications.[20,21]
Hasnan et al. review the nature of catalyst support, preparation method, Ni metal loading on the support, and Ni modification by the addition of second and noble metal promoters for the methane decomposition reaction. Optimal catalysts depend on the nature of their support, their acidity, which promotes methane decomposition, as well as its surface area, morphology and the proper interaction with the active metal, promoting the dispersion of the active phase and stabilizing the catalyst for improved resistance to sintering and coke formation.[22–25]

In this chapter, I evaluate the effect of amorphous aluminosilicate nanosheets (a-ASns) used as supports for Ni particles in CDM and compared them to different a-AS morphologies supports. I further synthesized $Ni(OH)_2$ nanoplates (Ni.np) and evaluated their capabilities as active species and as support itself in CDM. The overview of this study can be seen in **Figure 3.1**. a-AS.np and Ni.np were synthesized in between the layers of amphiphilic molecule (Brij L4) using a two-dimensional reactor in amphiphilic phases (TRAPs),[26–28] and their catalytic performance was evaluated.

I evaluated the addition of different metal promoters for the new synthesized catalysts. Chromium III (Cr^{3+}) species effect in crystalline aluminosilicates effect on the aluminosilicate support was evaluated due to their capacity to improve the acidity of the catalyst and their potential for decreasing coke formation in LDPE cracking and DMR.[6,29] Available literature on the effect of Cr species on CDM is scarce and inconclusive,[30,31] hence I decided to evaluate the effect of Cr^{3+} as a promoter for Ni/a-AS catalyst on its own and with a known metal promoter for CDM; lanthanum III (La^{3+}).[32,33]
Finally, I took advantage of the improved characteristics of Ni.np high surface area, micro/meso porosity and lamellar structure morphology, to use it as a support for well-known active metals for CDM: lanthanum and copper.[15,25,32,34,35]

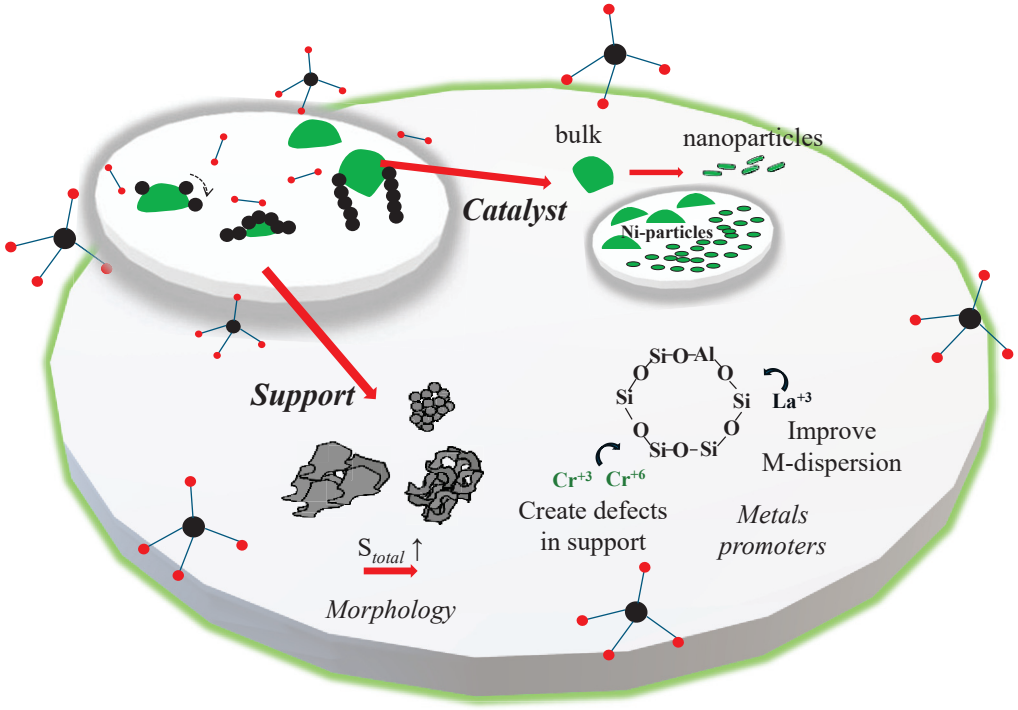

Figure. 3.1 Nanoparticles role in catalytic decomposition of methane, size morphology and metal interaction analysis overview.

3.2 Experimental

3.2.1 Materials

Tetraethylorthosilicate (TEOS, Wako Pure Chemicals Co.), aluminum isopropoxide (AIP, Nacalai Tesque Inc.), sodium hydroxide (NaOH, Wako Pure Chemicals Co.), nickel(III) nitrate hexahydrate (Wako Pure Chemical Co.), lanthanum(III) nitrate hexahydrate (Wako Pure Chemicals Co.), chromium(III) nitrate hexahydrate (Sigma-Aldrich Co.), chromium(III) oxide nonahydrate (Sigma-Aldrich Co.), copper (II) nitrate trihydrate (Sigma-Aldrich Co.), polyethylene glycol decyl ether (Brij L4, Sigma-Aldrich Co.), methanol (Wako Pure Chemicals Co.), heptane (Wako Pure Chemicals Co.) and deionized water were used without further purification to prepare the different supports and Ni-nanoparticles.

3.2.2 Preparation of Amorphous Aluminosilicate Samples

a-AS.b and a-AS.m samples were synthesized in an aqueous solution of TEOS as the source of silicon (16.2 wt%), AIP as the source of aluminum (0.3 wt%) and NaOH as a catalyst (0.6 wt%), agitated at 200 rpm and room temperature. a-AS.b and a-AS.m reaction time was 0.5 h and 2 h, respectively. The final products were centrifuged at 11, 000 rpm for 10 min, washed three times with ethanol and dried at 90 °C for 24 h.

TRAP was used to synthesize a-ASnp. The reaction takes place in the aqueous HL phases of the heptane solution. Composition of TRAP was Brij L4 (6.8 wt%), methanol (1.0 wt%), water (1.8 wt%), TEOS as the source of silicon (0.4 wt%), AIP as the source of aluminum (3.1×10^{-3} wt%) and NaOH as a catalyst (1.4×10^{-2} wt%), agitated at 200 rpm at 15 °C for 24 h. The final products were centrifuged at 11,000 rpm for 30 min and washed three times with ethanol and dried at 90 °C for 24 h.[27,28]

3.2.3 Preparation of Lanthanum Oxide

La_2O_3 was obtained by the calcination of $La(NO_3)_3 \cdot 6H_2O$ in air at 550 °C for 5 h.

3.2.4 Preparation of α-$Ni(OH)_2$ Nanoparticles

α-$Ni(OH)_2$ sheets were synthesized in the HL phases of the heptane solution of Brij L4 (10.7 wt%), methanol (0.7 wt%), water (3.3 wt%), $Ni(NO_3)_2 \cdot 6H_2O$ as the source of Ni (0.3 wt %) and NaOH as a catalyst (2.2×10^{-2} wt%), agitated at 200 rpm at room temperature for 24 h. The final products were centrifuged at 11,000 rpm for 30 min, washed three times with ethanol and dried at 90 °C for 24 h.

3.2.5 Impregnation of Ni-particles

An impregnation process was performed referring to our previous works. [6,36]and modify according to the needs of the different materials. Three types of wet impregnation methods were used for this study.

- $Ni(NO_3)_2 \cdot 6H_2O$

$Ni(NO_3)2 \cdot 6H_2O$ was dissolved in water and put in an ultrasound bath for 30 min. Then the solution of $Ni(NO_3)_2$ was added to the support in a mortar and crushed together until I obtained a homogeneous mixture. The mixture was dried at 90 °C for 24 h and then calcined under air at 550 °C for 5h. Ni-based catalyst obtained from commercial $Ni(NO_3)_2 \cdot 6H_2O$ are referred to as Ni.b/support. Depending on the analysis, 25:75 and 50:50 proportions were used for the loading of Ni.

- α-$Ni(OH)_2$ nanoparticles loading

Since $Ni(OH)_2$ doesn´t dissolve in water, I tried two different approaches substituting the water from the previous impregnation method. α-$Ni(OH)_2$ nanoplates were dissolved in:
- Dissolution in ethanol
- Dissolution in HNO_3 8 % (w/w) solution

The following procedure was the same as the procedure above. After dissolution, α-$Ni(OH)_2$ solution was added into a mortar and crushed together with the support. The mixture was then dried at 90 °C for 24 h and finally calcined under air at 550 °C for 5h. Ni-based catalyst obtained from commercial α-$Ni(OH)_2$ are referred to as Ni.np/support and samples obtained from novel sheets are referred to as Ni.np/support.

3.2.6 Preparation of Lanthanum and Chromium Series Samples

A series of La/Cr supports were synthesized using a two-step wet impregnation method. In the first step La or Cr were added to the a-AS via wet-impregnation method. After at 90 °C for 24 h and calcined at 550 °C for 5 h, the promoted a-AS samples were loaded with 75% (w/w) $Ni(OH)_2 \cdot 6H_2O$, then dried at 90 °C for 24 h and finally calcined under air at 550 °C for 5h.

For La samples, I used a mass range of 3.8 % to 20.9 %. (w/w) La:a-AS.m_{ref} and for chromium, a mass fight between 43.4 – 19.7 (w/w) Cr:a-AS.m_{ref}.

3.2.7 Preparation of La-Cr/a-AS Supports

Three different metal-supports were synthesized using the following methodology.

- La(1.4)a-AS was synthesized in an aqueous solution of TEOS (11.8 wt%), AIP (0.3 wt%), La_2O_3 (2.5×10^{-1} wt%) and NaOH (0.6 wt%).
- Cr(0.7)a-AS was synthesized in an aqueous solution of TEOS (11.8 wt%), AIP (0.3 wt%), Cr_2O_3 (1.2×10^{-1} wt%) and NaOH (0.6 wt%).
- La(1.4) Cr(0.7)a-AS was synthesized in an aqueous solution of TEOS (11.8 wt%), AIP (0.3 wt%), La_2O_3 (2.5×10^{-1} wt%), Cr_2O_3 (1.2×10^{-1} wt%) and NaOH (0.6 wt%).

All samples were agitated at 200 rpm and room temperature for 2 h. The final products were centrifuged at 11000 rpm for 10 min, washed three times with ethanol and dried at 90 °C for 24 h.

3.2.8 Preparation of La(50)Cu(12.5)/Ni.np Catalyst

50 % (w/w) $La(NO_3)_3 \cdot 6H_2O$ and 12.5 % (w/w) $Cu(NO_3)_2 \cdot 3H_2O$ were dissolved in water and put in an ultrasound bath for 30 min. The solution was then added to Ni.np (α-$Ni(OH)_2$ nanoplates) support, previously placed in a mortar, and crushed together until I obtained a homogeneous mixture. The mixture was dried at 90 °C for 24 h and then calcined under air at 700 °C for 5h.

3.2.9 Characterization

The chemical composition of the synthesized supports, Ni-particles and Ni-based catalyst was analyzed by scanning electron microscope-energy dispersive X-ray spectroscopy (SEM-EDX) using a JEOL JCM-7000 microscope at 15 kV. The molecular structures of the synthesized materials were analyzed by Fourier-transform infrared (FT-IR) spectroscopy using a JASCO FT/IR – 4600 with ATR PRO ONE single reflection accessory and X-ray diffraction (XRD) using a PANalytical X'Pert PRO diffractometer with Cu Kα radiation (45 kV and 40 mA).

XRD patterns were smoothen using and FTT filter by Origin2022 and compound reference patterns were generated using JADE 9 software. The morphologies of the particles were observed by transmission electron microscopy (TEM), obtained using a Hitachi H-800 at 200 kV. (N_2) adsorption was used to determine adsorption isotherms, specific surface area (SBET) was calculated using BET method and porous analysis of the materials was obtained from BJH plot applied to the nitrogen adsorption isotherm using a BELSORPmax (MicrotracBEL). Temperature program reduction (TPR) and desorption (TPD) analysis measurements were performed using a BELCAT II equipped with a quadrupole mass spectrometer (MicrotracBEL).

3.2.10 Catalytic Decomposition of Methane (CDM) in Severe Experimental Conditions.

All Ni-based catalysts were pelletized using a hydraulic press at 2 ton for 10 min. Then, the pellets were crushed and sieved using the 300 and 850 micron sieves. The retained fraction was used for the CDM reaction. Harsh reaction conditions over Ni-based catalysts (5.0 mg) and under Ar flow at 550 °C were performed in a BELCAT II instrument (MicrotracBEL). The temperature program reduction consisted of a 2-step stabilization stage. First temperature stabilized at 500 °C under Ar flow, followed by a reduction treatment of pure H_2 stream at the same temperature for 1 h. After the reduction treatment, residual H_2 is removed by Ar while adjusting the reaction temperature to 550 °C. Then, 80 vol% methane gas balanced by Ar was introduced into the reactor at a total flow rate of 25 sccm. H_2 produced during the CDM reaction was detected using a BELMASS instrument (MicrotracBEL). H_2 yield was calculated using a calibration curve using inert Ar as a standard. Deposited carbon amount was analyzed by thermogravimetric analysis (TGA) using a DTG-60 (SHIMADZU). However, it was very difficult to obtain a homogeneous sample and a mass balance was performed instead using the mass gained after the reaction. The mass balance showed that there were no significant problems in our reaction experiments, as seen in **Table 3.1**.

Table. 3.1 Main sample mass balance analysis

Sample	H_2 yield, %	Theoretical CH_4 conv., %	Experimental CH_4 conv., %	error %
Ni.b(75)/a-AS.m	3.00	5.99	6.03	0.60
Ni.np(75)/a-AS.m	3.40	6.81	7.05	3.63
Ni.np(75)/La(1.4)a-AS	2.52	5.04	5.07	0.57
Ni.np(75)/Cr(0.7)a-AS	2.99	5.99	6.07	1.40
Ni.np(75)/La(1.4)Cr(0.7)a-AS	3.86	7.72	8.05	4.39

3.3 Results and Discussion

3.3.1 Amorphous Aluminosilicate Support Characterization

Aluminosilicate based supports including zeolites have shown good synergic effect on CDM reactions,[6,24,34,37] showing high activities for hydrogen yield. In chapter 2 I was able to synthesize controlled a-AS.ns using TRAP's, in this chapter I further evaluate them as supports for Ni particles in CDM.

Two additional batches of a-AS were synthesized, as seen in **Table 3.2**, to compare the morphology effects on the surface area (S_{BET}) and support capabilities for Ni particles in CDM reaction: conventional a-AS synthesized in alkaline solution with reaction times of 0.5 and 2.0 h (a-AS.b & a-AS.m, respectively) and a-AS.ns synthesized in TRAPs.

Table. 3.2 Amorphous aluminosilicate supports samples

Sample	$\bar{\varphi}_{IC/IA}$ (nm)	Si/Al (mol/mol)	S_{BET} (m^2/g^{-1})
a-AS.b	60.0	45.5	18.3
a-AS.s	100.0	21.6	74.0
a-AS.m	45.0	14.4	180.6

X-ray diffraction (XRD) patterns showed that a-AS samples were indeed amorphous as seen in **Figure 3.2.a.** Fourier transformed infrared (FT-IR) analysis confirmed the presence of the main functional groups of the aluminosilicate materials with characteristic Si-O-Si stretching band at 1063 cm^{-1} and different AlO species: Al_2O_3 (455.0 cm^{-1}), AlO_6 (780.0 cm^{-1}) and very small amounts of AlO_4 (561.0 cm^{-1}), as seen in **Figure 3.2.b**.

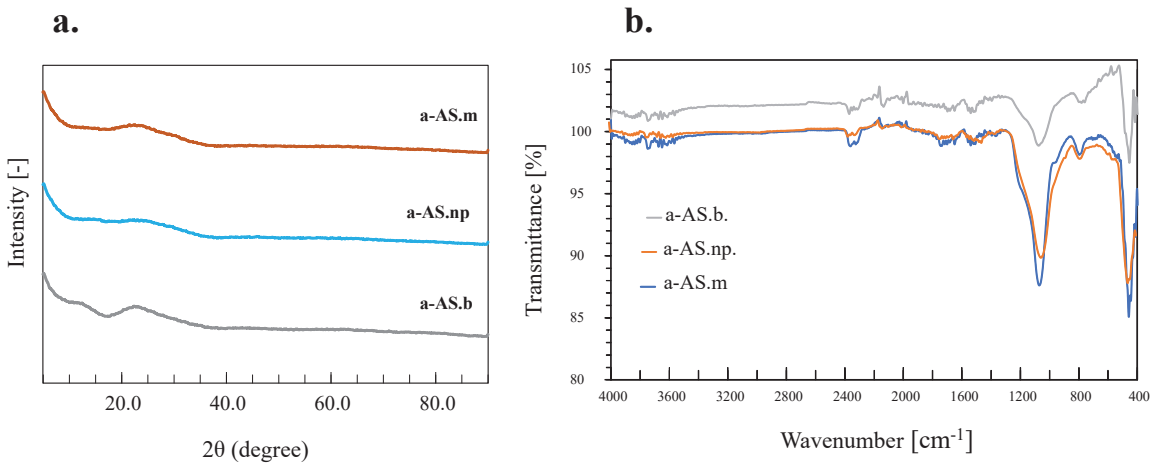

Figure. 3.2 a) XRD patterns of a-AS supports, b) FT-IR spectra of a-AS supports

Although a-AS samples have a similar plate-like primary structure, clear differences in their morphology and intra-crystalline/intra-agglomerate porous ($\bar{\varphi}_{IC/IA}$) size composition were observed by TEM as seen in **Figure 3.3**. Barret, Joyne and Halenda (BJH) method showed the pore volume distribution for the a-AS samples. Both a-AS.b and a-AS.np samples presented $\bar{\varphi}_{IC/IA}$ macropores (60.0 and 100.0 nm, respectively) compared to $\bar{\varphi}_{IC/IA}$ mesopore of 45.0 nm for a-AS.m as seen in **Figure 3.4**.

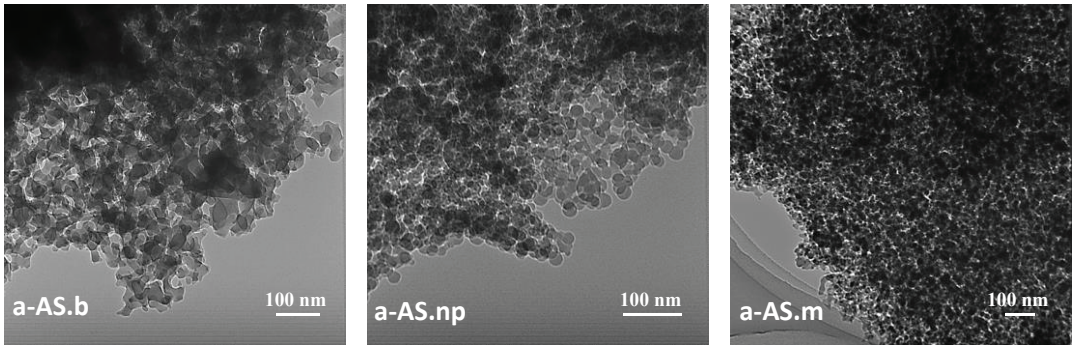

Figure. 3.3 STEM images of a-AS supports

a-AS.b and a-AS.np main shape suggests an isotropic growth, as seen in **Figure 3.3** for a-AS.np, in between the HL phases of amphiphilic molecules, possibly attributed to an induced osmotic pressure between the bilayers containing the reactant phase and solvent. [38,39,40] Consequently, a-AS.np presented disc-shape nanoplates, with lateral aggregation to form a-AS.ns ranging in lengths from 65.1 – 406.7 nm, with an average particle size of 215.5 nm and an average height of 2.8 nm. a-AS.b are bulky materials ($\bar{d}$ = 894.0 nm) with less than 0.5 cm^3g^{-1} $\bar{\varphi}_{IC/IA}$ macropore volume.

Increased reaction time for a-AS.m showed that the same NaOH catalyst acted as an alkaline treatment in a one-pot synthesis for formed a-AS, hence, a characteristic boomerang-like shape and a pear-like shape counterpart, attributed to the breakdown of the original plates. Increased $\bar{\varphi}_{IC/IA}$ pore volume for mesoporous samples could be attributed to the defects generated by the alkaline treatment that create mesoporous when aggregated compared to its plate counterparts as seen in **Figure 3.4**. The specific surface area (S_{BET}) for a-AS.b, a-AS.s and a-AS.m supports were 18.3, 74.0 and 180.6 m^2g^{-1}, respectively.

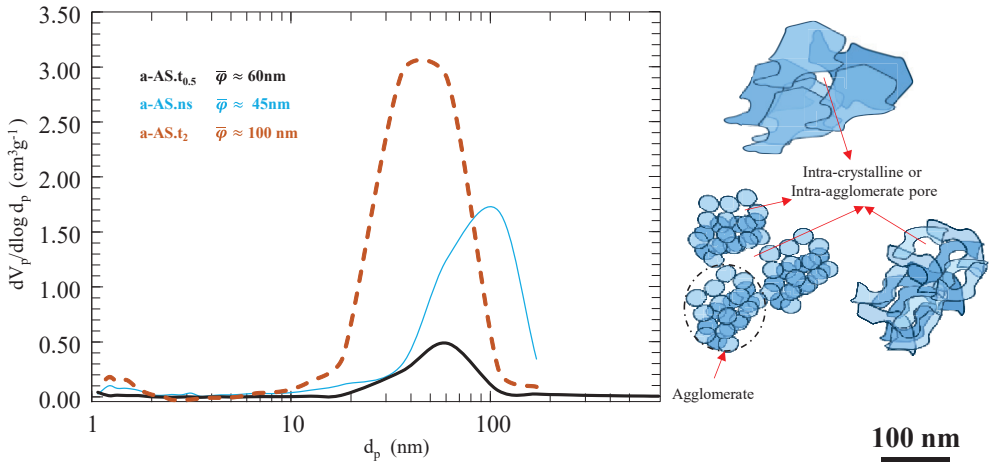

Figure. 3.4 BJH plot for a-AS samples

a-AS morphology effect was evaluated by loading 75.0 % (w/w) nickel nitrate ($Ni(NO_3)_2{\cdot}6H_2O$) using a wet impregnation method, dried and calcined at 550 °C for 5 h to obtain Ni-based catalyst conformed of dispersed NiO on the a-AS surface. From this point on, I will refer to Ni-particles originated from bulk $Ni(NO_3)_2{\cdot}6H_2O$ as Ni.b.

Table. 3.3 Ni.b catalyst supported in a-AS

Sample	Si/Al (mol/mol)	Ni/Si (g/g)	S_{BET} (m^2g^{-1})
Ni.b(75)/a-AS.b	6.2	1.8	9.5
Ni.b(75)/a-AS.np	9.4	1.1	11.9
Ni.b(75)/a-AS.m	8.9	0.8	73.6

Table 3.3. shows the Ni/Si [-] loading capacity for each support observed by EDX, FE-SEM and TPR analysis. a-AS.b showed the highest amount of nickel per gram of silica compared to the other samples.

However, we can observe in **Figure 3.5** that a-AS.b loaded Ni-particles are bulky spheres with closed/closing powder morphology ($\bar{d}$ = 234.6 ± 50.3 nm), which has been found to encapsulate impurities, decrease the rate of nickel reduction and wear out industrial equipment,[41] in agreement with TPR experimental data, where H_2 conversion was almost nonexistent, as seen in **Figure 3.6**.

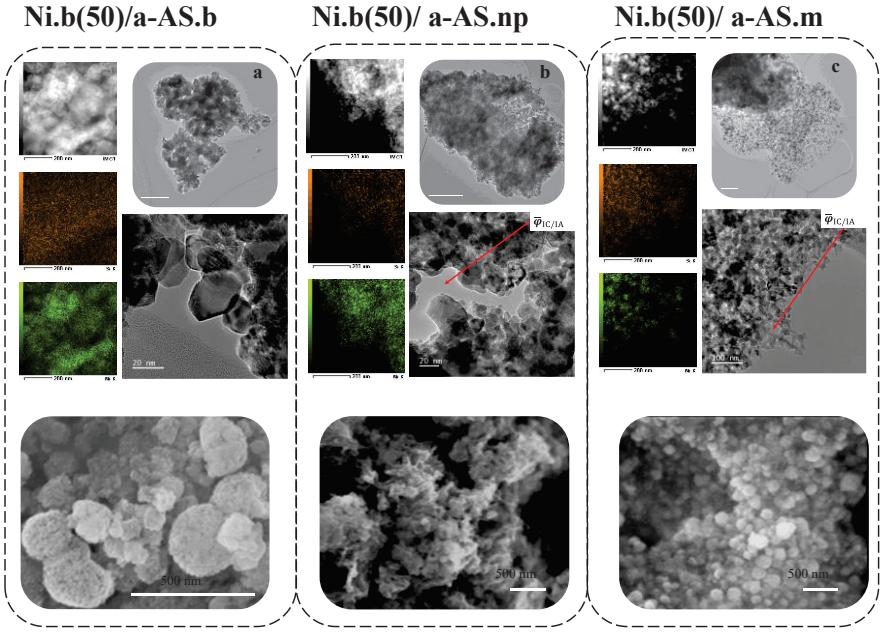

Figure. 3.5 STEM/HAADF and FE-SEM of Ni.b loaded a-AS samples

a-AS.np didn't show a clear nickel morphology however, FE-SEM observation suggests that Ni-particles are in between a spherical open powder and aggregated crystals. Limiting the nucleation of nickel particles to flat surfaces promoted a vertical agglomeration of Ni-particles and vertical growth. Available free Ni-particles promoted CDM reaction; however, it was hindered by the unfinished dispersion of Ni-particles.

Even when a-AS.m showed the lowest amount of Ni per gram of Si, TPR analysis showed the best CDM conversion. FE-SEM showed that Ni-particles were finely dispersed throughout the support and presented a truncated octahedron morphology. My conclusion is that porous materials with increased specific surface area promote the dispersion of Ni-particles throughout the support, avoiding agglomeration, reducing the size of the Ni-particles and increasing their dispersion.

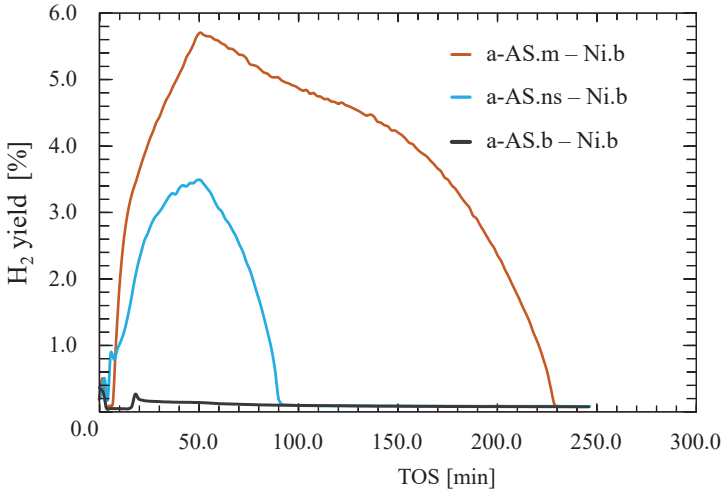

Figure 3.6. H_2 evolution on time for catalytic methane decomposition over Ni.b(75)/a-AS.b, Ni.b(75)/a-AS.np and Ni.b(75)/a-AS.m at severe reaction conditions (m_{cat} =5.0 mg, 20.0 sccm CH_4/5 sccm Ar, 550.0 °C).

3.3.2 Metal-Supports Interactions

I further investigated the effect of metal promoters Cr and La on the Ni.b/a-AS.m catalysts. For this purpose, a new batch of mesoporous amorphous aluminosilicate (a-AS.m_{ref}) was synthesized due to the amount of sample required, using the previous established conditions for a-AS.m synthesis.

Table 3.4. Ni.b catalysts supported in a-AS, promoted with La^{3+} and Cr^{3+} at different [C]

	Sample	Si/Al (mol/mol)	Ni/Si (g/g)	La/Si (g/g)	Cr/Si (g/g)	S_{BET} (m^2g^{-1})
Reference	Ni.b(50) / a-AS.m_{ref}	16.2	0.25			64.8
La-series	Ni.b(50) / La(3.8)a-AS.m_{ref}	6.0	0.58	0.04		53.3
	Ni.b(50) / La(5.2)a-AS.m_{ref}	8.4	0.53	0.06		51.5
	Ni.b(50) / La(8.2)a-AS.m_{ref}	7.7	0.66	0.09		60.0
	Ni.b(50) / La(20.9)a-AS.m_{ref}	7.2	0.61	0.26		62.3
Cr-series	Ni.b(50) / Cr(3.4)a-AS.m_{ref}	8.3	0.55		0.01	36.1
	Ni.b(50) / Cr(4.8)a-AS.m_{ref}	7.1	0.56		0.02	31.4
	Ni.b(50) / Cr(7.4)a-AS.m_{ref}	7.7	0.58		0.03	25.8
	Ni.b(50) / Cr(19.7)a-AS.m_{ref}	6.3	0.60		0.09	52.9

AS.m_{ref} samples were doped with promoters (La and Cr) and active metal (Ni) in a two-step wet impregnation method. **Table 3.4** shows a summary of La and Cr samples analyzed. It was interesting to note that the amount of Ni loading was rather stable throughout the La and Cr series.

First, I added $La(NO_3)_3 \cdot 6H_2O$ or $Cr(NO_3)_3 \cdot 6H_2O$ to a-AS.m_{ref} at different concentrations via a wet impregnation method, then dried for 24 h and calcined at 550°C for 5 h. Then 50 % (w/w) $Ni(NO_3)_3 \cdot 6H_2O$ was added to the newly promoted support via a wet impregnation method, dried for 24 h and calcined at 550°C for 5 h.

Chromium oxides has been reported as an effective promoter in diverse catalytic reactions due to its ability to protect the catalyst from sintering at high temperatures and its ability to avoid coke formation,[6,29,42] however, for a-AS.m supports, a decrease in H_2 yield in all combinations compared to unpromoted a-AS.mref was observed, as seen in **Figure 3.7**. FE-SEM showed high sintering at 550.0 °C with increased concentration of Cr and poor crystallization of Ni particles with no reaction at all for Ni.b(50) / Cr(19.7)a-AS.m_{ref}. This suggests strong interactions between Cr species and hydroxyl groups of a-AS,[29,42] and further strong interactions with Ni particles.

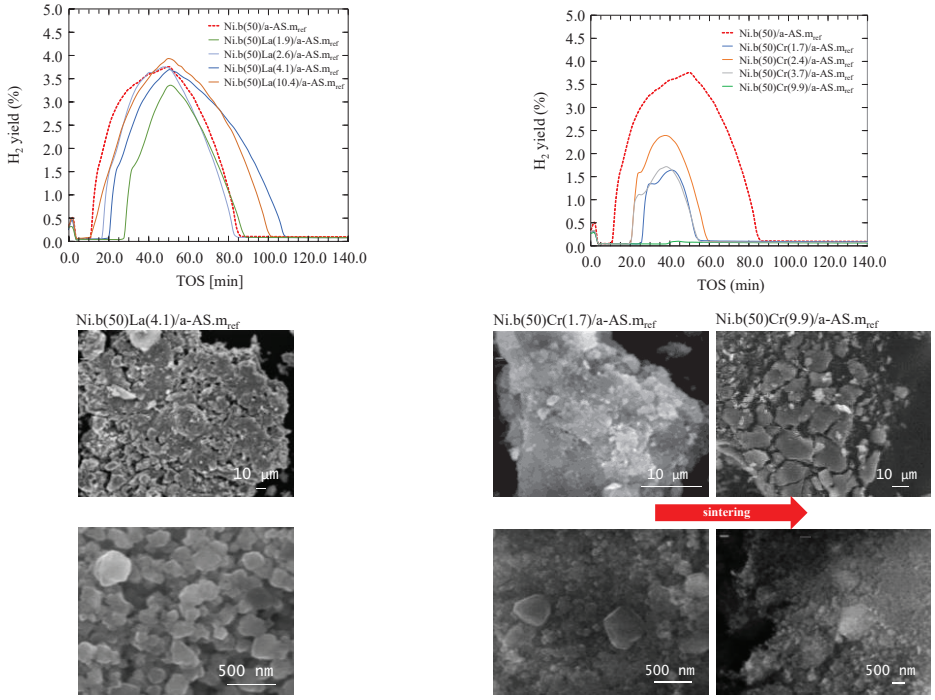

Figure 3.7. H_2 evolution on time for catalytic methane decomposition over Ni.b(50) / La(wt.%)a-AS.m_{ref}, Ni.b(50) / Cr(wt.%)a-AS.m_{ref} at severe reaction conditions (m_{cat} =5.0 mg, 20.0 sccm CH_4/5 sccm Ar, 550.0 °C).

On the other hand, lanthanum oxide has been reported to increase the dissociation rate of C-H bond by electron charge transfer to nickel,[32,35] and promote fine dispersion of nanocrystalline nickel particles in the lanthanum oxide matrix formed from the reduction of lanthanum nickel oxide.[43]

I was able to confirm by FE-SEM that in fact, nanocrystalline nickel particles were formed. H_2 yield was improved compared to unpromoted a-AS.m_{ref}, starting from a concentration of 7.4 % (w/w) of $La(NO_3)_3 \cdot 6H_2O$ in the support.

3.3.3 Ni-particle Nanoplates

Section 3.3.1 showed that the support morphology plays a crucial role in the Ni-particle morphology and consequently its overall catalytic performance. Hence, I also studied Ni-particle morphology.

I synthesized Ni.np using the TRAP method as described in the experimental section. Both XRD and FT-IR confirmed that α-$Ni(OH)_2$ was obtained. Because of the broadening effect of nanoparticles, XRD pattern of α-$Ni(OH)_2$ showed limited peaks, however, characteristics (003), (006), (009), (101) and (110) peaks were observed, as seen in **Figure 3.8a**. [45 – 47]

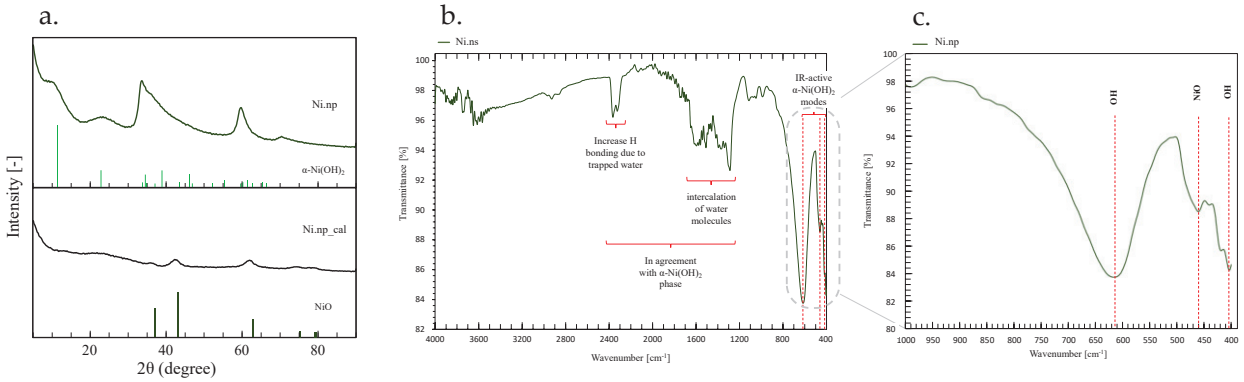

Figure 3.8. a) XRD pattern of α-$Ni(OH)_2$ (upper pattern) and NiO nanosheets (lower pattern), b) FT-IR pattern of α-$Ni(OH)_2$, c) FT-IR pattern of active α-$Ni(OH)_2$ modes at 400, 460 and 610 cm^{-1}

Figures 3.8b and 3.8c show the α-$Ni(OH)_2$ FT-IR patterns for the synthesized Ni-nanoparticles, with characteristic vibrational bands 420, 460 and 612 cm^{-1} associated to the functional groups OH, NiO and OH, respectively, were observed. [51 – 53] Additionally, enlarged interlayer space allowing intercalation of water molecules, observed in the vibrational bands between 1,200.0 – 1,600.0 cm^{-1} as well as the increased vibrational band associated to hydrogen bonding observed in the vibrational band at 2,320.0 – 2,360.0 cm^{-1} due to increased trapped water confirmed that in fact α-$Ni(OH)_2$ was obtained.

I successfully obtained aggregated Ni sheets comprised of small nanoplates of 23.2 nm in diameter and an average height of 8.4 nm with a high surface area of 373.74 m^2g^{-1}, synthesized in TRAPs. Aggregated porous nickel sheets showed an average size of 3,700.0 x 2,100.0 nm (*l* x *w*) with an average thickness of 209.2 nm. Based on TEM analysis the self-assembly mechanism of lamellar nickel sheets resembles the growth mechanism proposed by Parvin and Cho for 3D flower-like $Ni(OH)_2$, but in our case, in 2D as seen in **Figure 3.9**. [51 – 53] Ni.np showed a predominant lamellar structure,[51,52] with low crystallization due to low temperature synthesis condition (T_{amb}) and the confining effects of the HL phases of TRAPs, restricting aggregation in the y axis.

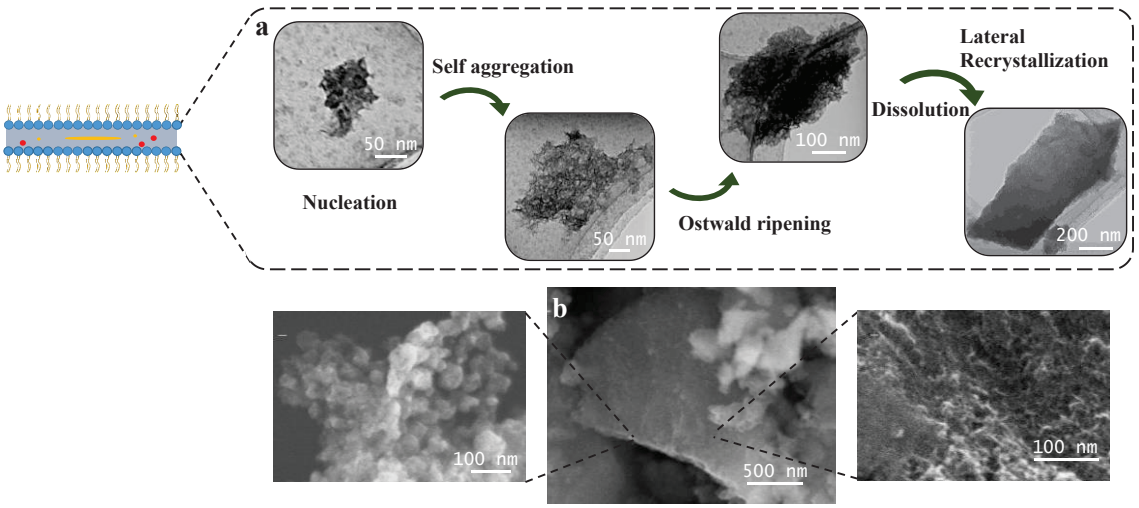

Figure. 3.9 Proposed self-formation mechanism of Ni.np in TRAPs

3.3.4 Pure Ni.np Catalyst

$Ni(OH)_2$ nanoplates (Ni.np) require high temperature treatment (calcination) to reduce the catalyst and activate it for the CDM, which facilitates the crystallization of the nanoplate's unit cells, migrating from a lamellar structure to defined crystals and acting as its own support. As expected, the crystallinity of Ni particles was modified and it's reflected in the pore morphology. As seen in **Figure 3.10**, at 300 °C, only micropores disappear, but mesopores keep their size around 4.5 nm. However, when calcined at 550 °C, both previous micropores and mesopores disappear, and new mesopores ($\overline{\varphi}_{IC/IA}$ = 35 nm) are created suggesting that the degree of crystallization is correlated to the calcination temperature

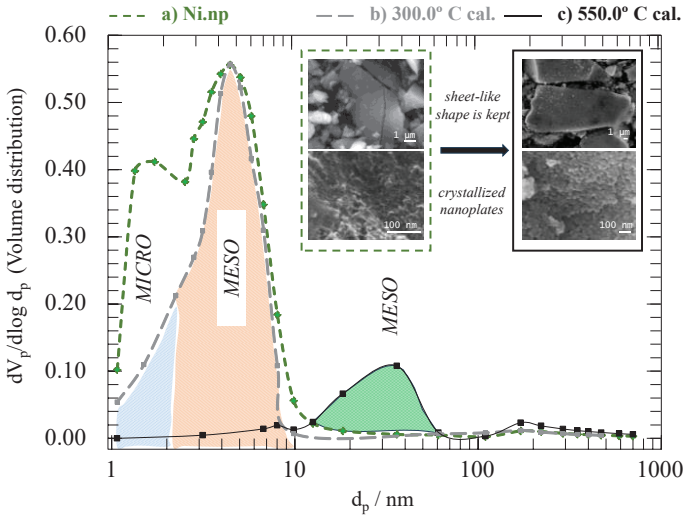

Figure. 3.10 Porous size distribution of a) Ni.np (α-Ni(OH)$_2$) b) calcined Ni.np (NiO) at 300°C and c) calcined Ni.np (NiO) at 550°C

The resulting crystal formation creates openings in the sheet-like structures resulting in the loss of micropores. This behavior is attributed to the conversion and crystallization of α-Ni(OH)$_2$ to NiO. Most samples were calcined at 550 ° C, hence, crystals are in between an octahedron and cubic crystal shape,[44] as seen in FE-SEM images.

Table. 3.4 Pure Ni samples

Sample	S_{BET} (m^2g^{-1})
$Ni(NO_3)_2{\cdot}6H_2O$	13.3
Ni.b (NiO)	7.8
Ni.np ($Ni(OH)_2$)	373.7
Ni.np-300 (NiO)	184.2
Ni.np-550 (NiO)	8.2

Since some of the first approaches to the adsorption of N_2 on pure and promoted nickel catalysts, it has been known that there is some degree of chemisorption on the nickel surface and that is very sensitive to the previous history of the catalyst as seen in **Table 3.4**.[45] This results are in agreement with previous studies on nickel catalysts, where even at low specific surface area of improved Ni-catalysts, the catalytic activity is improved.[45,46] This makes us wonder the significance of surface area for CDM and whether crystallization and metal interactions with support plays a more compelling role in the decomposition mechanism.

I also compared the catalytic activity of pure Ni.np and Ni.b, both calcined at 550° C. Ni.np presented a clear improvement on H_2 yield performance and catalyst stability, suggesting that aggregated nickel nanoplates in the core acted as support of superficial crystallized Ni nanoplates, as seen in Figure 3.11.

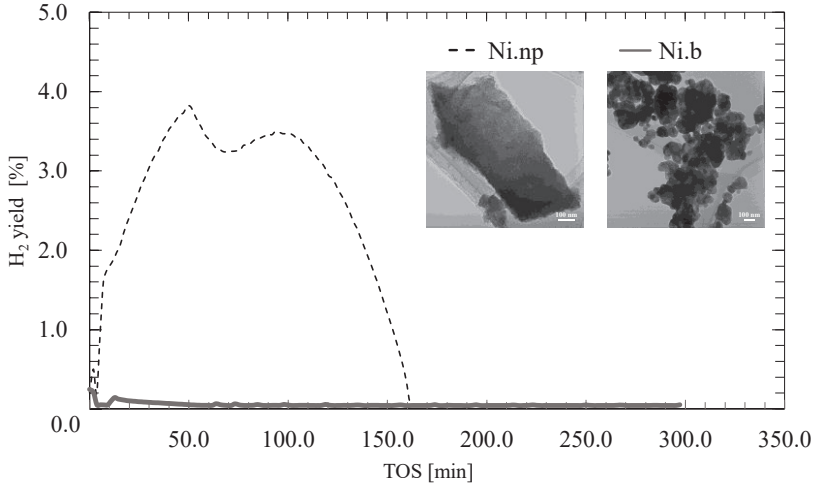

Figure. 3.11 H_2 evolution on time for catalytic methane decomposition of pure Ni at severe reaction conditions (m_{cat} =5.0 mg, 20.0 sccm CH4/5 sccm Ar, 550.0 °C).

3.3.5 Loading Capability of Ni.np

The loading capability of new synthesized Ni.np a-AS was also evaluated. First, we tested a wet impregnation method using ethanol and an ultrasound bath for 30 min to disperse the Ni.np, followed by the loading in a-AS.m, dried for 24 h and calcined at 550.0 °C. **Table 3.5** summarizes main characterization of loaded samples.

Table 3.5 EDX analysis and S_{BET} for the impregnation method effect on the loading of Ni-particles.

Sample			Wet-I_{method}	Si/Al	Ni/Si (g/g)	S_{BET} (m^2g^{-1})
Ni.b(75)	/	a-AS.m	$Ni(NO_3)_2{\cdot}6H_2O$ /H_2O	8.88	0.8	73.6
Ni.np(75)	/	a-AS.m	Ni.np/ethanol	5.1	1.7	56.0
Ni.np(75)	/	a-AS.m	Ni.np/8% HNO_3	6.33	2.2	59.3

Figure 3.12.b shows that the impregnation with ethanol as a solvent or dispersion (Ni.np/ethanol) was not supported on a-AS.m and performed poorly at CDM. I concluded that Ni.np was not loaded onto the a-AS support. Alternatively, I tried a second method using an 8 % HNO_3 solution (w/w) which solved the loading problem, but the Ni.np structure was decomposed.

Although an improvement on the H_2 yield was seen when using dissolved Ni.np compared to Ni.b on a-AS.m, I was not able to conclude that it was only because of the effect on the difference in size and morphology of dissolve Ni.b and Ni.np particles since the source of Ni was different and even when using the same ratio of Ni-source/support, Ni.np mass percentage of Ni is higher than Ni.b. Nonetheless it was noteworthy to mention that Ni.np showed smaller particle size with truncated octahedral structures compared to bigger spherical Ni.b.

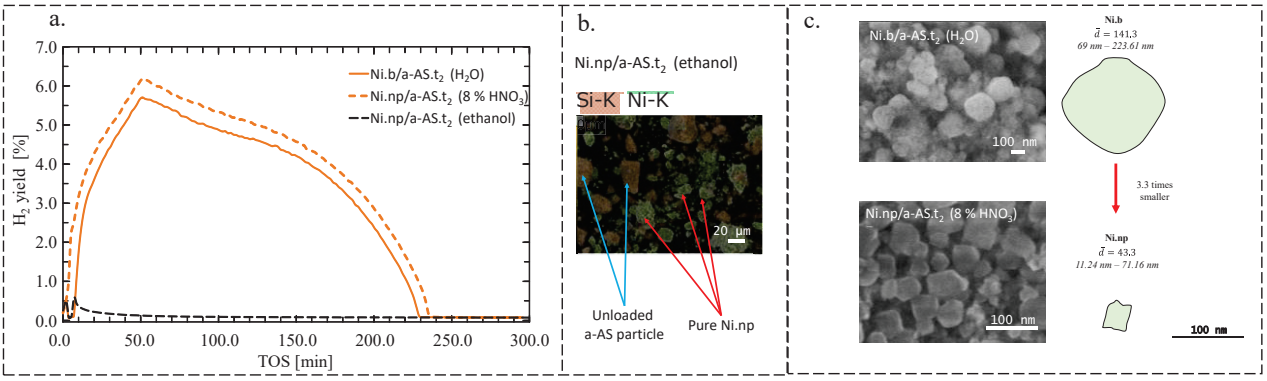

Figure. 3.12 a) H_2 evolution on time for catalytic methane decomposition at severe reaction conditions (m_{cat} =5.0 mg, 20.0 sccm CH_4/5 sccm Ar, 550.0 °C) of Ni.b and Ni.np over a-AS.m, b) MAP analysis of unloaded Ni.np on a-AS.m support c) FE-SEM images of Ni.b and Ni.np particles loaded on the surface of a-AS.m support.

Based on these results, the performance of Ni/a-AS catalyst cannot be determined only by the amount of dispersed nickel in the final catalyst or the area of the catalyst, since other factors such as the morphology of the unit cells, overall larger aggregates morphology and porous structure and the interactions between the active phase and support are key factors on the catalytic performance of CDM reaction as well.

3.3.6 Promoted a-AS on Dissolved Ni.np

I also evaluated the combined effect of La and Cr promoters in dissolve Ni.np. I incorporated 0.7 % (w/w) $Cr_2O_3{\cdot}9H_2O$ and 1.4 % (w/w) La_2O_3 during the polymerization step of TEOS and AIP for the synthesis of newly promoted a-AS to evaluate the impregnation effect of the promoters into the support. **Table 3.6** summarizes main characterization of La-Cr promoted samples.

Table 3.6 EDX analysis and S_{BET} for the La-Cr promoted a-AS samples, loaded with Ni.np by dissolution of 8% HNO_3.

Sample	Si/Al (mol/mol)	Ni/Si (g/g)	La/Si (g/g)	Cr/Si (g/g)	S_{BET} (m^2g^{-1})
Ni.np(75) / La(1.4)a-AS	4.9	2.9	0.12		55.7
Ni.np(75) / Cr(0.7)a-AS	2.5	3.0		0.35	88.2
Ni.np(75) / La(1.4) Cr(0.7)a-AS	1.1	5.6	0.61	0.26	84.6

EDX showed the average composition of the different metals in the a-AS structure, where a considerable increment of La/Si and Cr/Si compared to the Cr and La samples from the study in section 3.3.2 was observed, suggesting that metallic particles were also encapsulated by a-AS aggregates, limiting the metallic promoters interaction with Ni-particles, which would also support the fact that Ni.np(75)/Cr(0.7)a-AS sampled didn't hindered H_2 generation as much as it was expected and Ni.np(75)/La(1.4)a-AS didn't improve it.

Ni.np(75)/La(1.4)a-AS and Ni.np(75)/Cr(0.7)a-AS showed similar behaviors to the Cr and La series from section 3.2, decreasing the H_2 yield when Cr promoters were used and a more complex behavior for La species. Even when Ni.np(75)/La(1.4)Cr(0.7)a-AS is the combination of the mass reactant's proportions for La_2O_3 and $Cr_2O_3{\cdot}9H_2O$, a great increment in the amount of La loaded into the a-AS support was observed, in agreement with the size increase of La particles in the La(1.4)Cr(0.7)a-AS compared to La(1.4)a-AS, from 39.2 nm in diameter to 103.6 nm when Cr species are added.

FT-IR showed the main vibrational bands of LaO, CrO, AlO and SiO species, as seen in **Figure 3.13**. Main attributes of SiO and AlO functional groups were maintained,[47,48] confirming the addition of metal-oxide species into the a-AS surface and framework, confirmed as well by XRD analysis as seen in **Figure 3.14**.

Furthermore, in La(1.4)Cr(0.7)a-AS the 670 cm^{-1} vibrational band was not visible, possibly due to the absence of strong interactions of coordinated La^{3+} with 5- or 6- coordinated Al^{3+}, suggesting weak interactions between La_2O_3 and aluminosilicate. On the other hand, peaks derived from CrOH and CrO were clearly visible, suggesting favorable interactions with Cr_2O_3 and the aluminosilicate support.[48,49] Finally, the insertion of Cr species could have improved the interaction of La species with active species, hence, overall H_2 yield of the bimetallic La-Cr a-AS support was improved as seen in **Figure 3.15**.

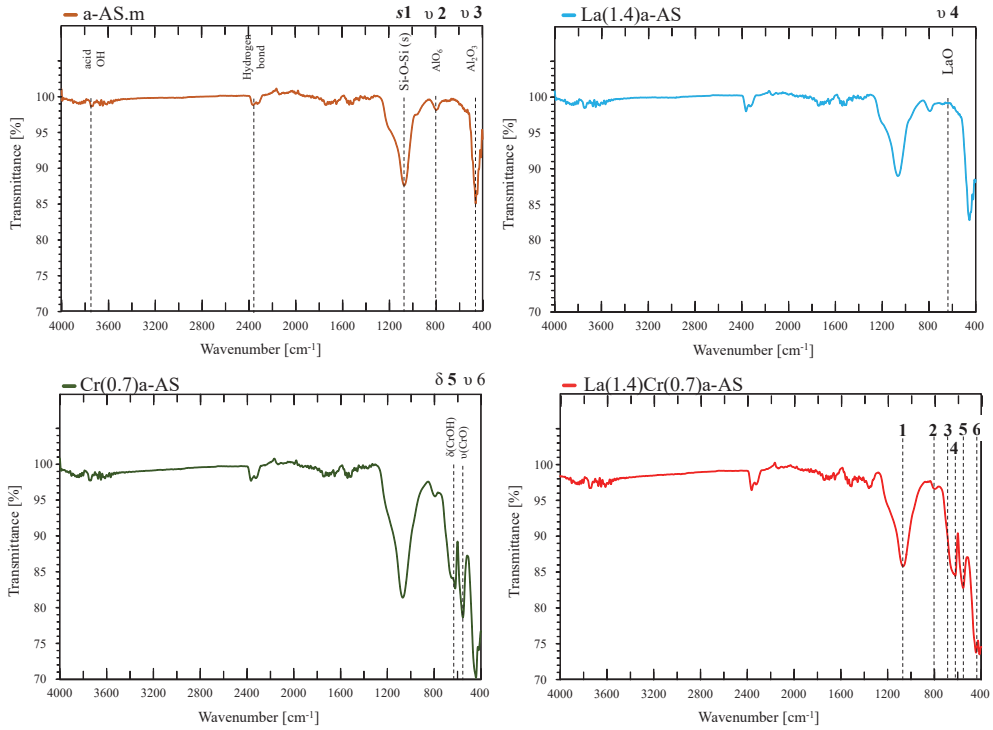

Figure. 3.13 FT-IR spectra of metal-amorphous aluminosilicates supports

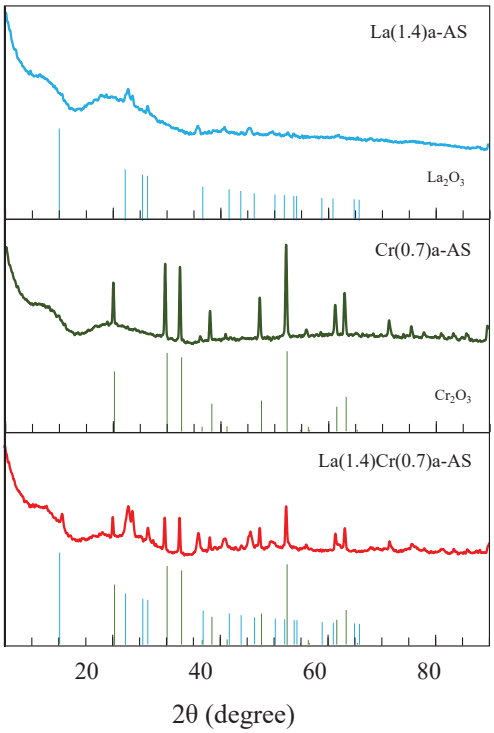

Figure. 3.14 XRD patterns of metal-amorphous aluminosilicates supports

XRD pattern of La(1.4)Cr(0.7)a-AS showed the characteristic peaks of a trigonal system of La_2O_3. In the case of Cr species, both CrO (560 cm^{-1}) and CrOH (620 cm^{-1}) vibrational frequencies were observed when adding Cr to the supports (Cr(0.7)a-AS and La(1.4)Cr(0.7)a-AS),[47] confirmed as well in the XRD patterns for Cr_2O_3.

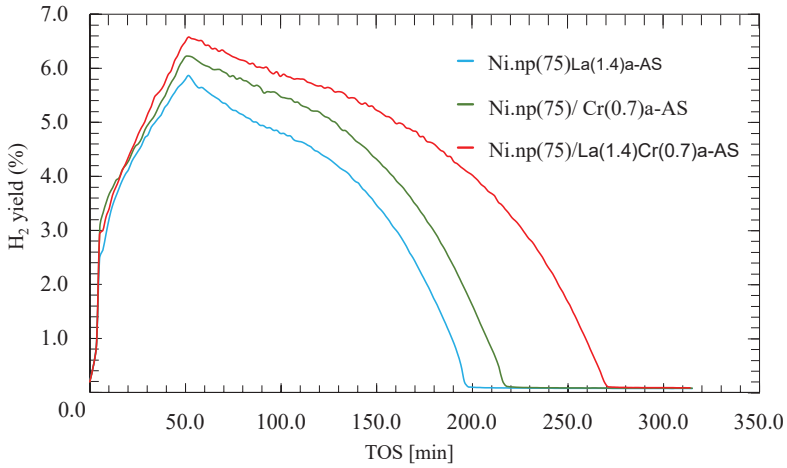

Figure. 3.15 H_2 evolution on time for catalytic methane decomposition over Ni.np(75)/ La(1.4)a-AS, Ni.np(75)/Cr(0.7)a-AS andNi.np(75)/La(1.4) Cr(0.7)a-AS at severe reaction conditions (m_{cat} =5.0 mg, 20.0 sccm CH_4/5 sccm Ar, 550.0 °C).

Adsorption analysis showed that both a-AS.m and La(1.4)a-AS have a clear Type IV isotherm derived from mesoporous species, however, when using Cr species, the porous size decreases from 50 nm to 20 nm approximately. Even when a Type IV isotherm is still predominant in Cr-supports, Figure **3.16.c and 3.16d**, showed a significant reduction in the mesoporous size and availability due to the addition of crystal structures in the amorphous framework resulting in a constraining effect of the amorphous framework. **Figure 3.16.e** shows the pore volume distribution, showing that Cr has a positive effect by creating 18 nm mesoporous, which in the presence of lanthanum becomes beneficial for Ni loading and CDM.

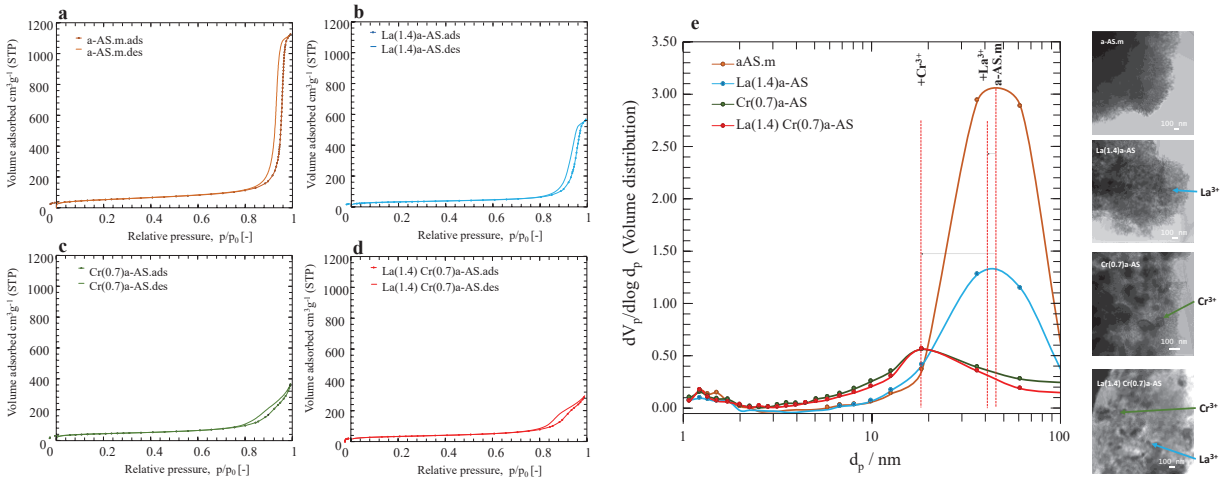

Figure. 3.16 Adsorption-desorption isotherms promoted AS supports. a) a-AS.m b) La(1.4)a-AS , c) Cr(0.7)a-AS d) La(1.4) Cr(0.7)a-AS., e) Porous size volume distribution behavior for La(1.4)a-AS, Cr(0.7)a-AS and La(1.4) Cr(0.7)a-AS (left), and TEM images of supports (right)

H_2-TPR profile of the bi-metallic promoter La(1.4)Cr(0.7)a-AS. As seen in **Figure 3.17**, several reductions bands were observed, due to the presence of La^{3+} and Cr^{3+} and their interaction with the support and the Ni-particles, clearly divided into two main areas; weak interactions from 150 – 400 °C and strong interactions from 700 – 1000 °C.

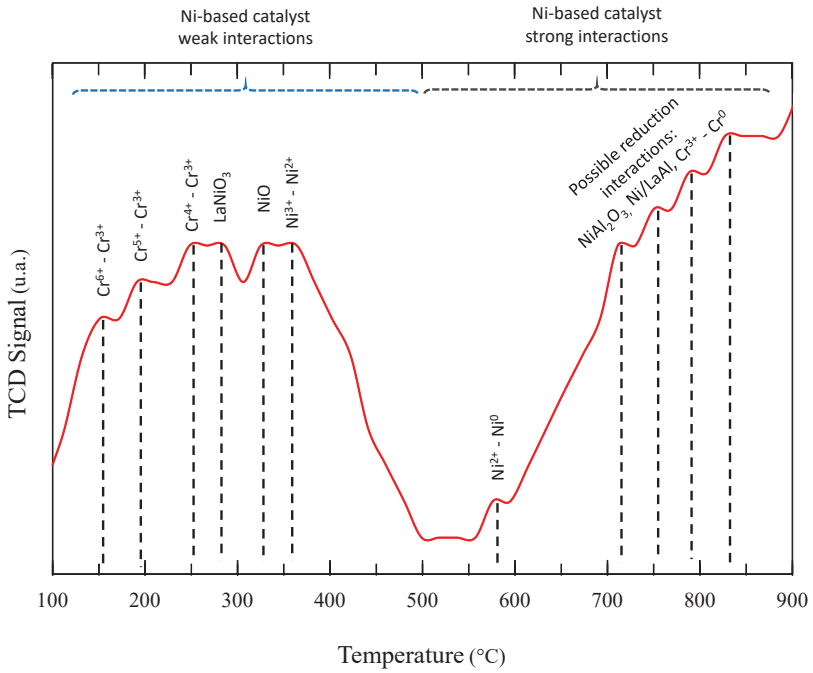

Figure. 3.17 H_2 TPR analysis of Ni.np(75)/ La(1.4)Cr(0.7)a-AS

In the weak series, the first three peaks match different references for the Cr species reduction (Cr^{6+}, Cr^{5+} and Cr^{4+} to Cr^{3+}), next, the 286 °C peak might be allocated to weak interactions of Ni with La^{3+} followed by the reduction of Ni species (bulk NiO, Ni^{3+} – Ni^{2+} and Ni^{2+} – Ni^{0}) in agreement with several studies.[50–52] This region suggests that even at low temperatures, some CDM could still be achieved due to highly reactive chromium species that allow dehydrogenation. Potentially decreasing the overall required reaction temperature of the CDM.

In the strong interaction series, 4 peaks can be observed, attributed to strong interactions between Ni-La and Ni-Al and crystalline Cr_2O_3 (Cr^{3+} – Cr^{0}).[53–56] The strong interaction of Ni-particles with Al and La species improves the stability of the particles in the support. This strong interaction not only helps avoid sintering of the Ni-particles at the calcination step of the catalyst preparation, but also extend the lifetime of the Ni-particles by preventing their detachment from the support when carbon nanotubes are forming.

3.3.7 Ni.np as Supports of Rare Earth/Transition Metals

I also evaluated the potential of Ni.np as a support for known promoters of CDM: La and Cu metallic species. [25,35,43,50,57] La(50)Cu(12.5)/Ni.np catalyst was synthesized by the addition of $La(NO_3)_3{\cdot}6H_2O$ and $Cu(NO_3)_2{\cdot}3H_2O$ by wet impregnation method to Ni.np supports, dried for 24 h and calcined at 700 °C for 5 h. The presence of NiO, La_2O_3 and CuO were confirmed by XRD as seen in **Figure 3.18**.

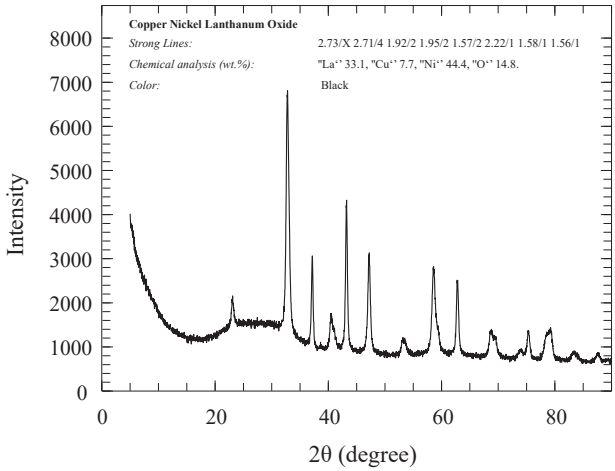

Figure. 3.18 XRD of La(50)Cu(12.5)/Ni.np

*Synthesized catalyst chemical structure matches sample prepared by Bazuev, G., Inst. of Solid-State Chemistry, Ekaterinburg, Russia. Mixture of 'La_2 O_3' (99.99%), 'Cu O' (99.9%) and 'Ni O' (99.9%) was annealed in air at 950 C for 30 hours and then quenched on a copper plate.

Figure 3.19 shows the morphology of the new La-Cu bimetallic catalyst supported in Ni.np. Copper particles showed hexagonal nanodisc structures [58] leaving a hexagonal-shaped porous when aggregated.

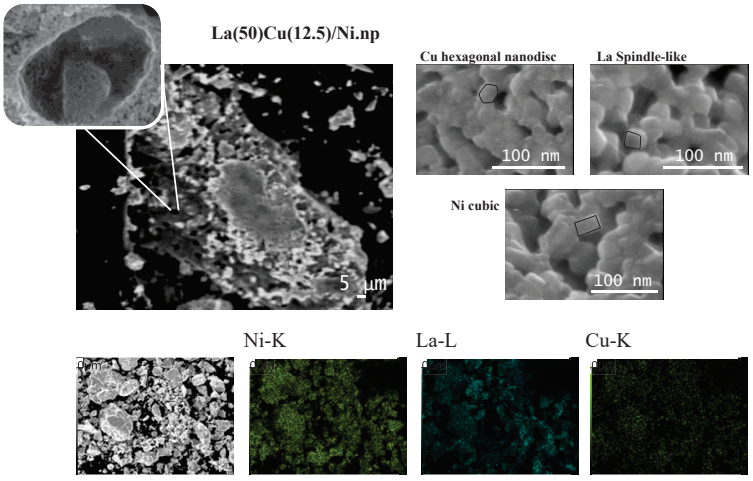

Figure. 3.19 FE-SEM images and MAP analysis of La(50)Cu(12.5)/Ni.np

This aggregation pattern agrees with the transition from calcined Ni.np mesoporous to the new catalyst macro porous of 65 nm diameter in average as seen in **Figure 3.20** and the aggregation pattern of metals over Ni.np sheets creating visible holes in the aggregated La-Cu particles. Lanthanum particles showed spindle like structure [59,60] and Ni particles, cubic like structure. [55]

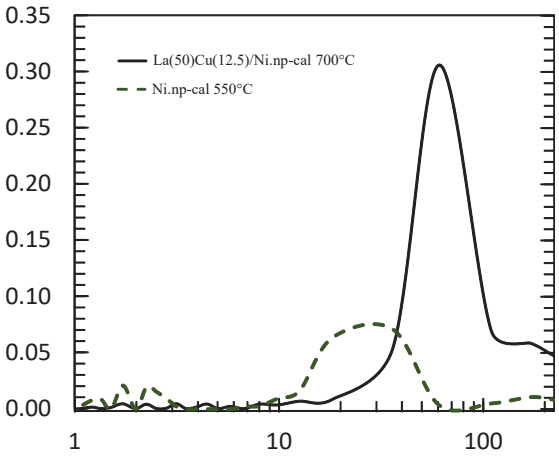

Figure. 3.20 Pore volume distribution of La(50)Cu(12.5)/Ni.np-cal at 700°C vs Ni.np-cal at 550°C

I tested this novel catalyst at 550 °C to compare it with previous samples, showing a huge improvement in stability in severe conditions, more than 400 min. A general improvement in H_2 generation compared to pure Ni.b, Ni.np, all Ni(50) samples and improved stability compared to Ni(75) samples considering that La(50)Cu(12.5)/Ni.np uses less mass % of Ni-source than all previous samples, as seem in **Figure 3.21**.
I hypothesized that increased stability might be associated to the combination of different size carbon nanotubes created by the combination of hexagonal copper nanodiscc particles and smaller octahedral nickel particles, creating gaps in between the nanotubes and avoiding aggregation and deactivation by carbon deposition, as seen in **Image 3.1**.
However, the deactivation at this temperature was around 80 min due to the increased deposition of carbon over the active sites.

Finally, **Figure 3.22** shows the La(50)Cu(12.5)/Ni.np catalyst analysis by NH_3 TPD, CO_2 TPD and H_2 TPR, of this catalyst. NH_3 TPD profile didn't show any peaks, hence no acid sites were detected. CO_2 TPD showed two peaks at 140 °C and 680 °C indicating that the catalyst has basic properties.

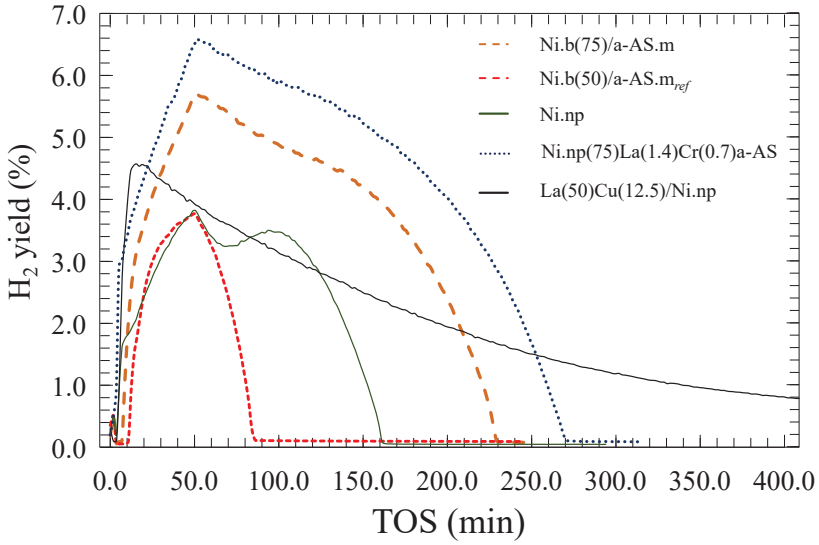

Figure. 3.21 H_2 evolution on time for catalytic methane decomposition over La(50)Cu(12.5)/Ni.np at severe reaction conditions (m_{cat} =5.0 mg, 20.0 sccm CH_4/5 sccm Ar, 550.0 °C).

H_2 TPR showed three main peaks. The first peak (around 100 – 300 °C) corresponds to Cu reductions and interactions with Ni, weak interactions between La-Ni ($LaNiO_3$) and reduction of NiO and Ni^{3+} - Ni^{2+} takes place. Around 500 °C we have a clearly defined peak which is the main peak for Ni species reduction and finally, the last peak (starting around 650 °C) shows a stable activity up to 900 °C for strong interactions between Ni-La species and reduction of La species in agreement with La oxide's electron transfer capabilities. [32]

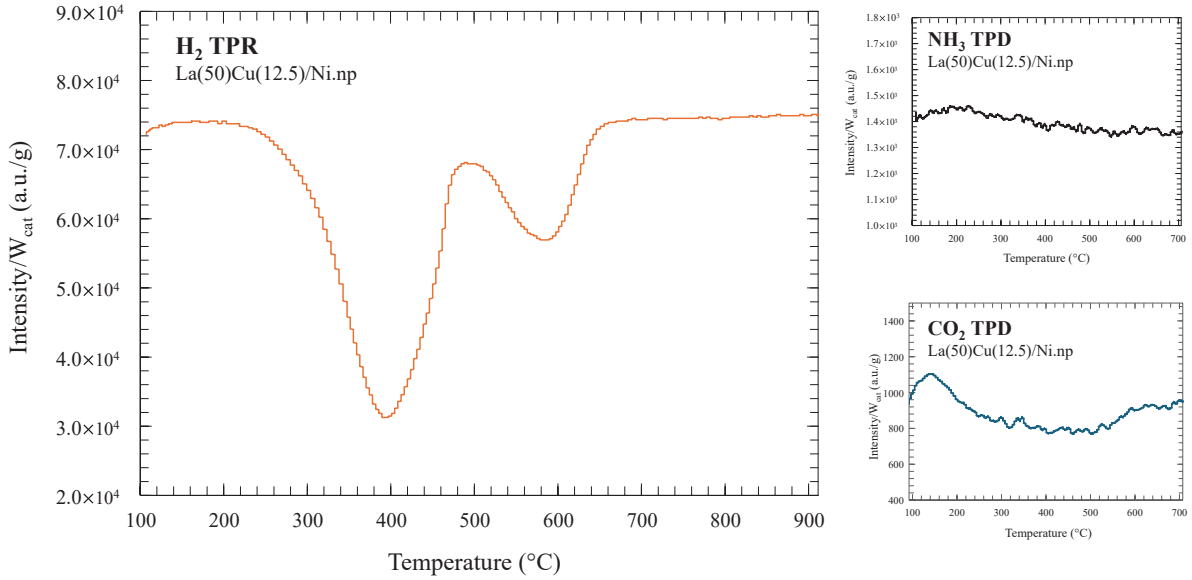

Figure. 3.22 Full catalyst characterization (H_2 TPR – NH_3 TPD – CO_2 TPD) analysis of La(50)Cu(12.5)/Ni.np

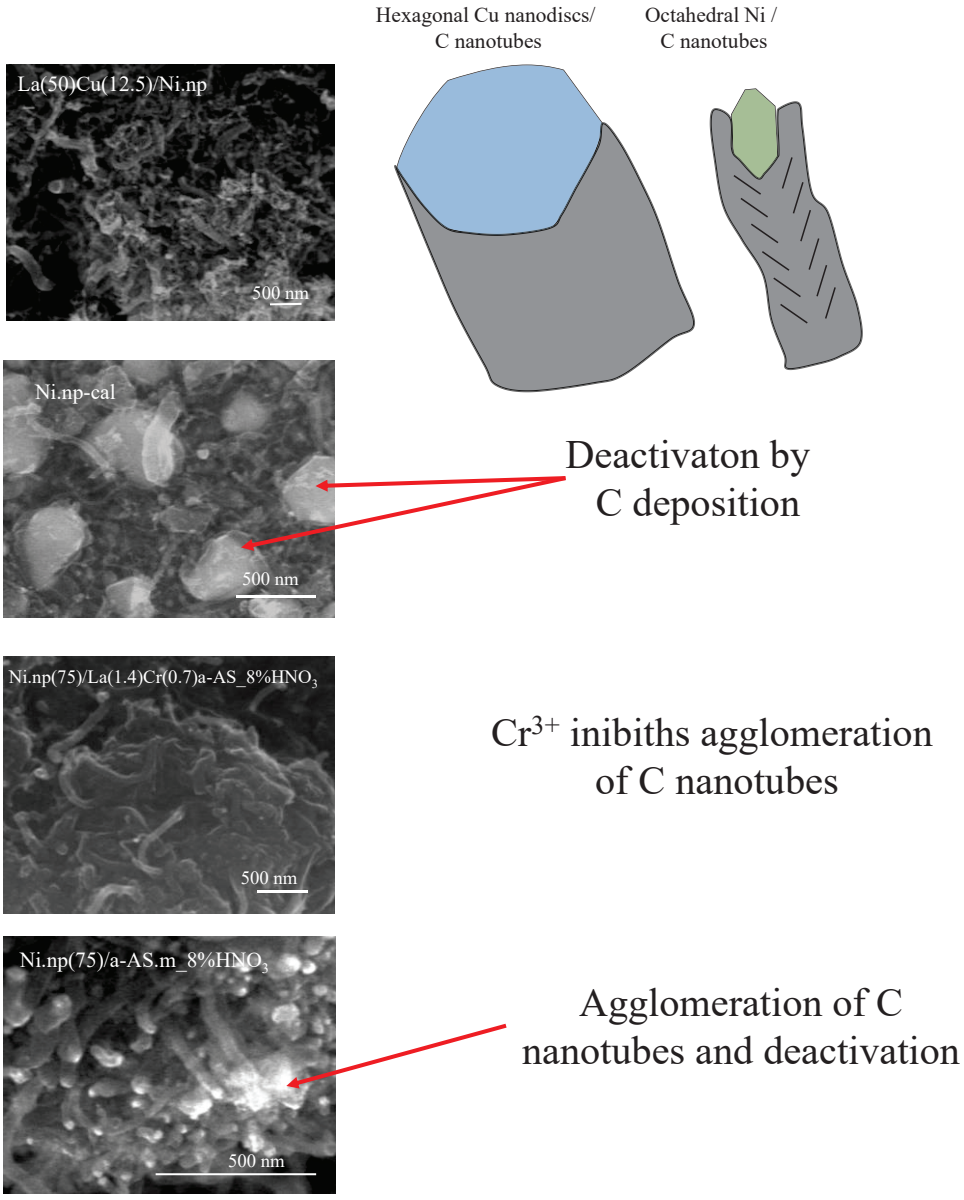

Image.

3.1 FE-SEM images of main samples after catalytic methane decomposition at severe conditions (m_{cat} =5.0 mg, 20.0 sccm CH_4/5 sccm Ar, 550.0 °C).

I further examined the catalyst at increased temperature of 700 °C and an outstanding conversion of methane of 50.8 % with H_2 yield of 15.9 % in severe conditions was observed.

3.4 Conclusions

I successfully synthesized a novel Ni-based catalyst through soft-template method, TRAP, with great implications in the future design of CDM catalysts. With this method, not only the support morphology and size of the support can be controlled, but also better understanding of the relation between support surface and crystallization of active species and promoters was achieved. This has great implications for the design of future supported catalysts since both the support and active catalytic species can be tailored to different applications.

In agreement with previous studies, lanthanum species improved Ni dispersion and C-H dissociation by electron transfer to nickel for both a-AS (above 7.4 % w/w) and Ni.np supports. Chromium on the other hand showed detrimental effects for CDM as a-AS promoter. La promoters showed synergistic effects with Cr, improving the formation of mesoporous in the catalyst and the fine crystallization of Ni nanoparticles throughout a-AS supports.

Porous Ni.np comprised of nanoplates of 23.2 nm in diameter and 8.4 nm in thickness were successfully synthesized using TRAPs, and further used as support for La and Cu promoters to improve their overall catalytic performance and stability. Max H_2 yield of 15.9 % and more than 400 min of generation at severe conditions (m_{cat} =5.0 mg, 20.0 sccm CH_4/5 sccm Ar, 550 °C)

Novel bi-metallic catalysts supported in Ni.np showed promising stability and conversion capabilities. Moreover, the TRAP method has unlimited potential to synthesize any type of metallic support from its nitrated form, enabling a wide range of supports for different combinations of catalysts and promoters.

Reference

[1] United Nations Environment Programme, Emissions Gap Report 2022: The Closing Window - Climate Crisis Calls for Rapid Transformation of Societies, 2022. https://wedocs.unep.org/20.500.11822/40874 (accessed September 21, 2023).

[2] M.K. Singla, P. Nijhawan, A.S. Oberoi, Hydrogen fuel and fuel cell technology for cleaner future: a review, Environmental Science and Pollution Research 28 (2021) 15607–15626. https://doi.org/10.1007/s11356-020-12231-8.

[3] M. Yue, H. Lambert, E. Pahon, R. Roche, S. Jemei, D. Hissel, Hydrogen energy systems: A critical review of technologies, applications, trends and challenges, Renewable and Sustainable Energy Reviews 146 (2021). https://doi.org/10.1016/j.rser.2021.111180.

[4] Menéndez-Agudin, R. Rocca, G. Fernandez, L. Luengo-Baranguan, D. Zaldivar, Hydrogen Technologies to Provide Flexibility to the Electric System: A Review, Renewable Energy and Power Quality Journal 20 (2022) 656–661. https://doi.org/10.24084/repqj20.392.

[5] H.F. Abbas, W.M.A. Wan Daud, Hydrogen production by methane decomposition: A review, Int J Hydrogen Energy 35 (2010) 1160–1190. https://doi.org/10.1016/j.ijhydene.2009.11.036.

[6] K. Tamura, D. Murata, T. Sumi, S. Kokuryo, H. Kitamura, S. Tsubota, K. Miyake, Y. Uchida, M. Miyamoto, N. Nishiyama, Dry Reforming of Methane with Suppressed Carbon Deposition over Cr- and Ni-Loaded Dealuminated β Zeolites, Energy & Fuels 37 (2023) 18945–18951. https://doi.org/10.1021/acs.energyfuels.3c02837.

[7] K.S. Nisa, V. Suendo, I.C. Sophiana, H. Susanto, A. Kusumaatmaja, N. Nishiyama, Y.W. Budhi, Effect of base promoter on activity of MCM-41-supported nickel catalyst for hydrogen production via dry reforming of methane, Int J Hydrogen Energy 47 (2022) 23201–23212. https://doi.org/10.1016/j.ijhydene.2022.05.081.

[8] I.C. Sophiana, F. Iskandar, H. Devianto, N. Nishiyama, Y.W. Budhi, Coke-Resistant Ni/CeZrO2 Catalysts for Dry Reforming of Methane to Produce Hydrogen-Rich Syngas, Nanomaterials 12 (2022) 1556. https://doi.org/10.3390/nano12091556.

[9] A. Al Nashrey, Comprehensive Overview of Hydrogen Production via Coal and Biomass Gasification Technologies, European Journal of Energy Research 2 (2022) 8–13. https://doi.org/10.24018/ejenergy.2022.2.4.85.

[10] S. Shiva Kumar, V. Himabindu, Hydrogen production by PEM water electrolysis – A review, Mater Sci Energy Technol 2 (2019) 442–454. https://doi.org/10.1016/j.mset.2019.03.002.

[11] J. Brauns, T. Turek, Alkaline Water Electrolysis Powered by Renewable Energy: A Review, Processes 8 (2020) 248. https://doi.org/10.3390/pr8020248.

[12] X. Tao, Y. Zhao, S. Wang, C. Li, R. Li, Recent advances and perspectives for solar-driven water splitting using particulate photocatalysts, Chem Soc Rev 51 (2022) 3561–3608. https://doi.org/10.1039/D1CS01182K.

[13] Y. Ma, L. Lin, T. Takata, T. Hisatomi, K. Domen, A perspective on two pathways of photocatalytic water splitting and their practical application systems, Physical Chemistry Chemical Physics 25 (2023) 6586–6601. https://doi.org/10.1039/D2CP05427B.

[14] E. Matus, O. Sukhova, I. Ismagilov, M. Kerzhentsev, O. Stonkus, Z. Ismagilov, Hydrogen Production through Autothermal Reforming of Ethanol: Enhancement of Ni Catalyst Performance via Promotion, Energies (Basel) 14 (2021) 5176. https://doi.org/10.3390/en14165176.

[15] N.S.N. Hasnan, S.N. Timmiati, K.L. Lim, Z. Yaakob, N.H.N. Kamaruddin, L.P. Teh, Recent developments in methane decomposition over heterogeneous catalysts: an overview, Mater Renew Sustain Energy 9 (2020). https://doi.org/10.1007/s40243-020-00167-5.

[16] K. Srilatha, D. Bhagawan, S. Shiva Kumar, V. Himabindu, Sustainable fuel production by thermocatalytic decomposition of methane – A review, S Afr J Chem Eng 24 (2017) 156–167. https://doi.org/10.1016/j.sajce.2017.10.002.

[17] F. Frusteri, G. Italiano, C. Espro, C. Cannilla, G. Bonura, H 2 production by methane decomposition: Catalytic and technological aspects, in: Int J Hydrogen Energy, 2012: pp. 16367–16374. https://doi.org/10.1016/j.ijhydene.2012.02.192.

[18] A.A. Ibrahim, A.H. Fakeeha, A.S. Al-Fatesh, A.E. Abasaeed, W.U. Khan, Methane decomposition over iron catalyst for hydrogen production, Int J Hydrogen Energy 40 (2015) 7593–7600. https://doi.org/10.1016/j.ijhydene.2014.10.058.

[19] N. Sánchez-Bastardo, R. Schlögl, H. Ruland, Methane Pyrolysis for CO2-Free H2 Production: A Green Process to Overcome Renewable Energies Unsteadiness, Chem Ing Tech 92 (2020) 1596–1609. https://doi.org/10.1002/cite.202000029.

[20] T. Maneerung, K. Hidajat, S. Kawi, Co-production of hydrogen and carbon nanofibers from catalytic decomposition of methane over LaNi(1-x)Mx O3-α perovskite (where M = Co, Fe and X = 0, 0.2, 0.5, 0.8, 1), Int J Hydrogen Energy 40 (2015) 13399–13411. https://doi.org/10.1016/j.ijhydene.2015.08.045.

[21] R. Guil-Lopez, J.A. Botas, J.L.G. Fierro, D.P. Serrano, Comparison of metal and carbon catalysts for hydrogen production by methane decomposition, Appl Catal A Gen 396 (2011) 40–51. https://doi.org/10.1016/j.apcata.2011.01.036.

[22] V. Nichele, M. Signoretto, F. Menegazzo, A. Gallo, V. Dal Santo, G. Cruciani, G. Cerrato, Glycerol steam reforming for hydrogen production: Design of Ni supported catalysts, Appl Catal B 111–112 (2012) 225–232. https://doi.org/10.1016/j.apcatb.2011.10.003.

[23] O. Phichairatanaphong, P. Teepakakorn, Y. Poo-Arporn, M. Chareonpanich, W. Donphai, Infiltrate Mesoporous Silica-Aluminosilicate Structure Improves Hydrogen Production via Methane Decomposition over a Nickel-Based Catalyst, Ind Eng Chem Res 60 (2021) 4562–4574. https://doi.org/10.1021/acs.iecr.0c06355.

[24] A.E. Awadallah, W. Ahmed, M.R.N. El-Din, A.A. Aboul-Enein, Novel aluminosilicate hollow sphere as a catalyst support for methane decomposition to COx-free hydrogen production, Appl Surf Sci 287 (2013) 415–422. https://doi.org/10.1016/j.apsusc.2013.09.173.

[25] A. Awad, M.A. Salam, D.V.N. Vo, B. Abdullah, Hydrogen production via thermocatalytic decomposition of methane over Ni-Cu-Pd/Al2O3 catalysts, in: IOP Conf Ser Mater Sci Eng, Institute of Physics Publishing, 2020. https://doi.org/10.1088/1757-899X/736/4/042006.

[26] Y. Uchida, T. Nishizawa, T. Omiya, Y. Hirota, N. Nishiyama, Nanosheet Formation in Hyperswollen Lyotropic Lamellar Phases, J Am Chem Soc 138 (2016) 1103–1105. https://doi.org/10.1021/jacs.5b11256.

[27] K. Sasaki, J.A.H. Gaitan, T. Okue, S. Matoba, Y. Tokuda, K. Miyake, Y. Uchida, N. Nishiyama, Amorphous Aluminosilicate Nanosheets as Universal Precursors for the Synthesis of Diverse Zeolite Nanosheets for Polymer-Cracking Reactions, Angewandte Chemie International Edition 61 (2022). https://doi.org/10.1002/anie.202213773.

[28] J.A. Hernandez G., K. Sasaki, K. Miyake, Y. Uchida, N. Nishiyama, Control of composition and surface area of aluminosilicates by tuning base catalyst concentration, Chem Lett In press (2024).

[29] S. Kokuryo, K. Tamura, K. Miyake, Y. Uchida, M. Miyamoto, Y. Oumi, A. Mizusawa, T. Kubo, N. Nishiyama, High coke deposition resistance by Cr loading on zeolite defects: reduced regeneration in cracking reactions, Catal Sci Technol 12 (2022) 7270–7274. https://doi.org/10.1039/D2CY00506A.

[30] A.E. Awadallah, A.A. Aboul-Enein, A.K. Aboul-Gheit, Impact of group VI metals addition to Co/MgO catalyst for non-oxidative decomposition of methane into COx-free hydrogen and carbon nanotubes, Fuel 129 (2014) 27–36. https://doi.org/10.1016/j.fuel.2014.03.038.

[31] A. Rastegarpanah, M. Rezaei, F. Meshkani, K. Zhang, X. Zhao, W. Pei, Y. Liu, J. Deng, H. Arandiyan, H. Dai, Influence of group VIB metals on activity of the Ni/MgO catalysts for methane decomposition, Appl Catal B 248 (2019) 515–525. https://doi.org/10.1016/j.apcatb.2019.01.067.

[32] J.L. Figueiredo, J.J.M. Órfão, A.F. Cunha, Hydrogen production via methane decomposition on Raney-type catalysts, Int J Hydrogen Energy 35 (2010) 9795–9800. https://doi.org/10.1016/j.ijhydene.2009.12.071.

[33] M. Pudukudy, Z. Yaakob, Methane decomposition over Ni, Co and Fe based monometallic catalysts supported on sol gel derived SiO2 microflakes, Chemical Engineering Journal 262 (2015) 1009–1021. https://doi.org/10.1016/j.cej.2014.10.077.

[34] G. Urdiana, R. Valdez, G. Lastra, M.Á. Valenzuela, A. Olivas, Production of hydrogen and carbon nanomaterials using transition metal catalysts through methane decomposition, Mater Lett 217 (2018) 9–12. https://doi.org/10.1016/j.matlet.2018.01.033.

[35] A.F. Cunha, N. Mahata, J.J.M. Órfão, J.L. Figueiredo, Methane Decomposition on La $_2$ O $_3$ -Promoted Raney-Type Fe Catalysts, Energy & Fuels 23 (2009) 4047–4050. https://doi.org/10.1021/ef900385e.

[36] H. Kitamura, T. Sumi, S. Kubota, S. Kokuryo, K. Tamura, K. Miyake, Y. Uchida, M. Miyamoto, N. Nishiyama, Stable and selective conversion of ethylene to propylene and butylene using Ni-loaded dealuminated Beta zeolite catalyst, Appl Catal A Gen 668 (2023) 119429. https://doi.org/10.1016/j.apcata.2023.119429.

[37] A.E. Awadallah, D.S. El-Desouki, N.A.K. Aboul-Gheit, A.H. Ibrahim, A.K. Aboul-Gheit, Effect of crystalline structure and pore geometry of silica based supported materials on the catalytic behavior of metallic nickel particles during methane decomposition to CO -free hydrogen and carbon nanomaterials, Int J Hydrogen Energy 41 (2016) 16890–16902. https://doi.org/10.1016/j.ijhydene.2016.07.081.

[38] Söderlund, T., Alakoskela, J.-M. I., Pakkanen, A. L., & Kinnunen, P. K. J. (2003). Comparison of the Effects of Surface Tension and Osmotic Pressure on the Interfacial Hydration of a Fluid Phospholipid Bilayer. Biophysical Journal, 85(4), 2333–2341. https://doi.org/10.1016/S0006-3495(03)74657-8

[39] Nakada, M., Kanda, J., Uchiyama, H., & Matsumura, K. (2024). Nanoscale intracellular ultrastructures affected by osmotic pressure using small-angle X-ray scattering. Biophysical Chemistry, 312, 107287. https://doi.org/10.1016/j.bpc.2024.107287

[40] Davidson, P., Penisson, C., Constantin, D., & Gabriel, J.-C. P. (2018). Isotropic, nematic, and lamellar phases in colloidal suspensions of nanosheets. Proceedings of the National Academy of Sciences, 115(26), 6662–6667. https://doi.org/10.1073/pnas.1802692115

[41] F. Ntuli, A.E. Lewis, The influence of iron on the precipitation behaviour of nickel powder, Chem Eng Sci 62 (2007) 3756–3766. https://doi.org/10.1016/j.ces.2007.04.001.

[42] Y. Fujimoto, T. Sumi, K. Miyake, Y. Uchida, N. Nishiyama, Improving Coke Resistance of Zn Ion Exchanged ZSM-5 on Dehydroaromatization of Ethane by Cr Species Loading, Chem Lett 51 (2022) 515–517. https://doi.org/10.1246/cl.210765.

[43] M. Pudukudy, Z. Yaakob, M.S. Takriff, Methane decomposition into COx free hydrogen and multiwalled carbon nanotubes over ceria, zirconia and lanthana supported nickel catalysts prepared via a facile solid state citrate fusion method, Energy Convers Manag 126 (2016) 302–315. https://doi.org/10.1016/j.enconman.2016.08.006.

[44] D. Huang, H. Liu, T. Li, Q. Niu, Template-free synthesis of NiO skeleton crystal octahedron and effect of surface depression on electrochemical performance, J Solgel Sci Technol 89 (2019) 511–520. https://doi.org/10.1007/s10971-018-4908-3.

[45] R.J. Kokes, P.H. Emmett, Chemisorption of Nitrogen on Nickel Catalysts, J Am Chem Soc 80 (1958) 2082–2086. https://doi.org/10.1021/ja01542a015.

[46] D. Wang, R. Xu, X. Wang, Y. Li, NiO nanorings and their unexpected catalytic property for CO oxidation, Nanotechnology 17 (2006) 979–983. https://doi.org/10.1088/0957-4484/17/4/023.

[47] H. Li, H. Zhang, M. Luo, Y. Dong, H. Xu, X. Cheng, Z. Cai, Adsorption of vanadium with amorphous hydrated chromium oxide, Water Pract Technol 16 (2021) 1410–1420. https://doi.org/10.2166/wpt.2021.078.

[48] D. Caputo, M. Casiello, A. Milella, W. Oberhauser, A. Maffezzoli, A. Nacci, C. Fusco, L. D'Accolti, Deep Control of Linear Oligomerization of Glycerol Using Lanthanum Catalyst on Mesoporous Silica Gel, Catalysts 10 (2020) 1170. https://doi.org/10.3390/catal10101170.

[49] T. Schaller, J.F. Stebbins, The Structural Role of Lanthanum and Yttrium in Aluminosilicate Glasses: A ^{27} Al and ^{17} O MAS NMR Study, J Phys Chem B 102 (1998) 10690–10697. https://doi.org/10.1021/jp982387m.

[50] D. Rivero-Mendoza, J. Stanley, J. Scott, K.-F. Aguey-Zinsou, An Alumina-Supported Ni-La-Based Catalyst for Producing Synthetic Natural Gas, Catalysts 6 (2016) 170. https://doi.org/10.3390/catal6110170.

[51] F. Ayari, M. Mhamdi, D.P. Debecker, E.M. Gaigneaux, J. Alvarez-Rodriguez, A. Guerrero-Ruiz, G. Delahay, A. Ghorbel, Effect of the chromium precursor nature on the physicochemical and catalytic properties of Cr–ZSM-5 catalysts: Application to the ammoxidation of ethylene, J Mol Catal A Chem 339 (2011) 8–16. https://doi.org/10.1016/j.molcata.2011.02.012.

[52] G. Tang, D. Gong, H. Liu, L. Wang, Highly Loaded Mesoporous Ni–La2O3 Catalyst Prepared by Colloidal Solution Combustion Method for CO2 Methanation, Catalysts 9 (2019) 442. https://doi.org/10.3390/catal9050442.

[53] Z. Xie, Y. Ren, J. Li, Z. Zhao, X. Fan, B. Liu, W. Song, L. Kong, X. Xiao, J. Liu, G. Jiang, Facile in situ synthesis of highly dispersed chromium oxide incorporated into mesoporous ZrO2 for the dehydrogenation of propane with CO2, J Catal 372 (2019) 206–216. https://doi.org/10.1016/j.jcat.2019.02.026.

[54] T. Zhu, H. Song, F. Li, Y. Chen, Hydrodeoxygenation of Benzofuran over Bimetallic Ni-Cu/γ-Al2O3 Catalysts, Catalysts 10 (2020) 274. https://doi.org/10.3390/catal10030274.

[55] K.N. Papageridis, N.D. Charisiou, S. Douvartzides, V. Sebastian, S.J. Hinder, M.A. Baker, A.A. AlKhoori, S.I. AlKhoori, K. Polychronopoulou, M.A. Goula, Continuous selective deoxygenation of palm oil for renewable diesel production over Ni catalysts supported on Al_2O_3 and La_2O_3–Al_2O_3, RSC Adv 11 (2021) 8569–8584. https://doi.org/10.1039/D0RA08541C.

[56] T.A. Le, T.W. Kim, S.H. Lee, E.D. Park, CO and CO2 methanation over Ni catalysts supported on alumina with different crystalline phases, Korean Journal of Chemical Engineering 34 (2017) 3085–3091. https://doi.org/10.1007/s11814-017-0257-0.

[57] W.-X. Zhang, Y. Liang, J.-W. Luo, A.-P. Jia, Y.-J. Wang, J.-Q. Lu, M.-F. Luo, Morphological effects of ordered Cr2O3 nanorods and Cr2O3 nanoparticles on fluorination of 2-chloro-1,1,1-trifluoroethane, J Mater Sci 51 (2016) 6488–6496. https://doi.org/10.1007/s10853-016-9948-x.

[58] J. Dufour, C. Martos, A. Ruiz, M. Maroño, J.M. Sánchez, Synthesis of copper promoted high temperature water–gas shift catalysts by oxidation–precipitation, Int J Hydrogen Energy 39 (2014) 17600–17607. https://doi.org/10.1016/j.ijhydene.2014.08.120.

[59] Meyer, Mbese, Agoro, The Frontiers of Nanomaterials (SnS, PbS and CuS) for Dye-Sensitized Solar Cell Applications: An Exciting New Infrared Material, Molecules 24 (2019) 4223. https://doi.org/10.3390/molecules24234223.

[60] J. Liu, G. Wang, L. Lu, Y. Guo, L. Yang, Facile shape-controlled synthesis of lanthanum oxide with different hierarchical micro/nanostructures for antibacterial activity based on phosphate removal, RSC Adv 7 (2017) 40965–40972. https://doi.org/10.1039/C7RA07521A.

Chapter 4

Zeolite Applications: Catalytic Transalkylation of Alkylphenol to Phenol in Supercritical Benzene Over MFI-type Zeolite in a Fixed-bed Reactor

4.1 Introduction

The manufacturing of natural biopolymers (15.0 – 30.0% dry weight of total lignocellulosic biomass) is a vision that many scientists share to take advantage, not only from raw natural resources, but also to better utilize the lignin from waste woody sources (around 40.0 – 50.0 million tons per annum are produced worldwide as a mostly non-commercialized waste product) and convert it into numerous useful products such as polymers, chemicals and fuels for industrial uses.[1–4]

Lignin is a very attractive biopolymer due to its high phenolic molecular mass which can be used as a feedstock for aromatic compounds and, up to date, lignin has no competing applications. Available lignin and market value of phenols obtained from petroleum and coal sources will likely increase, resulting in an increased attention to research and use of lignin as a source of platforms chemicals and phenol production.[5]
Lignin extraction from biomass is no longer a barrier in the race for valorization of lignin. Currently there are four main industrial processes to produce high-purity lignin; the Sulfite, Soda, Kraft, and Organosolv.[6] After lignin is extracted, there are four main upstream processes to depolymerize it; oxidative depolymerization,[7–13] thermal depolymerization,[14–20] chemical modification[21–24] and reductive depolymerization.[25–30] In my laboratory, Organosolv process is mainly used to extract high purity lignin and reductive depolymerization upstream processes.[13,30]

The main reactions involved in reductive depolymerization are hydrogenolysis, hydrocracking, hydrogenation, and hydrodeoxygenation (HDO) to break down lignin into phenolic compounds of lower molecular weight.[31–35]

The primary products obtained by the reductive depolymerization method are alkoxyphenols, benzene polyols, phenol, and catechol.[4] Direct production of alkyl phenols from lignin have been reported, but generally, the yields are low or de-methoxylation downstream processes are required. In 2020, Li et. al. proposed a one-pot lignin conversion where native lignin was converted into 4-alkylphenols via self-reforming-driven depolymerization and hydrogenolysis over $Pt/NiAl_2O_4$, with high yields up to 17.3 wt.% with subsequent aqueous phase reforming, accelerating the process and providing a low-cost and safe way for lignin valorization.[36] Hendry et.al. also reported alkylphenol production, 9.5 wt.%, from Etek lignin waste by ex-situ catalytic pyrolysis using Na/ZrO_2 and mild basicity conditions. [37]

To improve the amount of alkylphenols and phenols obtained from reductive catalytic processes from lignin, a de-methylation or de-methoxylation step is required to eliminate side chain methyl groups in the form of volatile CH_4 or CH_3OH.[38–41] For the scope of this study, I focused on the downstream process of the transalkylation of those alkylphenols to phenols using 4-propylphenol (ppp) molecules as alkylphenols model compound. Previous studies had reported successful de-methoxylation of alkoxyphenols of thermal degraded lignin and 2-methoxyphenol over FeO_x-based catalyst.[13,42]

Zeolite catalyst have been proved to remove the alkyl substituent from 4-ethylphpenol and 4-propylphenol into phenol and the associated olefins [44, 45, 46]. Additionally, it has been proved that MFI type zeolites had the better performance (yield and selectivity) towards phenol production in the transalkylation reaction of ppp [47] due to its shape selectivity properties as compared with mordenite and beta. Consequently, MFI type zeolite was chosen for this study.
Understanding the kinetic and diffusion limitations of this reaction over MFI-type zeolites is key for scaling up to an industrial process. In this work, the kinetics for the continuous transalkylation reaction of ppp and benzene over MFI-type zeolites in a fixed bed reactor in supercritical fluid was evaluated.

Previous reports indicate that supercritical fluid suppressed coke formation significantly in the zeolite's pores, which causes the pore channels to narrow and eventually be plugged, extending the lifespan of the zeolite as a catalyst [47, 48,49]. For this reason, I also studied the effect of the crystal size and acid sites (Al content) on the kinetics of the reaction and the ideal operating conditions in the supercritical region were established.

4.2 Experimental

4.2.1 Supercritical Fixed Bed Reactor and Kinetics

H–MFI–type zeolite selective catalytic properties were studied in the continuous transalkylation of ppp and benzene using a homemade fixed bed reactor. 150 mg of zeolite were calcined at 823 K under air flow for 2.00 h and placed in the reactor. A solution of 10.0 % 4–propylphenol (mass ppp/mass benzene) was made for all the reactions and injected into the stream using a piston system, pushed by distilled water. The system, seen in **Figure 4.1**, was heated, and pressurized using pure benzene. Once the desired pressure and temperature were reached, the feedstock was injected and stabilized before taking the samples.

The selected temperatures for the kinetic analysis were 350, 375 and 400 °C, with different time factors W/F_{ppp} ranged from 13.8 to 82.6 kg mol^{-1} s, where W is the catalytic weight and F_{PPP} is the feed rate of ppp (0.90 – 5.42 cm^3 h^{-1}).

The critical temperature of benzene and ppp are 562 and 715 K respectively, and the critical pressure are 4.89 and 3.60 MPa respectively [55]. The operating pressure range was 11.0 – 11.2 MPa for all reactions, consequently, the solution is in supercritical phase. The composition of the obtained liquid was analyzed by gas chromatography (GC2014, Shimadzu Co., Ltd.) equipped with FID detectors.

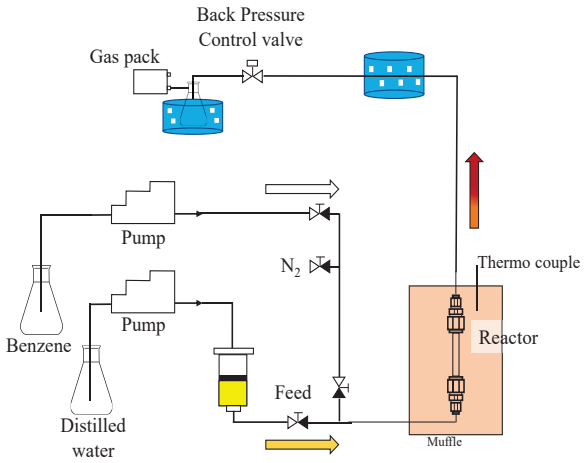

Figure. 4.1 Experimental setup for the transalkylation of ppp and supercritical benzene.

4.2.2 MFI-type Zeolite Samples

As previously discussed in Chapter 2, MFI-type zeolites samples were synthesized using the emulsion method, with a mixture of Water/O-15 surfactant/Cyclohexane. The water phase consisted of tetra-*n*-propyl ammonium hydroxide solution (abt. 10.0%) [TPA-OH; an organic structure directing agent (OSDA)], aluminum triisopropoxide (AIP), and sodium chloride (NaCl). Experimental samples are summarized in Chapter 2, **Table 2.3.**

Micro and nano MFI-type zeolites were successfully synthesized and verified by XRD analysis (**Figure 2.8a**), when compared to the calculated powder diffraction pattern for MFI-type zeolite from the database of zeolite structure (International Zeolite Association), as well as good crystallinity of the samples. Approximate crystal size was determined by imaging of the samples using SEM and FE–SEM as seen **in Figure 2.8b**, ranging from 100 – 2.00 x 10^3 nm.

4.3 Results and Discussion

4.3.1 Continuous Transalkylation of 4–propylphenol and Benzene in a Fixed Bed Reactor in Supercritical Fluid

I evaluated the kinetics of the transalkylation of ppp and benzene over nanometer – and micrometer–sized H–MFI–type zeolite using a continuous fixed bed reactor in supercritical fluid. The product yield was calculated based on the carbon amount of the ppp feedstock and the obtained products showed that transalkylation, isomerization, disproportionation, and dealkylation reactions took place during the reaction.

The main reaction pathways in the experimental reaction were the transalkylation reaction of ppp and benzene resulting in phenol (main product) and C–3 benzenes (propyl benzene and cumene) production and the isomerization reactions resulting in 2-isopropylphenol, 2-propylphenol and 3-propylphenol, as seen in **Figure 4.3**.

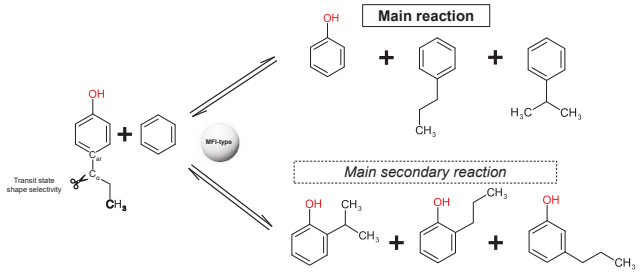

Figure. 4.3 Transalkylation reaction of ppp and benzene and main side reaction (isomerization reaction) over MFI-type zeolite catalyst.

These results are in agreement with MFI–type zeolite transition state shape selectivity with high preference towards the cleavage of C_{ar}–C_{α}, even when C_{α}– C_{β} has lower bond energy, 385 and 301 kJ mol–1, respectively, [45] as seen in the products yields of **Figure. 4.3** and **Figure. 4.4**.

Other reaction pathways were also observed in smaller quantities. Cleavage C_{α}–C_{β} and C_{β}–C_{γ} (ethylphenol–ethylbenzene and cresol–toluene) and disproportionation reactions (di–aromatics and methylated compounds) were produced in small quantities (less than 0.8 C–mol % yield average for the micrometer- and nanometer–sized particles). Special attention was given to the isomerization reactions since they accounted up to 17.4 C–mol % yield (nanometer-sized particles, 623 K and W/F_{ppp} = 27.6 kg s mol^{-1}) of the reacted ppp, and in average they accounted for 38.0 and 47.8 % of all the undesired reactions for the micrometer– and nanometer– sized particles, respectively. The coke and other unidentified products yield are included in the undesired reactions along with the known undesired reactions for the micrometer– and nanometer–sized zeolite evaluated points.

When analyzing the isomerization reactions, a curious behavior is observed, an inverse correlation on the yield of isomers is observed for nanometer sized particles, when decreasing temperature and decreasing W/F_{PPP}, while the micrometer particles follow a direct correlation.

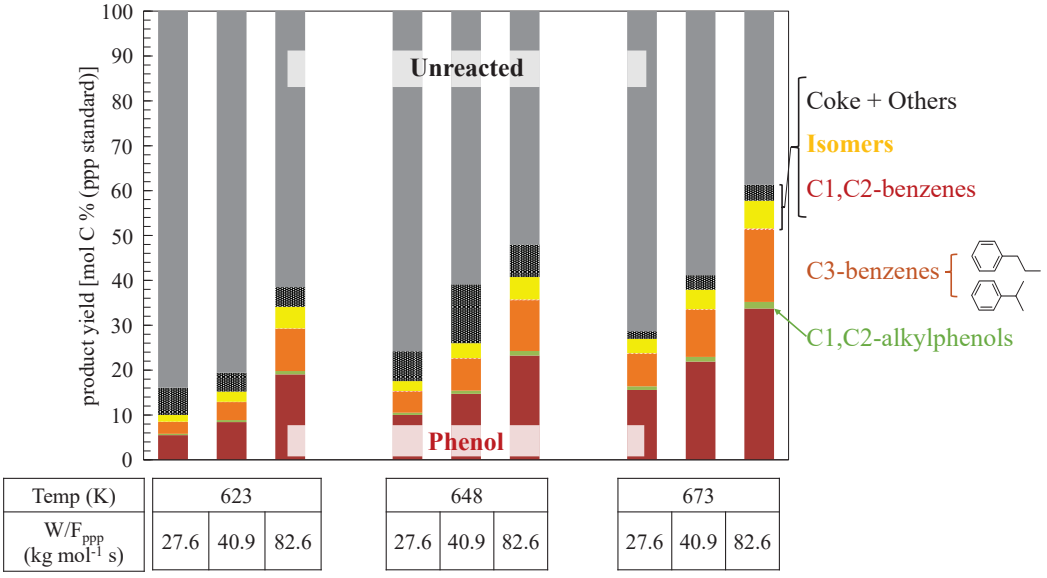

Figure. 4.3 Yield [C–mol %] of transalkylation and undesired products for the micrometer sized MFI-type zeolite. *Reaction conditions: 10 wt% ppp, MFI (nanometer– and micrometer– size) catalyst. Product yields are based on ppp, benzene was added in excess. P = 11.0 – 11.2 MPa.

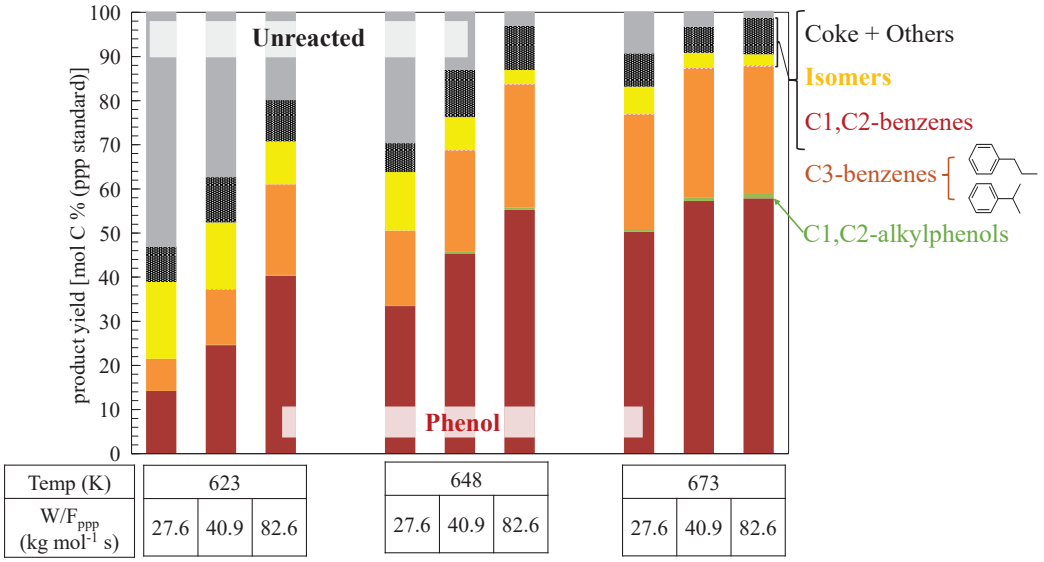

Figure. 4.4 Yield [C–mol %] of transalkylation and undesired products for the nanometer sized MFI-type zeolite*Reaction conditions: 10 wt% ppp, MFI (nanometer– and micrometer– size) catalyst. Product yields are based on ppp, benzene was added in excess. P = 11.0 – 11.2 MPa.

Liao. et. al., calculated the free Gibbs energies for the dealkylation of 4-ethylphenol (4-EP) and observed that the free energies for isomerization and disproportionation of 4-EP where almost constant (close to zero) over the temperature range of 473 – 773 K concluding that these two reactions were favored at low temperatures compared to the dealkylation which was favored at high temperatures. [46]

This similar behavior was observed for the transalkylation of ppp with benzene (which also starts with a dealkylation of the C_{ar}–C_{α} bond) and the isomerization reactions in the temperature range of 623 – 673 K, as seen **Figure. 4.4**. In the case of micrometer sample, low surface provides less available acid sites, and the isomer generation depends on the steric factor of reactive collisions. Hence higher temperatures and low-speed flows, nonetheless, remain relatively constant.

The effect of temperature and time factor was analyzed for the supercritical transalkylation of ppp–benzene in a fixed bed reactor using H–MFI type zeolite. **Figure. 4.5** shows the ideal conditions to maximize the conversion of ppp with high selectivity towards phenol production. For the micrometer– size zeolite, conversion is lower than 60 % at all points of temperature and time factors, ruled by the 40.0 – 50.0 % range. For the nanometer-size particles, a wide range of conversions can be obtained at the different points.

Micrometer- size particles selectivity showed a maximum of 81.4 % at 673 K and 82.7 kg mol^{-1} s, but several combinations of temperature and time factors can be used to obtain 65.0 – 75.0 % selectivity at 40.0 – 50.0 % conversion. For the nanometer– size zeolite, the highest conversion obtained was 98.4 % with a selectivity of 88.1% at 673 K and 82.7 kg mol^{-1} s.

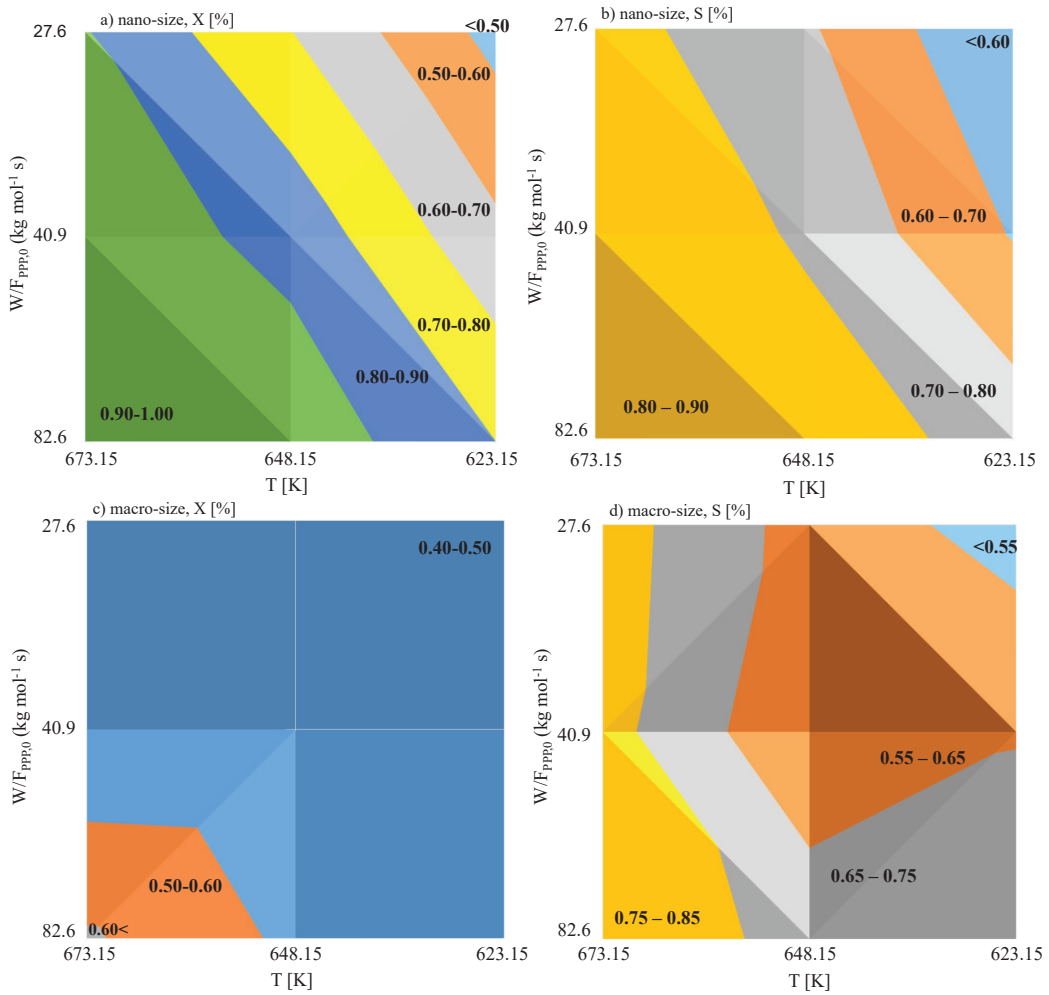

Figure. 4.5 Phenol conversion (a) and (c) and selectivity (b) and (d) [%] for nanometer– and micrometer–size MFI–type zeolite in supercritical fluid.

Figure. 4.6 shows the effect of particle size on the composition of the outlet stream [C–mol % (based on ppp)] at a time factor of 82.6 kg mol^{-1}s, vs different temperature points. A clear difference on the phenol yield was observed between the nanometer– and micrometer– sized H–MFI–type zeolite (for all the analyzed points, the average yield increase was 25.2 C–mol % when using nanometer–sized particles) indicating the presence of intracrystalline diffusion limitations for the micrometer-sized particles.

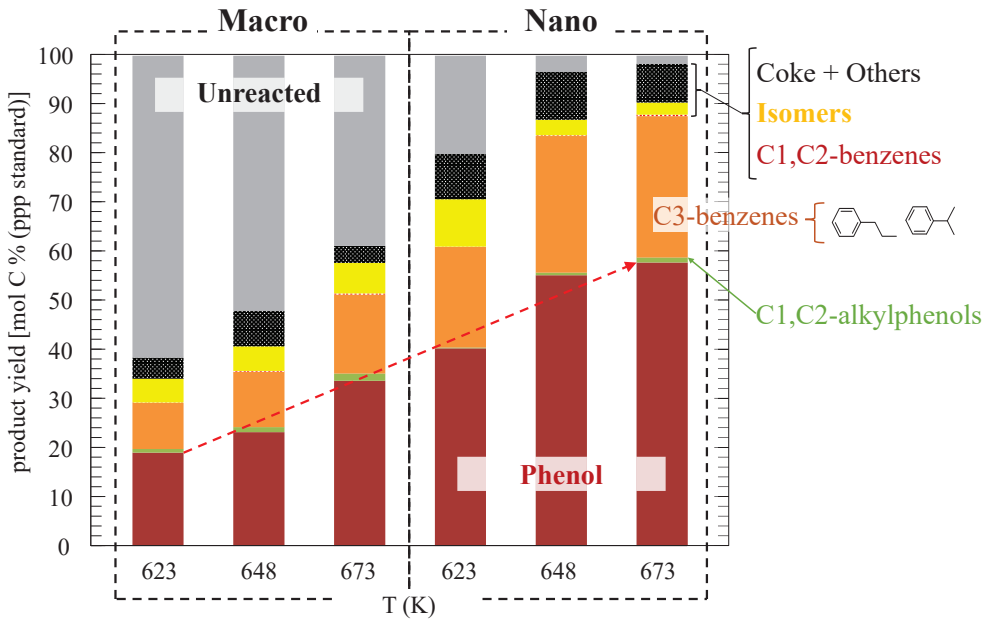

Figure. 4.6 Effect of crystal size on the yield [C–mol %] of transalkylation and undesired products

*Reaction conditions: 10 wt% ppp, MFI (nanometer– and micrometer– size) catalyst, T = 350, 375 and 400 °C, P = 11.0 – 11.2 MPa, W/F_{PPP} = 82.7 kg mol^{-1} s. Product yields are based on ppp, benzene was added in excess.

Catalyst stability was evaluated for the sample (N.1) in two cycles of 60 minutes with the following conditions: T = 673 K, P = 11.0 – 11.2 MPa and W/F_{PPP} = 40.9 kg mol^{-1}s. A steady conversion of ppp and negligible change in phenol and isomers yield was established. ppp conversion was 94.88 and 93.91 C-mol%, and phenol yield was 60.21 and 59.85 C-mol % for the 1st and the 2nd cycle, respectively. Hence, I was able to conclude that the catalyst was effectively stable in the analyzed timeframe (120 min total), successfully suppressing coke formation in supercritical conditions and in agreement with previous reports. [47, 48]

4.3.2 Kinetics of Transalkylation of ppp and Benzene

A first evaluation of the increment of phenol concentration vs. the increase in reactants suggested a 1st order reaction kinetics, consequently, a 1st order kinetic model was developed assuming a parallel bimolecular reaction based on the consumption of ppp to form phenol and isomers molecules. Benzene was added in excess to simplify the kinetic model. The concentration of benzene can be expressed as follow:

$$C_B = C_{B,0}(1 - X_B), \quad X_B \approx 0$$

$$C_B = C_{B,0} \tag{1}$$

The reaction rate for the transalkylation and isomerization reactions can be expressed with the following equation.

[Transalkylation]

$$-r_{TRA} = k'_1 C_{PPP} \tag{2}$$

[Isomerization]

$$-r_{ISO} = k'_2 C_{PPP} \tag{3}$$

where r_{TRA} and r_{ISO} represent the specific rate of reaction (mol kg^{-1} s^{-1}) of transalkylation of ppp/benzene and isomerization of ppp, respectively. C_{PPP} represents the concentration of ppp (mol m^{-3}), t represents reaction time (s), k'1 represents the specific rate constant of transalkylation (m^3 kg^{-1} s^{-1}) and k2 represents the specific rate constant of isomerization (m^3 kg^{-1} s^{-1}).

From Eqs. (2) and (3), the consumption rate of ppp in the overall conversion is expressed as:

$$-r_{PPP} = -(k'_1 + k'_2)C_{PPP} \tag{4}$$

Eq. (5) is obtained by integration of Eq. (4),

$$\frac{W}{F_{PPP}} = \frac{1}{(k\prime_1 + k\prime_2)} \frac{-\ln(\frac{C_{PPP}}{C_{PPP,0}})}{C_{PPP,0}} \tag{5}$$

where, W is the catalyst weight (kg), FPPP is the feed rate (mol s^{-1}), $C_{PPP,0}$ is the initial concentration of ppp (mol m^{-3}) [48].

In addition, Eq. (6) was obtained from Eqs. (2) and (4).

$$\frac{C_{PPP,0} - C_{PPP}}{C_{PH} - C_{PH,0}} = \frac{(k\prime_1 + k\prime_2)}{k\prime_1} \tag{6}$$

where $C_{PH,0}$ and C_{PH} are the initial and final concentration of phenol (mol/m^3) for the transalkylation process.

Figure. 4.7 shows the relationship between the $(\ln(C_{PPP,0}/C_{PPP})/ C_{PPP,0})/((C_{PPP,0}–C_{PPP})/C_{PH})$ and W/F_{PPP} obtained at different temperatures for the nanometer– and micrometer–sized H–MFI–type zeolite. The slope of the plots in these figures represent the apparent reaction rate constant k'_1 (m^{-3} kg s) for the transalkylation reaction. The reaction rate constants over micrometer– H–MFI–type zeolite ($k'_{1,macro}$) were 1.68 x 10^{-5}, 1.02 x 10^{-6}, and 7.50 x 10^{-6} s^{-1}, for the 350, 375 and 400 °C points, respectively. For the nanometer–sized H–MFI–type zeolite ($k'_{1,nano}$) were 9.36 x 10^{-5}, 4.45 x 10^{-5}, and 2.49 x 10^{-5} s^{-1}, for the 350, 375 and 400 °C points, respectively.

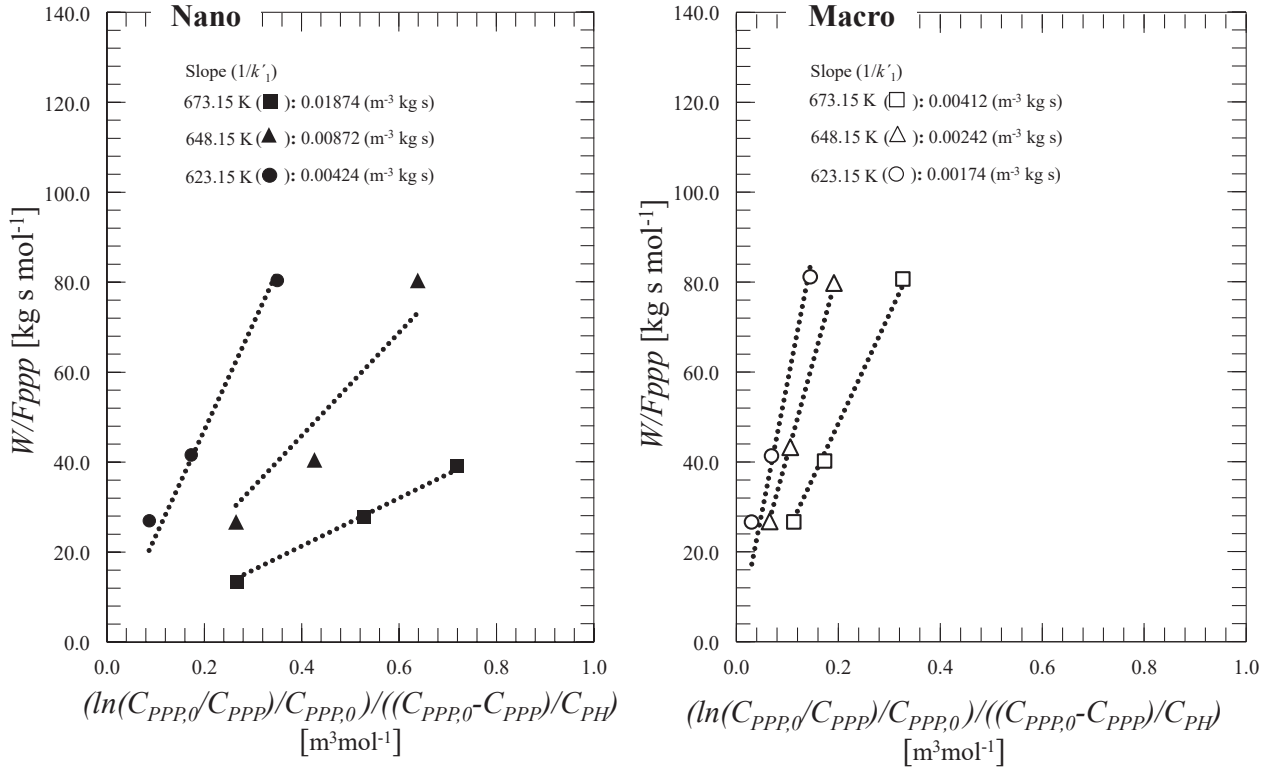

Figure. 4.7 Specific constant rates of transalkylation over nanometer– and micrometer– sized H–MFI– zeolite. *Reaction conditions T = 673 - 623 K, P = 11.0 – 11.2 MPa, W/F_{PPP} = 13.8 - 82.7 kg mol^{-1}s. Product yields are based on ppp, benzene was added in excess.

Figure. 4.8 shows the Arrhenius plots of the rate constants of transalkylation of ppp/benzene and isomerization of ppp over nanometer- and micrometer–sized H–MFI–type zeolite. The activation energies for the transalkylation were 103 and 60.0 kJ mol–1 for the nanometer- and micrometer– sized zeolite, respectively, and for the isomerization reaction were 31.5 and 34.6 $kJmol^{-1}$ for the nanometer– and micrometer– size, respectively.

As expected, for the isomerization reactions the activation energies for both nanometer and micrometer were almost the same as seen in Fig. 9, indicating that this reaction mostly take place in the outer surface of the zeolite where there are no intracrystalline diffusion limitations and there is no transit state shape selectivity.

For the synthesized nanometer sample, the external surface is 5 times bigger than the micrometer particle sized, resulting in a higher activity of isomerization reactions. Nonetheless, the highest isomer generation was observed at low temperatures and high-speed flows.

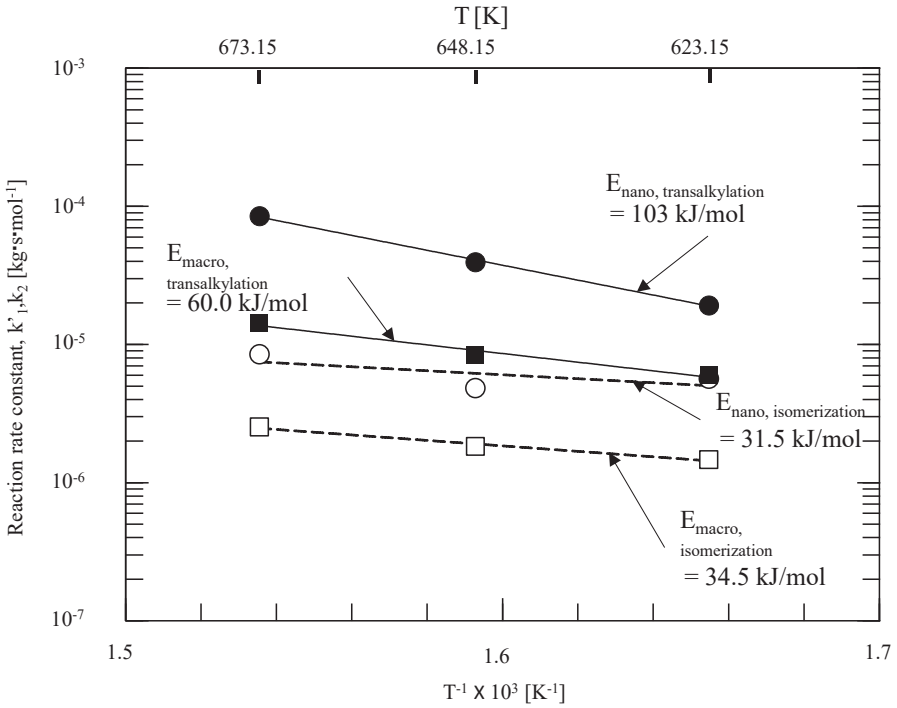

Figure. 4.8 Activation energies for transalkylation and isomerization reactions over nanometer- and micrometer- size H-MFI- type zeolite. *Reaction conditions T = 623 - 673 K, P = 11.0 – 11.2 MPa, W/F_{PPP} = 13.8 - 82.7 kg mol^{-1} s. Product yields are based on ppp, benzene was added in excess.

Transalkylation activation energies agree with Liao. et al. Since both the reaction rate and diffusional process are temperature dependent, diffusion limitations are observed as the activation energy in the micrometer– size is smaller than the nanometer– size particles and in agreement with equation; [57].

$$E_{obs} = (E_{true} + E_{diff})/2 \quad (7)$$

Next, I calculated the Thiele modulus and effectiveness factor for the transalkylation of ppp and supercritical benzene over MFI–type zeolite with different crystal sizes and Si/Al ratios. Diffusion limitations of molecules in the zeolite pores on the reaction in supercritical fluid, Thiele modulus vs. effectiveness factor graph was prepared. For this analysis, samples N.1 and M.1 with similar Si/Al ratios were selected. Decreasing the particle size (2.00 x 10^3 to 100 nm), decreases the Thiele modulus number and hence increases the efficiency factor. The relationship between the Thiele modulus,ϕ, and effectiveness factor, η, was used according to the following equations.

$$\phi = \frac{\mathrm{V}}{S}\sqrt{\frac{k\times\rho_p}{D_{eff}}} = L\sqrt{\frac{k\times\rho_p}{D_{eff}}}, \qquad (8)$$

$$V = \frac{1}{2}\,S\,\times 2L\ in\ a\ slab - shape\ crystal$$

where V is the volume of the zeolite crystal, S is the external surface area of the zeolite crystal, L is the half–thickness value of the MFI–type zeolite crystal and ϱP is the density of the zeolite crystal.

And the effectiveness factor was expressed in terms of the Thiele modulus as [54]:

$$\eta = \frac{\tanh(\phi)}{\phi} \qquad (9)$$

In the regime of strong diffusion resistance this relationship can be expressed as:

$$\frac{-r_{T1}}{-r_{T2}} = \frac{\eta_1}{\eta_2} = \frac{\phi_1}{\phi_2} = \frac{L_2}{L_1} \qquad (10)$$

Figure. 4.9 shows the ranges for the different limiting process to decrease diffusional resistances due to temperature dependence [57]. As temperature increases, Thiele modulus increases, indicating that the increase in reaction rate is faster than the decrease in diffusion resistance in supercritical fluid [58]. The effectiveness factors for the nanometer-and micrometer- size particles at 350 °C were 0.990 and 0.410, indicating that the catalytic transalkylation reaction over micrometer- size zeolite proceeded under transition conditions whilst the nanometer- size zeolite proceeded under reaction-controlling conditions. The same behavior was observed for the 375 °C temperature points and for the 400 °C temperature point, the reaction using nanometer- size particles shift into the transition condition.

Different acid site amounts were also evaluated in the kinetics of the transalkylation of ppp and benzene at 623 K, for the nanometer– size particles. As seen in **Table. 4.2**, the reaction rate constant for the transalkylation (k'1) increased with increasing acid site amount of zeolite, while isomerization reaction rate (k'2) change was negligible. This suggests that transalkylation reaction take place inside the pores of the zeolite, in accordance with previous reports [48], allowing both, Brønsted and Lewis acid sites, to dealkylate the alkyl group of the ppp molecule [44, 45, 46] limiting the reaction pathway due to the transit state shape selectivity of the MFI-type zeolite.

Table. 4.2 Rate constant for transalkylation and isomerization reactions for different Si/Al ratios at 623 K

Sample	Particle Size (nm)	Si/Al ratio (-)	Rate constant k'_1 (transalkylation) (m^{-3} kg s)	Rate constant k'_2 (isomerization) (m^{-3} kg s)
N.1	160	95.0	4.2×10^{-3}	1.2×10^{-3}
N.2	113	155	1.3×10^{-3}	0.90×10^{-3}
N.3	100	357	0.45×10^{-3}	0.90×10^{-3}

The reaction control conditions were located below Thiele modulus (⌀) of 0.100 [-]. For the analyzed H-MFI- type zeolite (Si/Al = 95.0), particles with a size (D) below 125 nm will be in this region.

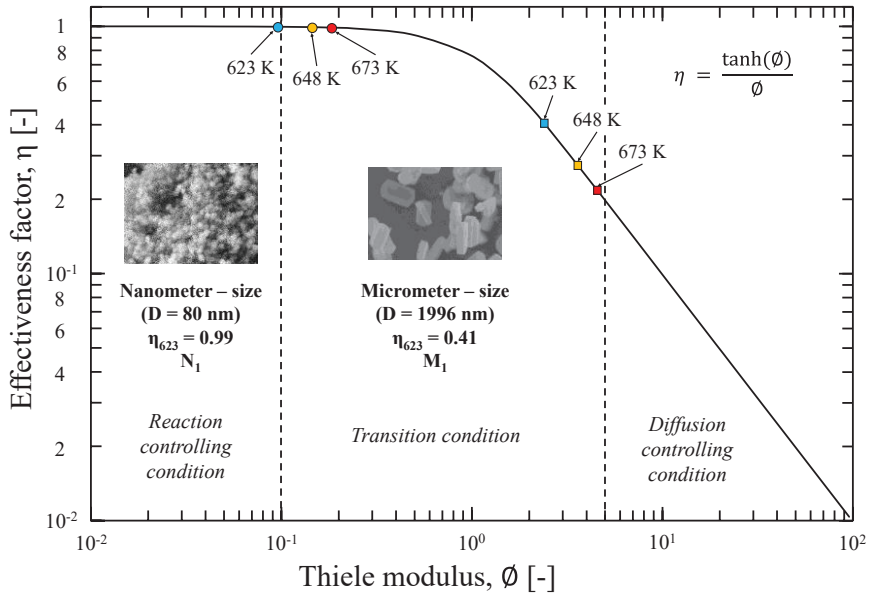

Figure. 4.9 Thiele modulus vs. effectiveness factor in the transalkylation reaction at 350 °C (623 K), 375 °C (648 K) and 400 °C (673 K) over H–MFI–type zeolites with different particle size (nm) in supercritical fluid.

4.4 Conclusions

I studied the kinetics of the catalytic transalkylation of ppp and supercritical benzene over H–MFI–type zeolite particles, at the temperature ranges of 623 – 678 K (11.0 MPa), as well as the effect of particle size and Si/Al ratio. For this case, I developed a 1st order kinetic model, assuming a parallel bimolecular reaction based on the consumption of ppp, to form phenol and isomers molecules.

Nanometer- size particles, located in the reaction control condition, exhibited higher conversion and selectivity towards the desired reaction pathway (transalkylation reaction) compared to the micrometer- size particles, located in the transition control conditions. Decreasing the particle size successfully reduced the internal diffusion limitations and increased the selectivity of the reaction, nonetheless, it also increases the isomerization reactions due to an increase of the external surface area.

Additional variables affect the kinetics of the reaction when modifying the amount of Al T–sites in the framework of the zeolite (Si/Al ratios), however, a small tendency to increase the reaction rate constant was observed when increasing the Al content. More research is required to determine if other factors are also influencing the reaction rate, such as diffusion limitations. Decreasing particle size suggests lower Thiele modulus numbers and higher effectiveness factor.

Finally, I was able to obtain high conversion of ppp and selectivity (phenol production), and low coke formation when decreasing the size of the H-MFI- type zeolite particles, in a fixed bed reactor under supercritical conditions.

Chapter 4

Reference

[1] O. International, F. Programme, Bioeconomy to 2030: 2030:, Agenda (2009).

[2] V.K. Garlapati, A.K. Chandel, S.P.J. Kumar, S. Sharma, S. Sevda, A.P. Ingle, D. Pant, Circular economy aspects of lignin: Towards a lignocellulose biorefinery, Renewable and Sustainable Energy Reviews 130 (2020). https://doi.org/10.1016/j.rser.2020.109977.

[3] D. Huang, R. Li, P. Xu, T. Li, R. Deng, S. Chen, Q. Zhang, The cornerstone of realizing lignin value-addition: Exploiting the native structure and properties of lignin by extraction methods, Chemical Engineering Journal 402 (2020) 126237. https://doi.org/10.1016/j.cej.2020.126237.

[4] S.S. Wong, R. Shu, J. Zhang, H. Liu, N. Yan, Downstream processing of lignin derived feedstock into end products, Chem Soc Rev 49 (2020) 5510–5560. https://doi.org/10.1039/d0cs00134a.

[5] M. Kleinert, T. Barth, Phenols from Lignin, Chem. Eng. Technol. 31 (2008) 736–745. https://doi.org/10.1002/ceat.200800073.

[6] Z. Strassberger, S. Tanase, G. Rothenberg, The pros and cons of lignin valorisation in an integrated biorefinery, RSC Adv. 4 (2014) 25310–25318. https://doi.org/10.1039/C4RA04747H.

[7] L. Das, P. Kolar, R. Sharma-Shivappa, J. Classen, J. Osborne, Oxidative Depolymerization of Lignin Using Supported Niobium Catalysts, ChemEngineering 1 (2017) 17. https://doi.org/10.3390/chemengineering1020017.

[8] D. Bourbiaux, J. Pu, F. Rataboul, L. Djakovitch, C. Geantet, D. Laurenti, Reductive or oxidative catalytic lignin depolymerization: An overview of recent advances, Catal Today 373 (2021) 24–37. https://doi.org/10.1016/j.cattod.2021.03.027.

[9] K. Ninomiya, K. Ochiai, M. Eguchi, K. Kuroda, Y. Tsuge, C. Ogino, T. Taima, K. Takahashi, Oxidative depolymerization potential of biorefinery lignin obtained by ionic liquid pretreatment and subsequent enzymatic saccharification of eucalyptus, Ind Crops Prod 111 (2018) 457–461. https://doi.org/10.1016/j.indcrop.2017.10.056.

[10] T. Voitl, P. Rudolf von Rohr, Oxidation of Lignin Using Aqueous Polyoxometalates in the Presence of Alcohols, ChemSusChem 1 (2008) 763–769. https://doi.org/10.1002/cssc.200800050.

[11] G. Chatel, R.D. Rogers, Review: Oxidation of Lignin Using Ionic Liquids—An Innovative Strategy To Produce Renewable Chemicals, ACS Sustain Chem Eng 2 (2014) 322–339. https://doi.org/10.1021/sc4004086.

[12] M. Wang, J. Lu, X. Zhang, L. Li, H. Li, N. Luo, F. Wang, Two-Step, Catalytic C–C Bond Oxidative Cleavage Process Converts Lignin Models and Extracts to Aromatic Acids, ACS Catal 6 (2016) 6086–6090. https://doi.org/10.1021/acscatal.6b02049.

[13] T. Yoshikawa, S. Shinohara, T. Yagia, N. Ryumon, Y. Nakasaka, T. Tagoa, T. Masudaa, Productionofphenolsfrom lignin-derived slurry liquid using iron oxidecatalyst, Applied Catalysis B: Envrionmental 146 (2014) 289–297. https://doi.org/10.1016/j.apcatb.2013.03.010.

[14] G. Kabir, B.H. Hameed, Recent progress on catalytic pyrolysis of lignocellulosic biomass to high-grade bio-oil and bio-chemicals, Renewable and Sustainable Energy Reviews 70 (2017) 945–967. https://doi.org/10.1016/j.rser.2016.12.001.

[15] H. Ben, A.J. Ragauskas, One step thermal conversion of lignin to the gasoline range liquid products by using zeolites as additives, RSC Adv 2 (2012) 12892.

https://doi.org/10.1039/c2ra22616b.

[16] M. Kleinert, T. Barth, Towards a Lignincellulosic Biorefinery: Direct One-Step Conversion of Lignin to Hydrogen-Enriched Biofuel, Energy & Fuels 22 (2008) 1371–1379. https://doi.org/10.1021/ef700631w.

[17] V.K. Ponnusamy, D.D. Nguyen, J. Dharmaraja, S. Shobana, J.R. Banu, R.G. Saratale, S.W. Chang, G. Kumar, A review on lignin structure, pretreatments, fermentation reactions and biorefinery potential, Bioresour Technol 271 (2019) 462–472. https://doi.org/10.1016/j.biortech.2018.09.070.

[18] V. Ponnuchamy, J. Sandak, A. Sandak, Revealing of Supercritical Water Gasification Process of Lignin by Reactive Force Field Molecular Dynamics Simulations, Processes 9 (2021) 714. https://doi.org/10.3390/pr9040714.

[19] M.M. Rahman, R. Liu, J. Cai, Catalytic fast pyrolysis of biomass over zeolites for high quality bio-oil – A review, Fuel Processing Technology 180 (2018) 32–46. https://doi.org/10.1016/j.fuproc.2018.08.002.

[20] M. Brebu, G. Cazacu, O. Chirila, Pyrolysis of lignin - A potential method for obtaining chemicals and/or fuels, Cellulose Chemistry and Technology 45 (2011) 43–50.

[21] D. Kai, M.J. Tan, P.L. Chee, Y.K. Chua, Y.L. Yap, X.J. Loh, Towards lignin-based functional materials in a sustainable world, Green Chemistry 18 (2016) 1175–1200. https://doi.org/10.1039/C5GC02616D.

[22] A. Grossman, W. Vermerris, Lignin-based polymers and nanomaterials, Curr Opin Biotechnol 56 (2019) 112–120. https://doi.org/10.1016/j.copbio.2018.10.009.

[23] B.M. Upton, A.M. Kasko, Strategies for the Conversion of Lignin to High-Value Polymeric Materials: Review and Perspective, Chem Rev 116 (2016) 2275–2306. https://doi.org/10.1021/acs.chemrev.5b00345.

[24] C. Wang, R.A. Venditti, UV Cross-Linkable Lignin Thermoplastic Graft Copolymers, ACS Sustain Chem Eng 3 (2015) 1839–1845. https://doi.org/10.1021/acssuschemeng.5b00416.

[25] M.L. Stone, E.M. Anderson, K.M. Meek, M. Reed, R. Katahira, F. Chen, R.A. Dixon, G.T. Beckham, Y. Román-Leshkov, Reductive Catalytic Fractionation of C-Lignin, ACS Sustain Chem Eng 6 (2018) 11211–11218. https://doi.org/10.1021/acssuschemeng.8b02741.

[26] S. Van den Bosch, W. Schutyser, R. Vanholme, T. Driessen, S.-F. Koelewijn, T. Renders, B. De Meester, W.J.J. Huijgen, W. Dehaen, C.M. Courtin, B. Lagrain, W. Boerjan, B.F. Sels, Reductive lignocellulose fractionation into soluble lignin-derived phenolic monomers and dimers and processable carbohydrate pulps, Energy Environ Sci 8 (2015) 1748–1763. https://doi.org/10.1039/C5EE00204D.

[27] T.I. Korányi, B. Fridrich, A. Pineda, K. Barta, Development of 'Lignin-First' Approaches for the Valorization of Lignocellulosic Biomass, Molecules 25 (2020) 2815. https://doi.org/10.3390/molecules25122815.

[28] E.M. Anderson, M.L. Stone, M.J. Hülsey, G.T. Beckham, Y. Román-Leshkov, Kinetic Studies of Lignin Solvolysis and Reduction by Reductive Catalytic Fractionation Decoupled in Flow-Through Reactors, ACS Sustain Chem Eng 6 (2018) 7951–7959. https://doi.org/10.1021/acssuschemeng.8b01256.

[29] X. Ouyang, X. Huang, B.M.S. Hendriks, M.D. Boot, E.J.M. Hensen, Coupling organosolv fractionation and reductive depolymerization of woody biomass in a two-step catalytic process, Green Chemistry 20 (2018) 2308–2319. https://doi.org/10.1039/c8gc00639c.

[30] Y. Kawamata, H. Ishimaru, K. Yamaguchia, T. Yoshikawa, Y. Koyama, Y. Nakasaka, S. Sato,

T. Masuda, Catalytic cracking of lignin model compounds and degraded lignin dissolved in inert solvent over mixed catalyst of iron oxide and MFI zeolite for phenol recovery, Fuel Processing Technology 197 (2020). https://doi.org/10.1016/j.fuproc.2019.106190.

[31] C. Cheng, J. Truong, J.A. Barrett, D. Shen, M.M. Abu-Omar, P.C. Ford, Hydrogenolysis of Organosolv Lignin in Ethanol/Isopropanol Media without Added Transition-Metal Catalyst, ACS Sustain Chem Eng 8 (2020) 1023–1030. https://doi.org/10.1021/acssuschemeng.9b05820.

[32] I. Kumaniaev, E. Subbotina, J. Sävmarker, M. Larhed, M. V. Galkin, J.S.M. Samec, Lignin depolymerization to monophenolic compounds in a flow-through system, Green Chemistry 19 (2017) 5767–5771. https://doi.org/10.1039/C7GC02731A.

[33] Q. Song, F. Wang, J. Cai, Y. Wang, J. Zhang, W. Yu, J. Xu, Lignin depolymerization (LDP) in alcohol over nickel-based catalysts via a fragmentation–hydrogenolysis process, Energy Environ Sci 6 (2013) 994. https://doi.org/10.1039/c2ee23741e.

[34] C. Zhang, F. Wang, Catalytic Lignin Depolymerization to Aromatic Chemicals, Acc Chem Res 53 (2020) 470–484. https://doi.org/10.1021/acs.accounts.9b00573.

[35] X. Chen, B. Zhang, Y. Wang, N. Yan, Valorization of Renewable Carbon Resources for Chemicals, Chimia (Aarau) 69 (2015) 120. https://doi.org/10.2533/chimia.2015.120.

[36] L. Li, L. Dong, D. Li, Y. Guo, X. Liu, Y. Wang, Hydrogen-Free Production of 4-Alkylphenols from Lignin via Self-Reforming-Driven Depolymerization and Hydrogenolysis, ACS Catal 10 (2020) 15197–15206. https://doi.org/10.1021/acscatal.0c03170.

[37] A. Hendry, M. Åhlén, T. Fernandes, O. Cheung, A. Sanna, Catalytic cracking of Etek lignin with zirconia supported metal-oxides for alkyl and alkoxy phenols recovery, Bioresour Technol 317 (2020) 124008. https://doi.org/10.1016/j.biortech.2020.124008.

[38] H.Y. Zhao, D. Li, P. Bui, S.T. Oyama, Hydrodeoxygenation of guaiacol as model compound for pyrolysis oil on transition metal phosphide hydroprocessing catalysts, Appl Catal A Gen 391 (2011) 305–310. https://doi.org/10.1016/j.apcata.2010.07.039.

[39] A.M. Robinson, J.E. Hensley, J.W. Medlin, Bifunctional Catalysts for Upgrading of Biomass-Derived Oxygenates: A Review, ACS Catal 6 (2016) 5026–5043. https://doi.org/10.1021/acscatal.6b00923.

[40] F. Mai, K. Cui, Z. Wen, K. Wu, F. Yan, M. Chen, H. Chen, Y. Li, Highly selective conversion of guaiacol to *tert* -butylphenols in supercritical ethanol over a H_2WO_4 catalyst, RSC Adv 9 (2019) 2764–2771. https://doi.org/10.1039/C8RA07962E.

[41] R. Ma, K. Cui, L. Yang, X. Ma, Y. Li, Selective catalytic conversion of guaiacol to phenols over a molybdenum carbide catalyst, Chemical Communications 51 (2015) 10299–10301. https://doi.org/10.1039/C5CC01900A.

[42] H. Ishimaru, T. Yoshikawa, Y. Nakasaka, E. Fumoto, S. Sato, T. Masuda, Synthesis of phenol from degraded lignin using synergistic effect of iron-oxide based catalysts: Oxidative cracking ability and acid-base properties, Catal Today 407 (2023) 194–200. https://doi.org/10.1016/j.cattod.2022.01.007.

General Conclusions

In this thesis, I have investigated soft-templating methods for the synthesis of nanomaterials with different morphologies towards catalytic applications. Specifically, aluminosilicate materials and their catalytic applications in the Catalytic Decomposition of Methane (CDM) and the transalkylation of 4-propylphenol ppp and supercritical benzene.

Chapter 1, briefly discuss the importance of nanomaterials in the current technological wave and the basic concepts of lyotropic mixtures which are key for the operation of the supramolecular arrangements of amphiphilic molecules (surfactants) that act as templates, with specific morphologies. Additionally, I discussed the importance and advantages of aluminosilicate materials. In Chapter 2, two main soft-templating methods are described and I further discussed the synthesis of amorphous and crystalline aluminosilicate nanomaterials and their characterization. In Chapter 3, I evaluate the potential of a-ASns as supports of active species (nickel oxide) for CDM, and further evaluate the effect of metal promoters (lanthanum and chromium) for this type of aluminosilicate materials. I also evaluated the morphology effect of the active particle itself, both as an active species and as a support for other active metal species (lanthanum and copper). Finally, in Chapter 4, I evaluated the effect of particle size on MFI-type zeolites for the transalkylation of 4-propylphenol (ppp) and supercritical benzene in a continuous fixed bed reactor. The effect of particle size was evaluated on the overall catalytic performance of the zeolite; yield, stability, selectivity and diffusion limitations.

Summary of Chapter 2

In Chapter 2, I successfully synthesized both amorphous and crystalline aluminosilicate, using the self-assembly characteristics of amphiphilic molecules in lyotropic mixtures. I mainly focus on liquid crystals and emulsion solutions based on Water/Surfactant/Organic solvent to create flexible supramolecular arrangements that act as templates for the synthesis of these aluminosilicate nanomaterials. In the TRAP method, lyotropic liquid crystals solutions are used to create sheet-like arrangements of the amphiphilic molecules used in the mixture, to synthesize amorphous aluminosilicate nanosheets. I successfully synthesized a-ASns conformed of homogeneous a-AS nanoplates of 20 nm diameter, 3 nm in height and 66 m^2g^{-1} of external surface by controlling the concentration of alkaline catalyst for the hydrolysis of Si and Al species. Finally, I successfully synthesized nanosized H-MFI-type zeolite using the emulsion method by a mixture of Water/O-15 surfactant/Cyclohexane and hydrothermal synthesis. Nanosized particles ranged from 100 – 160 nm in diameter based on the amount of aluminum used in the synthesis.

Summary of Chapter 3

In Chapter 3, I studied the potential of amorphous aluminosilicates as support for catalytic metal species in CDM. When compared to its counterpart, bulk amorphous aluminosilicate, 2-dimensional nanomaterials showed catalytic improvement in H_2 generation, however, due to the flat surface of the a-ASns, poor crystallization and vertical aggregation was promoted. Mesoporous amorphous aluminosilicates a-AS.m showed the best performance due to the crystallization boost that high surface area with multiple contact points could offer. I also evaluated the effect of metal promoters La^{3+} and Cr^{3+} and found that La species positively promote the NiO particles due to charge transfer assistance but only on certain concentrations by a double wet impregnation method (first impregnation of La

species into aAS.m + calcination followed by an impregnation of Ni species to promoted support). Cr species hindered the CDM reaction in all concentrations. Based on the results I have hypothesized that Cr species has strong interactions with Ni species, hence, strong sintering effects were observed after calcination, and adverse charge transfer from Ni^{3+} to Cr^{3+} might be rendering Ni species inactive. Nonetheless, the combination of La and Cr species show a positive effect, where the sintering effect of Cr species, which creates smaller mesoporous in the a-AS.m support has a synergistic effect with La species, compensating the adverse charge effect of Cr species. Finally, the morphology of Ni species was evaluated. α-$Ni(OH)_2$ nanosheets (Ni.ns) comprised of the aggregation of several nanoplates were synthesized using TRAP's. I evaluated the effect of this metal hydroxide nanoparticles both as an active species and as a support. When using the Ni.ns as active species, a dissolution in acidic solution is required to reduce the size of the nanosheets to be able to be impregnated on the supports, otherwise, the Ni.ns are too big to be loaded into the supports. I performed a final experiment, where Ni.ns were used as supports for La^{3+} and Cu^{3+}. This novel catalyst showed great performance in CDM and great stability. More research is required; however, I established the foundations for the synthesis of novel catalysts for CDM with a wide range of nano supports with different morphologies using lyotropic mixtures and tailored to the specific requirements of the catalytic application.

Summary of Chapter 4

In Chapter 4, I studied the kinetics of the transalkylation of ppp and supercritical benzene over H-MFI-type zeolite in a Fixed Bed Reactor. I evaluated the effect of particle size of MFI-type zeolites on the kinetics of the reaction at different temperatures and supercritical conditions. I established a 1st order kinetic model assuming a parallel bimolecular reaction based on the consumption of ppp to form phenol and isomers molecules. The reaction rate constants over micrometer– H–MFI–type zeolite ($k'_{1,macro}$) were 1.68 x 10^{-5}, 1.02 x 10^{-6}, and 7.50 x 10^{-6} s^{-1}, for the 350, 375 and 400 °C points, respectively. For the nanometer–sized H–MFI–type zeolite ($k'_{1,nano}$) were 9.36 x 10^{-5}, 4.45 x 10^{-5}, and 2.49 x 10^{-5} s^{-1}, for the 350, 375 and 400 °C points, respectively. Finally, I evaluated the Thiele modulus of the catalysts and decreasing particle size suggests lower Thiele modulus numbers and higher effectiveness factor, hence lower diffusion limitations. According to Thiele modulus calculations, nanosized H-MFI-zeolites showed that the transalkylation took place in the kinetic controlling region.

List of Publications

1. **Jose A. Hernandez Gaitan**, Xinyu Li, Kazuya Tamura, Koji Miyake*, Yoshiaki Uchida, Norikazu Nishiyama, “Ni Particle Morphology and Support Effect in the Catalytic Decomposition of Methane: Into the Design of Novel, High Yield Catalyst for Catalytic Decomposition of Methane”, *Adv. Energy Sustainability Res.*, 2400096 (2024).

2. **Jose A. Hernandez Gaitan**, Koki Sasaki, Koji Miyake, Yoshiaki Uchida, Norikazu Nishiyama, "Control of Composition and Surface Area of Aluminosilicates by Tuning Base Catalyst Concentration," *Chem. Lett.*, 53, upad034 (2024)

3. **Jose A. Hernandez Gaitan**, Yuta Nakasaka, Takuya Yoshikawa, Norikazu Nishiyama, Takao Masuda, “Catalytic transalkylation of alkylphenol to phenol in supercritical benzene fluid over MFI type zeolite in a fixed-bed reactor: Diffusion and reaction limitations”, *Chem. Eng. J.*, 464, 142618, (2023)

Related papers

1. Koji Miyake, Tomoka Sumi, Shinya Kokuryo, Haruna Kitamura, **Jose A. Hernandez Gaitan**, Yoshiaki Uchida, Norikazu Nishiyama, "Improved methane dehydroaromatization reaction over Mo and Cr co-doped ZSM-5 catalyst," *New J. Chem.*, 47, 6054-6057 (2023)

2. Koki Sasaki, **Jose A. Hernandez Gaitan**, Yuki Tokuda, Koji Miyake, Yoshiaki Uchida, Norikazu Nishiyama, "A Nanosheet Molding Method to Estimate the Size of Bilayers Suspended in Liquid,” *J. Mater. Chem. C*, 10, 15816-15821 (2022).

3. Koki Sasaki, **Jose A. Hernandez Gaitan**, Tsuyoshi Okue, Shotaro Matoba, Yuki Tokuda, Koji Miyake, Yoshiaki Uchida, Norikazu Nishiyama, "Amorphous Aluminosilicate Nanosheets as Universal Precursors for the Synthesis of Diverse Zeolite Nanosheets for Polymer-Cracking Reactions," *Angew. Chem. Int. Ed*., 61, e202213773 (2022).

4. Xinyu Li**, Jose A. Hernandez Gaitan**, Shinya Kokuryo, Tomoka Sumi, Haruna Kitamura, Koji Miyake, Yoshiaki Uchida, Norikazu Nishiyama, "Hierarchical zeolites with high hydrothermal stability prepared via desilication of OSDA-occluded zeolites," *Micropor. Mesopor. Mater*., 344, 112096 (2022).

List of Presentations in International Conferences

1. 20th International Zeolite Conference (IZC) July 3rd – July 8th , 2022
   Poster presentation "Diffusion and Reaction Limitations: Catalytic Transalkylation of Alkylphenol to Phenol in Supercritical Benzene Fluid over MFI-type Zeolite
2. SCEJ 89th Annual Meeting (SCEJ) March 18th – March 20th , 2024
   Oral presentation "Potential of Amorphous Aluminosilicate Nanosheets and TRAP Method"

Awards

1 2023 Japan Liquid Crystal Society Paper Award, Category A, Award-winning paper "Amorphous Aluminosilicate Nanosheets as Universal Precursors for the Synthesis of Diverse Zeolite Nanosheets for Polymer‐Cracking Reactions"

Others

1 40th Researcher Overseas Dispatch Support Award - Murata Academic and Education Foundation, 2024

1 International Research Conference Dispatch Researcher Award – Yoshida Science and Technology Foundation, 2024

Acknowledgement

I am very grateful for all the help and guidance that Professor Dr. Norikazu Nishiyama, Associate Professor Dr. Yoshiaki Uchida and Assistant Professor Dr. Koji Miyake gave me during my years of research in Osaka University and their contributions. Professor Dr. Norikazu Nishiyama constantly worried about my progress and proposed valuable ideas and suggestions during discussions and seminars and was always very patient and kind. Without his continuous support and thoughtful guidance and persistent help, I wouldn't have been able to achieve this milestone in my academic career. I especially would like to thank Associate Professor Dr. Yoshiaki Uchida whose invaluable advice guided me when I needed it the most. Not only he supported me and gave taught me many lessons on how to excel as a researcher both in Japan as in the world, but he also motivated me to never give up even when cultural, language or challenging barriers appeared. Assistant Professor Dr. Koji Miyake punctual advice help me to challenge myself beyond my expectations, by suggesting topics that might have sounded too challenging, but were the key to create the results that my research yielded over these three years. I would like to thank Prof. Dr. Takao Masuda and Prof. Dr. Yuta Nakasaka at Hokkaido University for their critical comments and helpful suggestions for my first paper, which was the foundation for all my doctoral studies.

I wish to express thanks to Professor Prof. Dr. Takashi Harada from the Osaka University Solar Energy Chemistry Research Center, for his crucial help and advised for the correct operation of FE-SEM equipment and the correct imaging for my different samples, which led to the image quality required for publications. I would also like to thank Dr. Sato Takagi from the Research Center for Ultra-High Voltage Electron Microscopy at Osaka University for its help with the special analysis using HRSTEM. Also to the Japanese Government for supporting me with the MEXT scholarship, which was of invaluable help to continue my higher education.

To my coworkers, I would like to express my gratitude; Dr. Koki Sasaki, Dr. Yasuhiro Shu, Mrs. Xinyu Li, Mrs. Xinran Yang, Mr. Yuuki Tokuda, Mr. Shohei Kubota, Mr. Ryuji Takada, Mrs. Miu Hirata, Mrs. Sumi Tomoka and Mrs. Haruna Kitamura for their help, support, comments on my research and overall, their kind treatment towards me which make my studying in Nishiyama laboratory, very enjoyable. I really appreciate Dr. Koki Sasaki, for all his help and guidance at the beginning of my doctoral studies, which allowed me to catch up real fast. Mrs. Xinyu Li, for her kind comments, motivation and all her valuable insight and discussion for the characterization of nanoparticles. Finally, Mrs. Hirata, Mr. Kubota and Mr. Takada for their great patience and help for all procedures in Japanese, not only they help me check my grammar and vocabulary, but they also took the time to always help me in my Japanese studies.

I am especially thankful to my wife and my mother. To my mother who always put herself last, to make sure my sisters and I could have an education and always supported me in all my dreams and aspirations. To my wife, for supporting and motivating me to pursue my dreams, even when it meant to leave our country and move to a different continent. She has always cared for, supported and pushed me to be a better version of myself. Without them, none of this would have been possible. Last but not least, I am thankful to God, who has always guided my path, has never abandon me, and has always fill my hearth with strength and resilience to overcome the challenges of life.

José Andrés Hernández Gaitán

2024